UC San Diego
UC San Diego Electronic Theses and Dissertations

Title

First-Principles Studies of Surface Energies of Magnetic Full-Heuslers and Machine Learning of Hybrid Perovskites

Permalink

https://escholarship.org/uc/item/0p69m3tn

Author

Wong, Joseph

Publication Date

2019

Peer reviewed|Thesis/dissertation

UNIVERSITY OF CALIFORNIA SAN DIEGO

First-Principles Studies of Surface Energies of Magnetic Full-Heuslers and Machine Learning of Hybrid Perovskites

A thesis submitted in partial satisfaction of the
requirements for the degree
Master of Science

in

Nanoengineering

by

Joseph Wong

Committee in charge:

Professor Kesong Yang, Chair
Professor Shyue Ping Ong
Professor Tod Pascal

2019

The thesis of Joseph Wong is approved, and it is acceptable in quality and form for publication on microfilm and electronically:

_____

_____

_____

Chair

University of California San Diego

2019

TABLE OF CONTENTS

LIST OF FIGURES

ACKNOWLEDGEMENTS

I would like to acknowledge my research advisor, Dr. Kesong Yang, for his constant guidance and mentoring throughout my work for my masters thesis. I am greatly appreciative of his time and dedication put in to improving my critical thinking and writing skills used to produce these works.

I would also like to acknowledge current and former group members for teaching me how to perform many of the techniques used in this work: Dr. Safdar Nazir, Dr. Jianli Cheng, Dr. Mazier Behtash, Yuheng Li, Sicong Jiang, and Paul Joo. I am appreciative of their willingness to teach me how to use the tools necessary to perform these works.

Chapter 1, in full, is currently being prepared for submission for publication of the material. Wong, Joseph; Nazir, Safdar; Yang, Kesong. The thesis author was the primary investigator and author of this material.

Chapter 2, in full, is currently being prepared for submission for publication of the material. Wong, Joseph; Li, Yuheng; Jiang, Sicong; Yang, Kesong. The thesis author was the primary investigator and author of this material.

Chapter 3, in full, is currently being prepared for submission for publication of the material. Wong, Joseph; Yang, Kesong. The thesis author was the primary investigator and author of this material.

Chapter 4, in part, is a reprint of the material as it appears in the Journal of the European Ceramic Society, 2019. Behtash, Mazier; Wong, Joseph; Jiang, Sicong; Luo, Jian; Yang, Kesong. Dr. Mazier Behtash was the primary investigator of this material.

Chapter 5, in full, is currently being prepared for submission for publication of the material. Wong, Joseph; Cheng, Jianli; Yang, Kesong. The thesis author was the primary investigator and author of this material.

2018	B. S. in Chemical Engineering, University of California San Diego
2016-2019	Research Assistant, University of California San Diego
2018-2019	Teaching Assistant, University of California San Diego
2019	M. S. in Nanoengineering, University of California San Diego

PUBLICATIONS

Maziar Behtash, Joseph Wong, Sicong Jiang, Jian Luo, and Kesong Yang, "First-Principles Study of Impurity Segregation in Zirconia, Hafnia, and Yttria-Stabilized-Zirconia Grain Boundaries", *J. Eur. Ceram. Soc.*, (2019).

Liyuan Wu, Pengfei Lu, Yuheng Li, Yan Sun, Joseph Wong, and Kesong Yang, "First-Principles Characterization of Two-Dimensional $(CH_3(CH_2)_3NH_3)_2(CH_3NH_3)_{n-1}Ge_nI_{3n+1}$ Perovskite", *J. Mater. Chem. A*, 6, 24389-24396, (2018).

Yuheng Li, Maziar Behtash, Joseph Wong, and Kesong Yang, "Enhancing Ferroelectric Dipole Ordering in Organic-Inorganic Hybrid Perovskite $CH_3NH_3PbI_3$: Strain and Doping Engineering", *J. Phys. Chem. C*, 122, 177-184, (2018).

Joseph Wong, Kesong Yang, "Two-Dimensional Hybrid Organic-Inorganic Perovskites: Photovoltaic and Optoelectronic Properties", *to be submitted*.

Joseph Wong, Safdar Nazir, Kesong Yang, "High-Throughput First-Principles Investigations of Magnetic Full Heusler Surface Energies", *to be submitted*.

Joseph Wong, Yuheng Li, Sicong Jiang, Kesong Yang, "Machine Learning Meta Ensemble for Formation Energy, Band Gap, and Charge Carrier Mobility of Hybrid Organic-Inorganic Perovskites", *in preparation*.

Joseph Wong, Jianli Cheng, Kesong Yang, "AIMSGB: Usage and Applications", *to be submitted*.

ABSTRACT OF THE THESIS

First-Principles Studies of Surface Energies of Magnetic Full-Heuslers and Machine Learning of Hybrid Perovskites

by

Joseph Wong

Master of Science in Nanoengineering

University of California San Diego, 2019

Professor Kesong Yang, Chair

Materials design is a cornerstone of every device. Historically, the materials selection process was characterized by a time consuming, expensive, Edisonian approach. In recent years however, rapid advancements in computational power and materials simulation software has spawned the field of computational materials science. Computational materials science opens a new avenue to materials discovery called high-throughput materials design. This approach allows for rapid prototyping of materials in a large, complex chemical space. In this work, the scope of high-throughput materials design approach is used in the analysis of several topics: magnetic full-heuslers, hybrid perovskites, and grain boundary structures. Using high-throughput density functional theory (DFT), we study the surface energy of 68 magnetic full heuslers to guide the synthesis of magnetic

tunnel junctions for applications in memory storage devices. We employ a high-throughput machine learning approach to explore the chemical space of single and double perovskite materials for applications in stable, high-performance solar cells. We also look deeper into hybrid perovskite materials in a literature review of two-dimensional hybrid perovskites, which demonstrate greater stability and tunable band gaps with simple fabrication routes. In addition, their strong binding energies lead to strong light emitting properties, with potential applications in light emitting diode devices. We also examine the configurational entropy of yttria-stabilized zirconia grain boundaries and provide example usage and applications of AIMSGB, an open-source python library for grain boundary structure generation.

Chapter 1

Surface Energy of Full Heuslers

1.1   Introduction

Heusler compounds are a class of ternary semiconducting or metallic alloys that have the X_2YZ (full-Heuslers) or the XYZ (half-Heuslers) formulas, where X and Y are transition metals, and Z is a main group element.[8] Heusler alloys exhibit a wide range of multifunctionalities including superconductivity,[9, 10] tunable topological insulators,[11, 12, 13] and high spin polarization.[14, 15, 16, 17] In particular, the half metallic ferromagnetism property of Heusler alloys at a high Curie temperature has attracted a lot of attention due to its ability to generate completely spin-polarized conduction electrons which has potential applications in spintronics,[18, 19, 20, 21] including tunnel magnetoresistance[22, 23] and spin torque transfer devices.[15, 24, 25]

Co-based full Heuslers are prominent candidates of the Heusler alloys due to their half metallicity with a high curie temperature above room temperature and stable structure.[23, 24, 26] Several experimental studies have demonstrated small magnetic damping constant,[23] perpendicular magnetic anisotropy,[27] and high tunnel magnetoresistance ratio[28] in thin films of Co-based Heuslers grown epitaxially on MgO substrates. In epitaxially grown Heusler thin films, the surface effects have been shown to influence the half-metallicity and spin polarization properties of the material. For example, several first-principles studies have shown that the half-metallic properties

are often lost at the surface due to surface states pinned at the Fermi level.[29, 30, 31, 32] Furthermore, surface roughness has also been shown to influence the tunneling magnetoresistance value.[33] Because the surface properties play a strong role in the properties of full Heuslers, it is important to control the surface composition to tune the magnetic and spin polarizing properties. The surface composition is heavily determined by the surface energy. Several first principles studies have examined the surface energies of Heusler compounds including Co_2XSi (X = Cr, Mn, Si),[34] Co_2VGa,[35] and Mn_2CoAl,[36] however the results of these studies are limited to these select few compounds and the (100) and (111) slab orientation. To the best of our knowledge, no studies have been done that have examined the surface energy with consideration of the composition flexibility of Heusler compounds and the different surface orientations.

In this work, we performed a high throughput first-principles calculation of the surfaces of 68 different full Heusler alloys in the (100), (110), and (111) direction with consideration of all possible surface terminations at each orientation. In our analysis of the Co-based compounds, we found that the surface energy depends heavily on the Z atom, decreasing with increasing Z group (number of valence electrons) and period (atomic radius) number. We found that the surface energies tend to be the lowest for terminations that contain the Z atom and tend to be the highest with terminations containing the X atom. Compounds containing Sn as the Z atom exhibit especially low surface energies compared to other Z atom choices. Between the different surface orientations, the lowest surface energies are found in the (100) and (111) orientations. The surface energy is also found to be lower in the X-poor chemical potential condition and higher in the X-rich condition. The culmination of these trends leads to the lowest surface energy compounds in X-poor (100) YZ-terminated Co_2{Zr, Hf, Ti, Mn}Sn, Co_2MnGe, and Co_2{Hf, Mn, Ti}Ga, X-poor (111) Z-terminated Co_2{V, Zr, Ti, Mn}Sn, Co_2{Fe, Mn}Ge, Co_2{Hf, V, Cr}Ga, and X-rich (111) Z-terminated Co_2{Nb, V, Hf, Mn}Sn, and Co_2FeGe. This work lays the foundation for the control of surface terminations of epitaxially grown Heusler thin films.

1.2   Computational Details

All density functional theory (DFT) calculations were performed using the Vienna *Ab initio* Simulation Package (VASP).[37, 38] The projector augmented-wave (PAW) potentials were used for electron-ion interactions,[39] and the Perdew-Burke-Ernzerhof (PBE) generalized gradient approximation (GGA) is used for the exchange correlation functional.[40] A cutoff energy of 450 eV and a $9 \times 9 \times 1$ Gamma centered k-space grid was used for the slab models. Atomic coordinate relaxation was terminated when the interatomic forces were less than 0.01 eV Å^{-1}. For the bulk calculations, the automatic framework AFLOW[41] was used with a cutoff energy of 450 eV and a $10 \times 10 \times 10$ Gamma centered k-space grid. Atomic coordinate relaxation was terminated when the change in energy was less than 10^{-5} eV between two ionic steps. Electronic self-consistency was assumed at 10^{-5} eV and 10^{-6} eV for slab and bulk models respectively.

1.2.1   Surface Structure

Figure 1.1 shows the (a) Regular and (b) Inverse cubic and (c) Regular and (d) Inverse tetragonal full Heusler compounds. The cubic Heusler lattice contains four sites which form four fcc sublattices shown in Figure 1.1a) and 1.1b): Z (occupied by a Z atom), X(I) (occupied by an X atom), X(II) (occupied by X in regular cubic and Y in inverse cubic), and Y (occupied by Y in regular cubic and X in inverse cubic). In the regular cubic structure, the Y site is octahedrally coordinated by 6 Z atoms, and the X(I) and X(II) sites are both tetrahedrally coordinated by Y and Z atoms. In this case, both sites occupied by X atoms experience an equivalent environment. The inverse cubic structure can be obtained by switching the X and Y atoms in X(II) and Y, yielding the structure in Figure (1.1b). Here, the two X atoms have different environments. The X atom at the X(II) site is coordinated octahedrally by Z atoms and tetrahedrally by Y atoms while the one at the X(I) site is coordinated octahedrally by Y atoms and tetrahedrally by Z atoms. The regular and inverse tetragonal Heuslers can be obtained by stretching/compressing the cubic Heusler counterparts along the z axis. In this work, we only studied the properties of the regular cubic

3
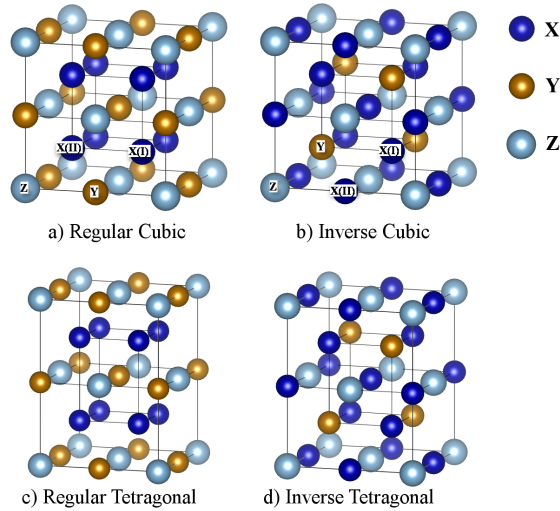
Figure 1.1: The four types of Heusler structures: (a) Regular Cubic, (b) Inverse Cubic, (c) Regular Tetragonal, and (d) Inverse Tetragonal

Heusler compounds because several high performing Heusler compounds have been shown to crystallize in this phase.[42, 43]

The Heusler compounds studied in this work belong to the regular cubic full-Heusler family. The full-Heusler alloys adopt the formula, X_2YZ, and crystallize in the $L2_1$ structure composed of four fcc sublattices as shown in Fig. 1.2.[8] The lattice parameters for the bulk Heusler compounds were calculated via DFT. We selected 68 compounds that demonstrate promising magnetic properties. These bulk compounds were used as the basis for the 408 slab structures, which were generated using the Pymatgen surface and structure modules.[44, 45, 46] Figure 1.2 shows the slabs structures constructed for every possible surface termination in the (100), (110), and (111) directions. In the (100) direction, there are two terminations: X_2 (a) and YZ (b). In the (110) direction, there is only one X_2YZ termination (c). In the (111) direction, there are three terminations: X (d), Y (e), and Z (f). Each slab was constructed with a 10 Åvacuum layer and with symmetric surface terminations (i.e. X_2-X_2 or YZ-YZ for the (100) direction). These slab structures can be classified into two types: stoichiometric and nonstoichiometric. A stoichiometric slab is a slab that has the same atomic composition as the bulk (X_2YZ). Of all the slabs in this work, only the (110) oriented slab is classified as a stoichiometric slab. Conversely, a nonstoichiometric slab is one that does not
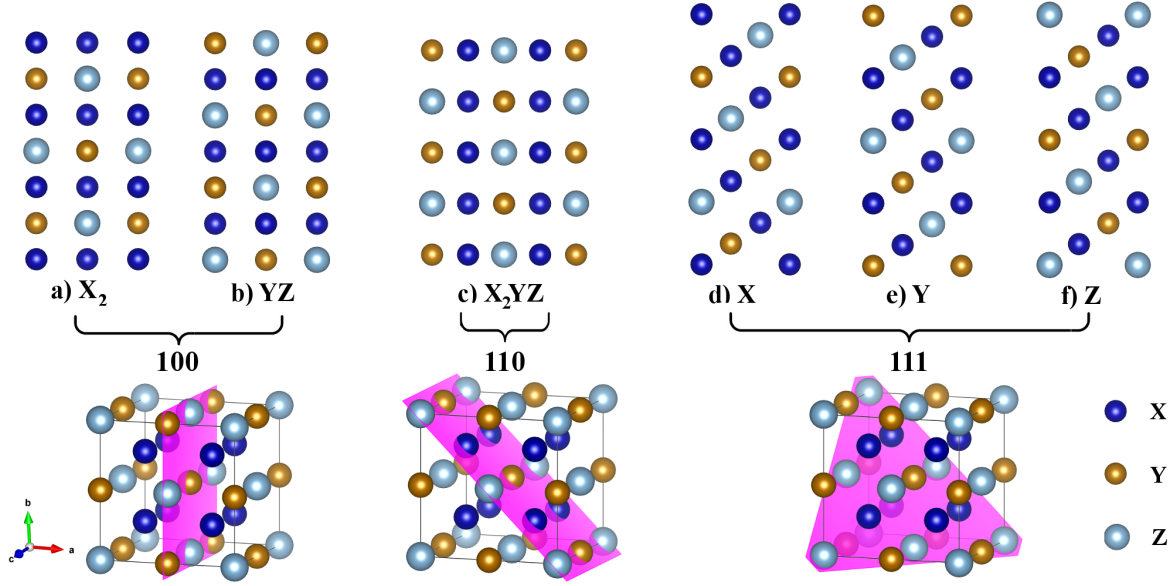
Figure 1.2: Sample slab terminations of X_2YZ: (a) X_2, (b) YZ, (c) X_2YZ, (d) X, (e) Y, (f) Z

have the same atomic composition as the bulk (i.e. X_3YZ). Of the slabs in this work, both (100) and (111) oriented slabs are considered nonstoichiometric.

1.2.2 Surface Energy Calculation

The calculation of the surface energy will be different for stoichiometric and nonstoichiometric slabs. For stoichiometric slabs, the surface energy can be calculated simply via

$$\gamma = \frac{[E_s - nE_b]}{2A} \tag{1.1}$$

where γ is the surface energy in J/m^2, E_s is the total energy of the slab structure, n is the number of formula units contained in the slab, E_b is the stoichiometrically equivalent energy of the bulk material, and A is the surface area of the slab. For nonstoichiometric slabs, γ can be calculated similarly with the inclusion of the chemical potential via

$$\gamma = \frac{[E_s - (nE_b \pm m\mu_x)]}{2A} \tag{1.2}$$

where μ_x is the chemical potential of the bulk dopant atoms necessary to reach the stoichiometric ratio of the slab and m is the number of atoms, x, needed to reach an equivalent stoichiometric amount. When the chemical environment is characterized as a x-rich condition, μ_x is equal to the energy of the bulk x material per atom. Because of the chemical potential term, the surface energy will become a range of values rather than a single scalar. For example, if the slab had a formula of $X_6Y_2Z_2$ and the bulk energy was derived from one stoichiometric unit, Eq. 1.2 becomes one of the following:

$$\gamma = \frac{[E_s - (2E_b + 2\mu_X)]}{2A} \tag{1.3}$$

$$\gamma = \frac{[E_s - (3E_b - \mu_Y - \mu_Z)]}{2A} \tag{1.4}$$

Eq. 1.3 and Eq. 1.4 lead to two different values for the surface energy, each corresponding to either the X-rich (Eq. 1.3) or X-poor (Eq. 1.4) condition.

Figure 1.3 summarizes the process of calculating the surface energies from the bulk Heusler structure. First, the structures of 68 bulk Heusler compounds are optimized and their energies are calculated. Next, these optimized structures are used as basis to generate the 408 slab structures via the Pymatgen library. These slab structures then undergo a highthroughput DFT calculation, yielding the slab energies. Bulk X/Y/Z calculations are used to determine the chemical potential term in Eq. 1.2. All these raw compound energies are then used to calculate the surface energies for each slab for all surface orientations and surface terminations.
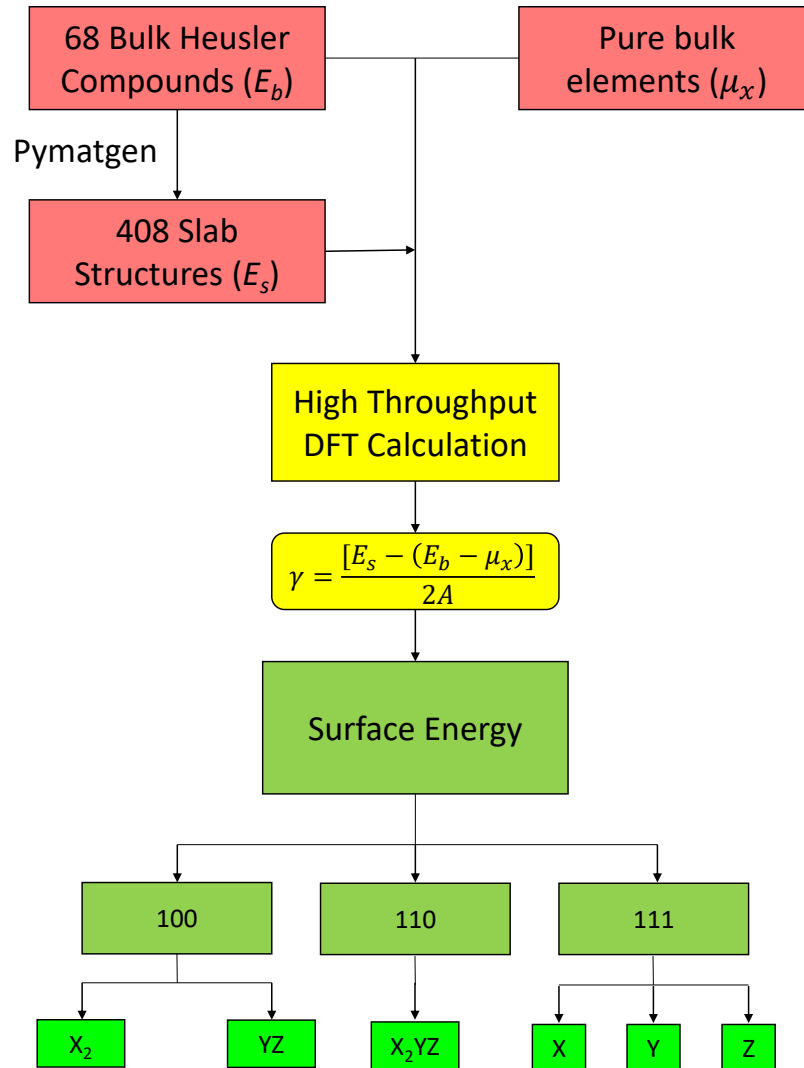
Figure 1.3: Surface energy calculation flowchart beginning with bulk Heusler compounds and ending with Heusler surface energies.

1.3   Results and Discussion

1.3.1   Surface Energy Data

Our calculated surface energies for 68 full-Heusler alloys are tabulated in Table 1.1 for the X-poor condition and in Table 1.2 for the X-rich condition. In the case of the stoichiometric (110) oriented surfaces, the surface energy values are the same in both tables since there are no rich/poor conditions. The compound names are sorted alphabetically first by the X atom, then by the Z atom, thereby sorting the surface energies by X-atom and further sorting each X-atom group by the Z-atom. The columns containing the surface energies are categorized first by the surface orientation (i.e. (100), (110), or (111)), then by the surface termination (i.e. X_2, YZ, X, Y, or Z). Compared to the inverse full-Heusler Mn_2CoAl which has a calculated average surface energy of 3.104 J/m^2 for the (100) surface,[36] our results for the regular full-Heusler counterpart are somewhat lower with surface energies of 2.03 J/m^2 and 0.98 J/m^2 in the X-poor condition for the X_2 and YZ terminations and 1.80 J/m^2 and 1.21 J/m^2 in the X-rich condition for the X_2 and YZ terminations respectively. In the following discussion, we will focus our analysis on the 30 Co-based compounds because Co-based Heusler alloys have been shown to exhibit excellent magnetic properties, including half-metallicity with a high T_C, small magnetic damping constant, and high spin polarization.[26, 23, 47]

1.3.2   (100) Surface Orientation

Fig 1.4 shows the (100) surface energies of the Co_2 based compounds plotted against the Z atom in order of increasing group number. The left and right plots show the surface energy data under the X-poor and X-rich conditions. Our surface energy values for Co_2MnSi predict the same low energy terminations as those predicted by Khosravizadeh *et al.*, who calculated surface energies of 0.58 J/m^2 for the X_2 termination and 0.16 J/m^2 for the YZ termination respectively.[34] We calculated Co_2MnSi surface energies of 3.79 J/m^2 and 1.29 J/m^2 for X-poor X_2 and YZ terminations and 2.40 J/m^2 and 2.44 J/m^2 for X-rich X_2 and YZ terminations respectively.

For Co_2FeSi, we calculated surface energies of 3.11 J/m^2 and 1.72 J/m^2 for X-poor X_2 and

Table 1.1: All surface energy data for the X-poor condition in J/m^2

	100		110	111				100		110	111		
Name	X_2	YZ	X_2YZ	X	Y	Z	Name	X_2	YZ	X_2YZ	X	Y	Z
Au$_2$MnZn	1.03	1.34	0.91	1.19	1.33	0.83	Fe$_2$MnAl	3.50	1.35	2.59	3.60	4.47	1.91
Co$_2$FeAl	3.68	1.64	2.29	3.73	2.54	1.55	Ga$_2$MnCo	0.76	1.60	0.46	0.58	1.03	0.55
Co$_2$HfAl	3.97	1.16	2.02	3.56	1.63	1.44	Mn$_2$CoAl	2.03	0.98	1.63	2.10	2.27	1.47
Co$_2$MnAl	3.83	1.23	2.36	3.91	2.61	1.67	Mn$_2$VAl	3.18	1.42	2.44	3.39	2.73	2.12
Co$_2$CrAl	3.34	1.77	2.60	3.91	2.89	1.36	Mn$_2$PtCo	2.09	2.02	1.96	1.77	1.83	2.45
Co$_2$NbAl	3.53	1.81	2.10	3.69	2.36	1.21	Mn$_2$CoCr	2.27	3.43	2.45	2.56	2.95	3.99
Co$_2$TaAl	3.57	2.08	2.27	3.70	2.65	1.24	Mn$_2$VGa	2.77	1.00	1.87	2.88	2.41	1.34
Co$_2$TiAl	4.16	1.43	2.26	3.97	1.91	1.53	Mn$_2$PtPd	2.52	1.62	2.02	2.37	1.97	2.06
Co$_2$VAl	3.64	2.06	2.27	3.97	2.68	1.31	Mn$_2$PtRh	2.19	1.80	1.76	1.85	1.78	2.16
Co$_2$ZrAl	3.82	0.94	1.88	3.41	1.39	1.39	Mn$_2$PtV	2.52	2.87	2.06	1.99	1.81	2.35
Co$_2$CrGa	3.05	1.40	1.75	3.26	2.41	0.84	Ni$_2$FeAl	2.64	1.70	1.76	2.90	2.35	1.20
Co$_2$FeGa	3.31	1.28	1.79	3.27	2.30	0.97	Ni$_2$FeGa	2.34	1.35	1.33	2.56	2.14	0.74
Co$_2$HfGa	3.70	0.73	1.47	3.04	1.18	0.66	Ni$_2$MnGe	2.17	0.66	0.92	2.29	1.50	0.32
Co$_2$VGa	3.28	1.57	1.85	1.91	2.36	0.75	Pd$_2$MnAu	2.36	1.70	2.46	2.56	1.83	1.92
Co$_2$MnGa	3.45	0.85	1.87	3.50	2.31	1.15	Pd$_2$MnCu	2.41	2.17	2.34	2.66	2.18	2.38
Co$_2$TiGa	3.89	0.90	1.81	3.61	1.69	1.01	Pd$_2$MnGe	1.92	1.53	1.63	2.36	1.88	1.17
Co$_2$FeGe	2.59	1.08	1.18	2.71	1.90	0.23	Pd$_2$MnSb	2.03	1.26	1.69	2.65	1.88	0.93
Co$_2$MnGe	3.25	0.74	1.52	3.36	2.08	0.57	Pd$_2$MnSn	2.12	1.28	1.84	2.91	2.18	1.32
Co$_2$FeSi	3.11	1.72	1.86	3.48	2.30	1.07	Pd$_2$MnZn	2.47	1.97	2.29	3.45	2.79	2.36
Co$_2$MnSi	3.79	1.26	2.15	4.14	2.43	1.23	Pt$_2$MnZn	2.36	1.18	1.24	2.12	1.40	0.90
Co$_2$TiSi	4.02	1.04	1.95	4.03	1.85	1.21	Rh$_2$MnAl	3.42	1.10	1.95	3.53	2.13	1.38
Co$_2$HfSn	3.28	0.33	1.13	2.66	1.09	-0.11	Rh$_2$MnGe	2.46	0.80	0.81	2.29	1.34	0.15
Co$_2$MnSn	3.08	0.49	1.08	3.00	1.93	0.40	Rh$_2$MnHf	2.72	1.84	1.79	2.90	1.91	1.49
Co$_2$NbSn	2.43	0.87	0.96	2.30	1.72	-0.24	Rh$_2$MnPb	2.32	0.70	1.02	2.34	1.56	0.48
Co$_2$TiSn	3.28	0.43	1.27	3.22	1.54	0.38	Rh$_2$MnSc	3.00	0.94	1.64	3.04	1.95	0.86
Co$_2$VSn	2.56	0.86	1.07	2.93	2.15	0.33	Rh$_2$CuSn	3.00	0.54	1.18	3.07	1.61	0.30
Co$_2$ZrSn	3.31	0.11	1.16	2.97	1.19	0.34	Rh$_2$MnSn	2.67	0.63	0.83	2.68	1.54	0.26
Co$_2$MnTi	3.09	2.03	2.29	3.27	2.28	1.83	Rh$_2$MnTi	2.71	1.93	2.06	2.88	2.09	1.78
Co$_2$NbZn	3.25	1.80	2.03	3.16	2.27	1.42	Rh$_2$FeZn	2.90	1.38	1.86	2.93	2.21	1.52
Co$_2$TaZn	3.35	2.07	2.15	3.23	2.55	1.54	Rh$_2$MnZn	2.86	1.01	1.71	2.74	1.92	1.34
Co$_2$VZn	3.25	1.93	2.15	3.26	2.57	1.49	Rh$_2$MnZr	2.60	1.70	1.70	2.77	1.86	1.37
Cu$_2$MnAl	1.90	1.44	1.46	2.22	1.92	1.22	Ru$_2$MnNb	2.98	2.09	2.31	3.09	2.41	2.20
Cu$_2$MnIn	1.55	1.10	1.03	1.71	1.59	0.86	Ru$_2$MnTa	3.12	2.23	2.39	3.25	2.47	2.33
Cu$_2$MnSn	1.20	0.39	0.34	1.25	1.16	-0.01	Ru$_2$MnV	2.96	2.21	2.50	3.08	2.55	2.53

Table 1.2: All surface energy data for the X-rich condition in J/m^2

	100		110	111				100		110	111		
Name	X$_2$	YZ	X$_2$YZ	X	Y	Z	Name	X$_2$	YZ	X$_2$YZ	X	Y	Z
Au$_2$MnZn	0.78	1.59	0.91	0.91	1.62	1.11	Fe$_2$MnAl	3.10	1.75	2.59	3.15	4.93	2.36
Co$_2$FeAl	2.97	2.35	2.29	2.91	3.35	2.37	Ga$_2$MnCo	0.49	1.87	0.46	0.28	1.34	0.86
Co$_2$HfAl	2.95	2.18	2.02	2.39	2.80	2.61	Mn$_2$CoAl	1.80	1.21	1.63	1.83	2.53	1.73
Co$_2$MnAl	3.10	1.96	2.36	3.07	3.45	2.51	Mn$_2$VAl	2.53	2.07	2.44	2.64	3.48	2.87
Co$_2$CrAl	2.87	2.23	2.60	3.37	3.43	1.89	Mn$_2$PtCo	1.74	2.37	1.96	1.37	2.23	2.85
Co$_2$NbAl	2.76	2.58	2.10	2.79	3.25	2.10	Mn$_2$CoCr	2.13	3.57	2.45	2.40	3.12	4.15
Co$_2$TaAl	2.73	2.92	2.27	2.73	3.62	2.21	Mn$_2$VGa	2.28	1.49	1.87	2.32	2.97	1.90
Co$_2$TiAl	2.99	2.59	2.26	2.63	3.25	2.87	Mn$_2$PtPd	2.01	2.13	2.02	1.77	2.56	2.65
Co$_2$VAl	2.83	2.87	2.27	3.03	3.61	2.24	Mn$_2$PtRh	1.66	2.33	1.76	1.23	2.39	2.78
Co$_2$ZrAl	2.93	1.83	1.88	2.39	2.42	2.42	Mn$_2$PtV	1.96	3.44	2.06	1.33	2.46	3.00
Co$_2$CrGa	2.82	1.63	1.75	3.00	2.67	1.10	Ni$_2$FeAl	2.01	2.33	1.76	2.17	3.08	1.93
Co$_2$FeGa	2.84	1.74	1.79	2.73	2.84	1.51	Ni$_2$FeGa	1.92	1.77	1.33	2.07	2.63	1.23
Co$_2$HfGa	2.84	1.58	1.47	2.05	2.17	1.65	Ni$_2$MnGe	1.72	1.11	0.92	1.77	2.01	0.83
Co$_2$VGa	2.68	2.17	1.85	1.22	3.05	1.44	Pd$_2$MnAu	2.03	2.03	2.46	2.18	2.21	2.30
Co$_2$MnGa	2.96	1.34	1.87	2.94	2.88	1.71	Pd$_2$MnCu	2.01	2.57	2.34	2.20	2.64	2.84
Co$_2$TiGa	2.90	1.89	1.81	2.47	2.83	2.15	Pd$_2$MnGe	1.36	2.09	1.63	1.72	2.52	1.81
Co$_2$FeGe	2.28	1.39	1.18	2.36	2.26	0.59	Pd$_2$MnSb	1.51	1.79	1.69	2.04	2.48	1.54
Co$_2$MnGe	2.75	1.24	1.52	2.79	2.65	1.14	Pd$_2$MnSn	1.43	1.96	1.84	2.12	2.97	2.11
Co$_2$FeSi	2.40	2.44	1.86	2.66	3.13	1.89	Pd$_2$MnZn	1.79	2.65	2.29	2.66	3.57	3.15
Co$_2$MnSi	2.88	2.17	2.15	3.09	3.47	2.28	Pt$_2$MnZn	1.58	1.95	1.24	1.23	2.30	1.79
Co$_2$TiSi	2.74	2.32	1.95	2.55	3.32	2.69	Rh$_2$MnAl	2.18	2.34	1.95	2.10	3.56	2.82
Co$_2$HfSn	2.63	0.98	1.13	1.91	1.84	0.65	Rh$_2$MnGe	1.67	1.59	0.81	1.38	2.26	1.07
Co$_2$MnSn	2.85	0.73	1.08	2.73	2.20	0.67	Rh$_2$MnHf	1.63	2.94	1.79	1.64	3.17	2.75
Co$_2$NbSn	2.20	1.09	0.96	2.04	1.98	0.02	Rh$_2$MnPb	2.12	0.90	1.02	2.11	1.79	0.71
Co$_2$TiSn	2.63	1.08	1.27	2.46	2.30	1.14	Rh$_2$MnSc	1.95	1.99	1.64	1.84	3.16	2.07
Co$_2$VSn	2.41	1.01	1.07	2.76	2.32	0.50	Rh$_2$CuSn	2.36	1.18	1.18	2.34	2.34	1.03
Co$_2$ZrSn	2.68	0.74	1.16	2.25	1.91	1.06	Rh$_2$MnSn	1.90	1.39	0.83	1.79	2.43	1.14
Co$_2$MnTi	2.54	2.57	2.29	2.64	2.91	2.46	Rh$_2$MnTi	1.70	2.94	2.06	1.72	3.25	2.94
Co$_2$NbZn	2.91	2.13	2.03	2.78	2.66	1.80	Rh$_2$FeZn	2.40	1.88	1.86	2.35	2.79	2.09
Co$_2$TaZn	2.94	2.48	2.15	2.76	3.02	2.01	Rh$_2$MnZn	2.30	1.57	1.71	2.09	2.57	1.99
Co$_2$VZn	2.96	2.22	2.15	2.92	2.90	1.82	Rh$_2$MnZr	1.66	2.64	1.70	1.68	2.95	2.46
Cu$_2$MnAl	1.64	1.70	1.46	1.91	2.22	1.53	Ru$_2$MnNb	2.65	2.42	2.31	2.71	2.79	2.58
Cu$_2$MnIn	1.64	1.00	1.03	1.81	1.48	0.75	Ru$_2$MnTa	2.66	2.69	2.39	2.72	2.99	2.85
Cu$_2$MnSn	1.30	0.28	0.34	1.37	1.04	-0.13	Ru$_2$MnV	2.65	2.52	2.50	2.72	2.91	2.89

YZ terminations and 2.88 J/m^2 and 2.17 J/m^2 for X-rich X$_2$ and YZ terminations respectively. Like the results of Khosravizadeh *et al.* who predict surface energies of 0.36 J/m^2 for the X$_2$ termination and 0.42 J/m^2 for the YZ termination respectively, our results also predict an increase in the YZ termination and a decrease in the X$_2$ termination surface energies of Co$_2$FeSi in comparison to the surface energies of Co$_2$MnSi, however we only observe a preference for the X$_2$ termination under the X-rich condition. In both X-rich and X-poor conditions, it can be seen that the YZ-terminated slabs overall have lower surface energies compared to the X$_2$-terminated slabs. This difference is emphasized under the X-poor (Y and Z rich) condition, where the surface energies of the YZ-terminated slabs are minimized. As expected, the X$_2$ terminated slabs under the X-rich condition have surface energies similar to that of bulk Co.

Within the YZ-terminated slab surface energies, another interesting trend shown in Fig 1.4 is the decreasing surface energy with increasing group number of the Z atom. As the number of valence electrons in the Z atom increases, the surface energy trends downward. Furthermore, within each group, the surface energy also decreases with increasing period number and atomic radius. When these trends culminate in the group 13 and 14 atoms with the larger atomic radii under the X-poor condition, the surface energy falls below the (100) MgO surface energy, revealing promising candidates able to be grown on an MgO substrate, including Co$_2$\{Zr, Hf, Ti, Mn\}Sn, Co$_2$MnGe, and Co$_2$\{Hf, Mn, Ti\}Ga.

1.3.3   (110) Surface Orientation

Fig 1.5 shows the (110) surface energies of the Co$_2$ based compounds plotted against the Z atom in order of increasing group number. Since the (110) oriented slabs are stoichiometric, the surface energy does not depend on the chemical potential and hence only has one value for the surface energy. The (110) surface energies follow a trend similar to that in the (100) orientation. Namely, there is also a trend of decreasing surface energy with increasing group and period number
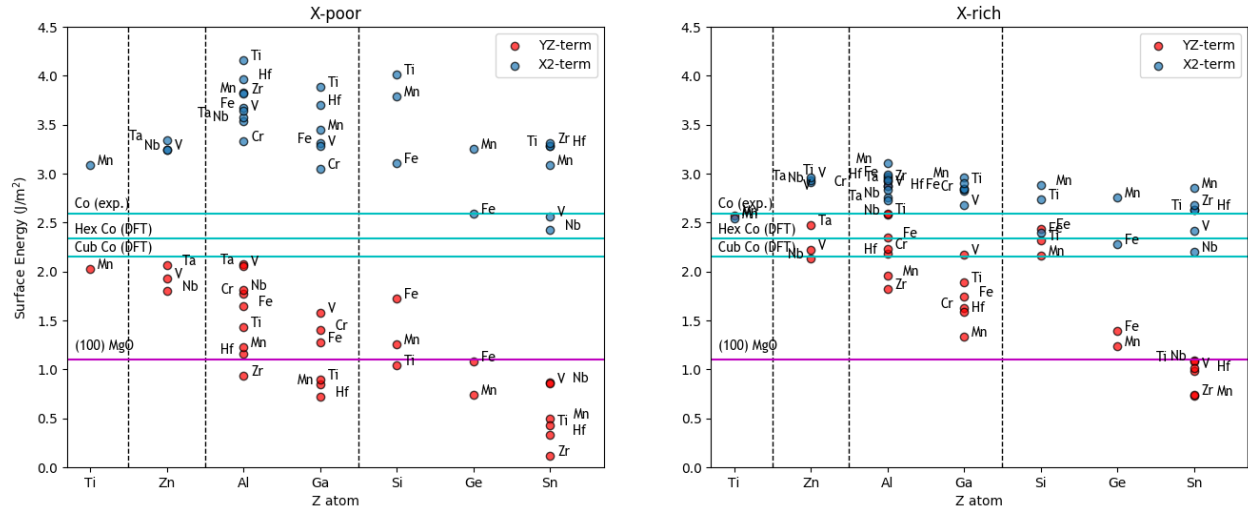
Figure 1.4: Surface energy plotted against Z atom for all Co_2YZ compounds at the (100) surface for both X rich (right) and X poor (left) conditions. The Y atom is listed next to each data point. The dashed lines separates the Z atoms by group number. The magenta and cyan lines represent the surface energy of (100) MgO[48] and bulk Co[49] respectively.

and atomic radius of the Z atom. Overall, the surface energies in the (110) direction are higher than those of the (100) direction due to the higher number of bonds cleaved at the surface. Because of this, only some of the Sn-containing compounds fall below the (100) MgO surface energy.

1.3.4 (111) Surface Orientation

Fig 1.6 shows the (111) surface energies of the Co_2 based compounds plotted against the Z atom in order of increasing group number. The left and right plots show the surface energy values under the X-poor and X-rich conditions. Our results for Co_2VGa predict the same termination preference as that predicted by Han *et al.* who calculated surface energy values of 1.63 J/m^2, 4.58 J/m^2, and -0.22 J/m^2 for the X, Y, and Z terminations in the X-poor condition and 1.64 J/m^2, 4.58 J/m^2, and 1.09 J/m^2 for the X, Y, and Z terminations in the X-rich condition respectively.[35] We calculated surface energy values of 1.91 J/m^2, 2.36 J/m^2, and 0.75 J/m^2 for X-poor X, Y, and Z terminations and 1.22 J/m^2, 3.05 J/m^2, and 1.44 J/m^2 for X-rich X, Y, and Z terminations respectively. However, unlike the results of Han *et al.*, we find that the X termination can become

12
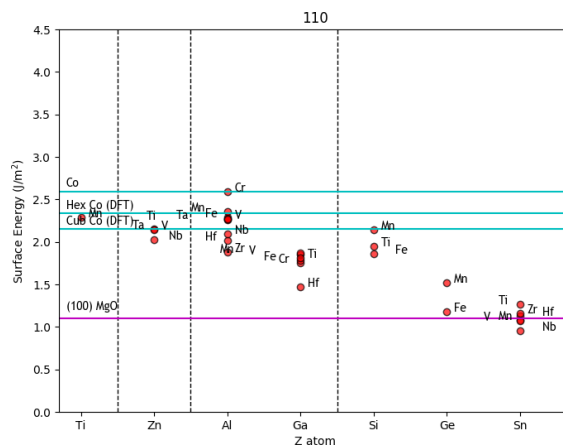
Figure 1.5: Surface energy plotted against Z atom for all Co_2YZ compounds at the (110) surface. Since the slabs are stoichiometric, there is no rich/poor condition. The Y atom is listed next to each data point. The dashed lines separates the Z atoms by group number. The magenta and cyan lines represent the surface energy of (100) MgO[48] and bulk Co[49] respectively.

the preferred surface termination under the X-rich condition. In both X-poor and X-rich conditions, the Z-terminated slabs have the lowest surface energies of the three terminations. As in the (100) direction, the Heusler compound surfaces show a preference for terminations containing the Z atom and a disfavor for terminations containing the X atom. The X-terminated slab surface energies are also comparable to bulk Co and all the slabs approach the bulk Co surface energy value in the X-rich condition.

Within the Z-terminated slab surface energies, the surface energies demonstrate a similar trend to that in the (100) and (110) orientation. As the group and period number and atomic radii increase, the surface energy decreases. In the X-poor condition, this trend leads to the several group 13 and 14 Z atom containing slabs that have surface energies lower than (100) MgO, including $Co_2\{Zr, V, Ti, Mn\}Sn$, $Co_2\{Fe, Mn\}Ge$, and $Co_2\{Hf, V, Cr, Fe, Ti\}Ga$. Interestingly, the Ge and Sn containing slabs still demonstrate low surface energies in the X-rich condition, continuing to stay under the (100) MgO surface energy.
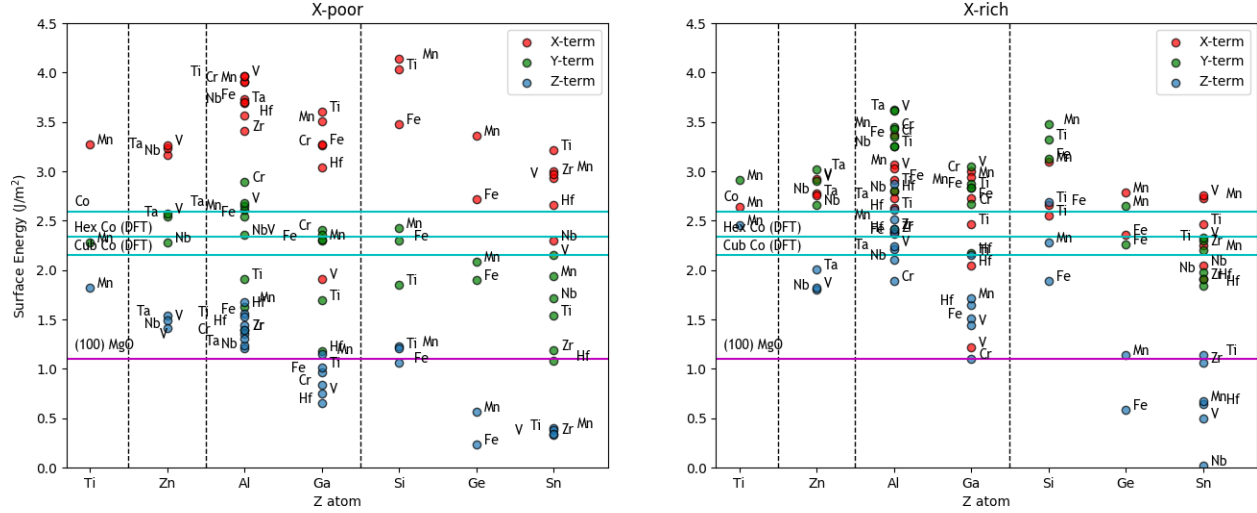
Figure 1.6: Surface energy plotted against Z atom for all Co_2YZ compounds at the (111) surface for both X rich (right) and X poor (left) conditions. The Y atom is listed next to each data point. The dashed lines separates the Z atoms by group number. The magenta and cyan lines represent the surface energy of (100) MgO[48] and bulk Co[49] respectively.

1.4 Conclusion

In this work, we use high-throughput first-princples DFT calculations to study the surface energies of magnetic full Heusler alloys. We find a trend of decreasing surface energy with increasing number of valence electrons and atomic radius of the Z atom. We find that terminations containing a Z atom in the X-poor condition in both (100) and (111) tend to have the lowest surface energies of all terminations. The culmination of this trend allows us to identify 22 Heusler compounds with surface energies lower than that of (100) MgO, corresponding to X-poor (100) YZ-terminated Co_2\{Zr, Hf, Ti, Mn\}Sn, Co_2MnGe, and Co_2\{Hf, Mn, Ti\}Ga, X-poor (111) Z-terminated Co_2\{V, Zr, Ti, Mn\}Sn, Co_2\{Fe, Mn\}Ge, Co_2\{Hf, V, Cr\}Ga, and X-rich (111) Z-terminated Co_2\{Nb, V, Hf, Mn\}Sn, and Co_2FeGe. In future works, the magnetic anisotropy of each termination could be studied to explore any relationship between the magnetic properties and surface energies.

Chapter 1, in full, is currently being prepared for submission for publication of the material. Wong, Joseph; Nazir, Safdar; Yang, Kesong. The thesis author was the primary investigator and author of this material.

Chapter 2

Machine Learning Analysis of Hybrid Perovskites

2.1 Introduction

High throughput computational materials design has experienced a surge of research attention in recent years due to rapid expansion of computing resources and development of materials modeling software tools.[50, 51] Such developments include high-throughput density functional theory (DFT) calculations,[41, 52] materials properties repositories,[53] and the materials genome initiative.[44, 54] More recently, machine learning (ML) techniques have been used to further accelerate materials properties prediction and materials discovery.[55] ML techniques reduce the computational costs associated with quantum mechanical modeling methods in exchange for small losses in accuracy by extrapolating from the descriptors of previously generated data. ML technology has been used in a variety of materials design applications, including polymer chains,[55] vanadium selenites,[56] and ternary compounds.[57]

ML has also been applied in the design of hybrid organic-inorganic perovskites (HOIP) of the form ABX_3 or $A_2B'B''X_6$, where A is an organic cation such as methylammonium (MA: $CH_3NH_3^+$), B is a transition metal cation such as Pb^{2+} and Sn^{2+}, and X is a monovalent anion such as Cl^-,

Br$^-$, and I$^-$.[58] HOIP have demonstrated strong promise as light absorbing materials in solar cell applications due to high power conversion efficiencies (PCE) with records reaching up to 22.1%,[59] low cost fabrication requirements, and tunable band gaps.[60, 61, 62, 63] Despite tremendous research progress over the past decade, HOIP still face large obstacles inhibiting implementation in industry. These obstacles include the toxicity of the lead atom in the best performing HOIP[64] and low stability exacerbated in ambient conditions.[65, 66, 67] High throughput DFT screening of HOIP materials is one route to exploring the complex and diverse space of HOIP compositions,[68, 69] however the computational resources required to explore the desired chemical search space can easily become prohibitive when considering the many structural types of HOIP. In light of these challenges, ML presents tremendous opportunity in the discovery of stable, lead-free HOIP with its ability to explore a complex and diverse space of HOIP structures and compositions while remaining computationally feasible. Several studies applying the ML approach in this regard have been performed, but have relied heavily on structural features of the perovskite material, either limiting the study to one space group, employing features that require explicit information regarding atomic coordinates, or creating structural templates to artificially produce structural features.[58, 70, 71, 72]

In this work, we train a ML model to predict the band gaps (E_g), formation energies (E_F), and charge carrier effective mass (m_e^*, m_h^*) of both single and double HOIP belonging to 24 different structural types using primarily features derived from elemental composition. From an analysis of 87 compositional features, 208 single perovskites, and 1694 double perovskites, we identify several key features in the prediction of m_e^*/m_h^*, E_g, and E_F, including transition metal fraction, number of valence electrons, ionic character, and electronegativity. Using a meta ensembling technique, we achieve root mean squared errors (RMSE) of 0.09, 0.49, 0.64, 0.74, and 0.63 for PBE E_g, HSE E_g, E_F, m_e^*, and m_h^* respectively for single perovskites, and 0.05, 0.32, 0.48, 0.60, and 0.73 for E_F, PBE E_g, HSE E_g, m_e^*, and m_h^* respectively for double perovskites.

Figure 2.1: Overall workflow schematic from raw data to ML prediction.

2.2 Computational Details

Our workflow for converting the input data to ML predictions is shown in Figure 2.1. The HOIP m_e^*, m_h^*, HSE E_g, PBE E_g, and E_F target data are obtained from previous DFT calculations. We sorted the data into 208 single perovskite and 1694 double perovskite data points. We manually selected 55 features and extracted 32 compositional features using the matminer tool as shown in table 2.1.[73] A normalized two dimensional array containing the feature values for each data point is used as the input to our ML model. To determine feature importance values, we take the average of the feature importances calculated from decision tree, bagging, random forest, and extreme gradient boosting.[74, 75]

We employ a meta ensembling technique to make ML predictions as shown in Figure 2.2. Meta ensambling, or stacking, is a technique that takes the predictions of base learners as features for the meta models to improve the overall predictive capabilities. The initial 87 input features are passed to a series of base models which each make their own individual predictions of the target variables. In our base layer, we use several models implemented in scikit-learn, including SVR, ridge regression, lasso, linear regression, k-nearest neighbors regression, decision tree regression, bagging, and random forest.[74] The predictions from the base layer are then passed to models in the meta layer which likewise make their own predictions of the target variables. In our meta layer, we use also use several models from scikit-learn, including bagging, adaboost, and random forest in addition to extreme gradient boosting implemented in XGBoost.[74, 75] Finally, the meta layer predictions are averaged to yield a final predicted value for the target variable.
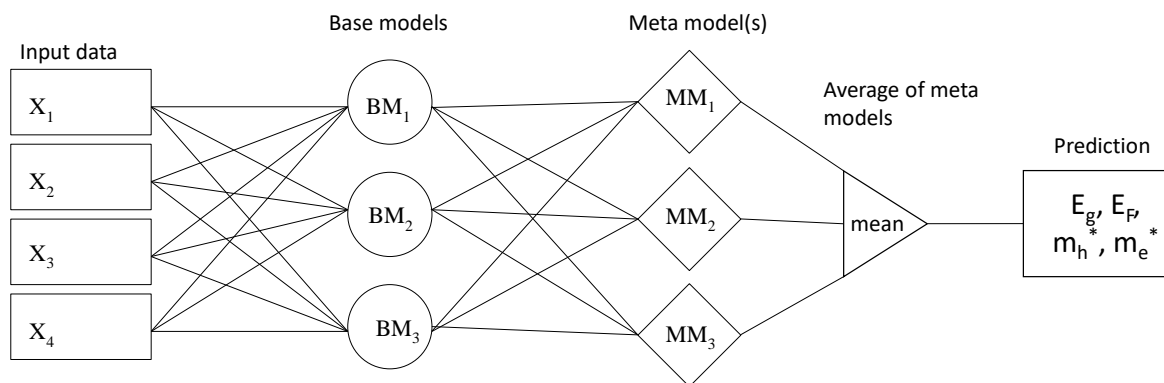
Figure 2.2: Schematic of our machine learning model used in the prediction of target variables.

Table 2.1: List of all 87 descriptors considered in the ML model

Tolerance factor	group num B'	radius A	sval B'
Octahedral factor	group num B"	radius B'	sval B"
minimum oxidation state	period num B'	radius B"	pval B'
maximum oxidation state	period num B"	radius X	pval B"
range oxidation state	period num X	radius ratio A/B'	dval B'
std dev oxidation state	valence num B'	radius ratio A/B"	dval B"
isolated chem pot B'	valence num B"	radius ratio A/X	dval X
isolated chem pot B"	valence num X	radius ratio B'/X	fval B'
isolated chem pot X	atomic num B'	radius ratio B'/B"	fval B"
avg anion electron affinity	atomic num B"	radius ratio B"/X	mass A
minimum EN difference	atomic num X	Mulliken EN B'	mass B'
maximum EN difference	avg s valence electrons	Mulliken EN B"	mass B"
range EN difference	avg p valence electrons	Mulliken EN X	mass X
mean EN difference	avg d valence electrons	Pauling EN B'	0-norm
std dev EN difference	avg f valence electrons	Pauling EN B"	2-norm
compound possible	frac s valence electrons	Pauling EN X	3-norm
max ionic char	frac p valence electrons	Ionization Potential B'	5-norm
avg ionic char	frac d valence electrons	Ionization Potential B"	7-norm
transition metal fraction	frac f valence electrons	Ionization Potential X	10-norm
bulk chem pot B'	HOMO energy	Electron Affinity B'	gap AO
bulk chem pot B"	LUMO energy	Electron Affinity B"	
bulk chem pot X	band center	Electron Affinity X	
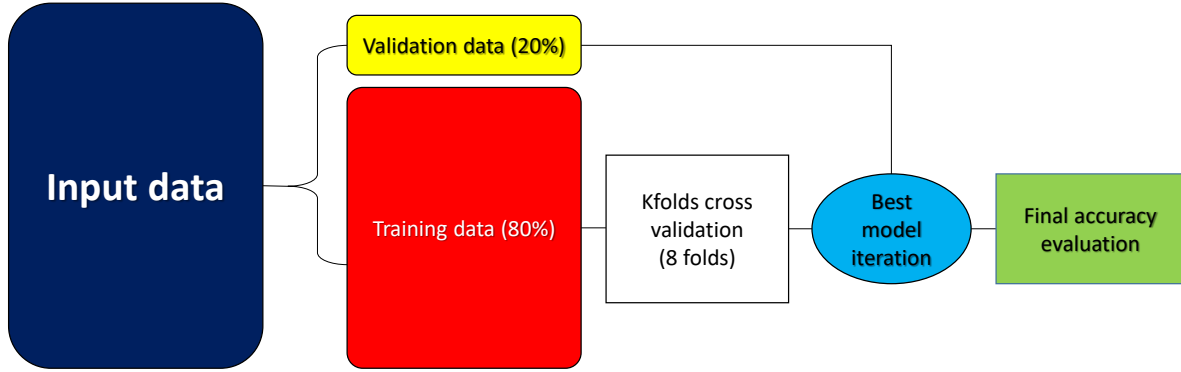
Figure 2.3: A flow diagram of our ML model training process.

To evaluate the performance of our ML model, we calculate the root mean squared error (RMSE) between ML prediction and DFT calculated values of a validation set containing 20% of the total data. The equation for RMSE is given as

$$RMSE = \sqrt{\frac{\Sigma_i^N (y_p - y_o)^2}{N}},$$ (2.1)

where N is the total number of data points, y_p is the predicted target value, and y_o is the observed, or true target value. A lower RMSE value indicates a higher accuracy ML model and a RMSE value of 0 indicates a perfect ML model. To avoid overfitting our model to the data, we divide the initial data into 80% training and 20% test data and measure the RMSE of the training data using k-folds cross validation as shown in Figure 2.3. In this technique, the data is divided into k number of folds, where each fold contains a set of test data and a set of training data. The test indices of each fold do not overlap with each other. The ML model is trained on each fold and its RMSE is measured according to predictions on the test data of each fold. In this work, we use the iteration with the lowest RMSE of 8 folds to make predictions on the validation set consisting of 20% of the initial input data. We consider the RMSE calculated from the predictions on this validation set as an accurate representation of how the model will perform on unseen data.
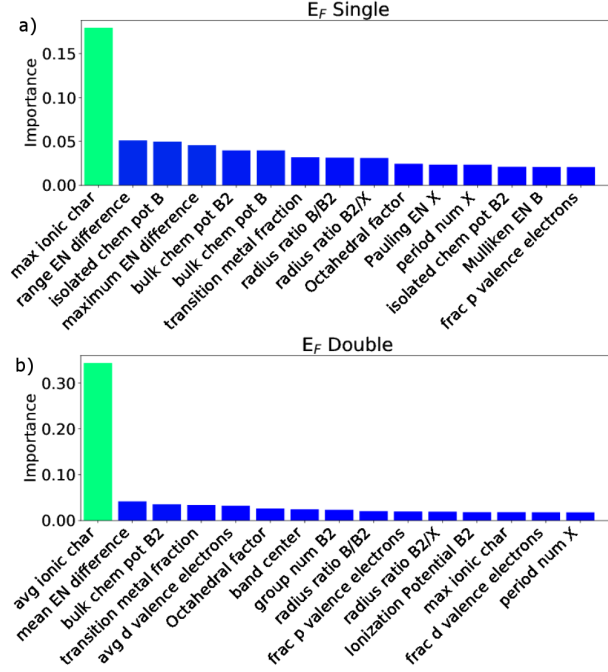
Figure 2.4: Relative feature importances for E_F for a) single and b) double perovskites.

2.3 Results

2.3.1 Formation Energy Feature Importances and Model Accuracy

A list of relative feature importances for E_F for single and double perovskites are shown in Figure 2.4. For both single and double perovskites, the ionic character is the one feature that stands above the rest as the most important descriptor in the prediction of E_F. For single perovskites, this descriptor is more specifically the max ionic character, while for double perovskites, it is the average ionic character. This suggests that the degree of ionic bonding within a perovskite material is the dominant factor that leads to highly stable structures.

Figure 2.5 shows a plot of predicted E_F values against observed E_F values. We obtain a RMSE value of 0.09 for single perovskites and 0.05 for double perovskites, corresponding to a mean absolute error (MAE) of 0.3 eV/atom and 0.22 eV/atom respectively. Compared to the E_F results of Meredig *et al.* and Askerka *et al.* who obtained MAE values of 0.12 eV/atom and 0.11 eV/atom respectively, the error for E_F is relatively high.[57, 71] The low RMSE value compared
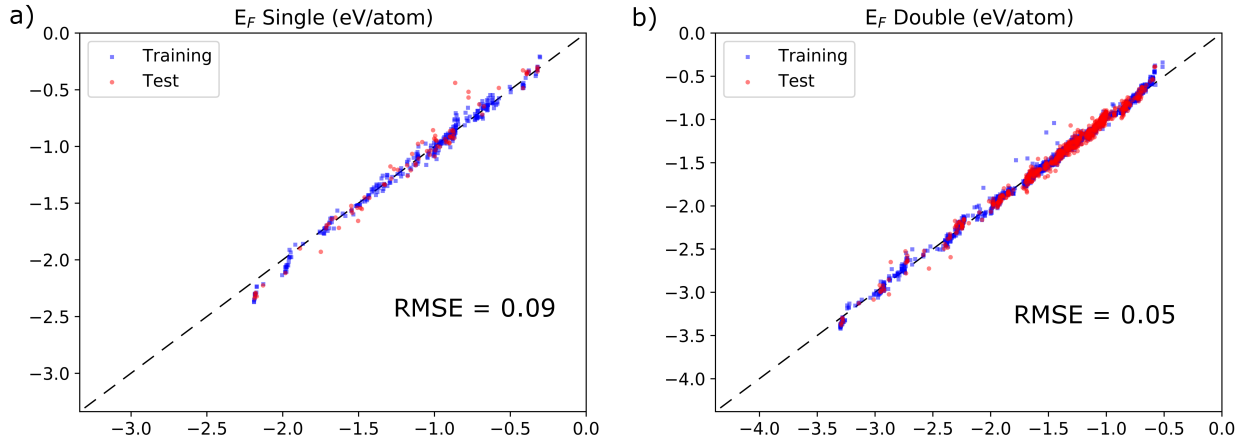
Figure 2.5: Predicted values plotted against observed values for a) single perovskite and b) double perovskite E_F. The dashed line corresponds to 0 error between the predicted and observed values.

to E_g and m^* suggests that the ionic character of hybrid perovskites is a very strong predictor of E_F. The RMSE of single perovskites is slightly higher than double perovskites likely due to fewer available training data points. Nonetheless, our results suggest that even with a small dataset, the E_F can be predicted with a some degree of accuracy.

2.3.2   Band Gap Feature Importances and Model Accuracy

A list of relative feature importances for E_g PBE and E_g HSE for single and double perovskites are shown in Figure 2.6. Unlike Figure 2.4, there is no one distinct feature that dominates the rest. Instead, there are a few descriptors that are considerably important with a variety of others that are slightly important in determining the band gap. Ionic character descriptors are seen to rank highly for HSE and PBE E_g in double and single perovskites, especially for double perovskites. Like the case for E_F, this suggests the degree of ionic bonding influences the perovskite band gap. The transition metal fraction and the fraction of d valence electrons are found to rank highly in the feature importances of double perovskites, but not very highly in single perovskites. This difference likely arises because the two B atoms in double perovskites leave one more degree of freedom for transition metal selection allowing for a higher information resolution regarding the transition

21
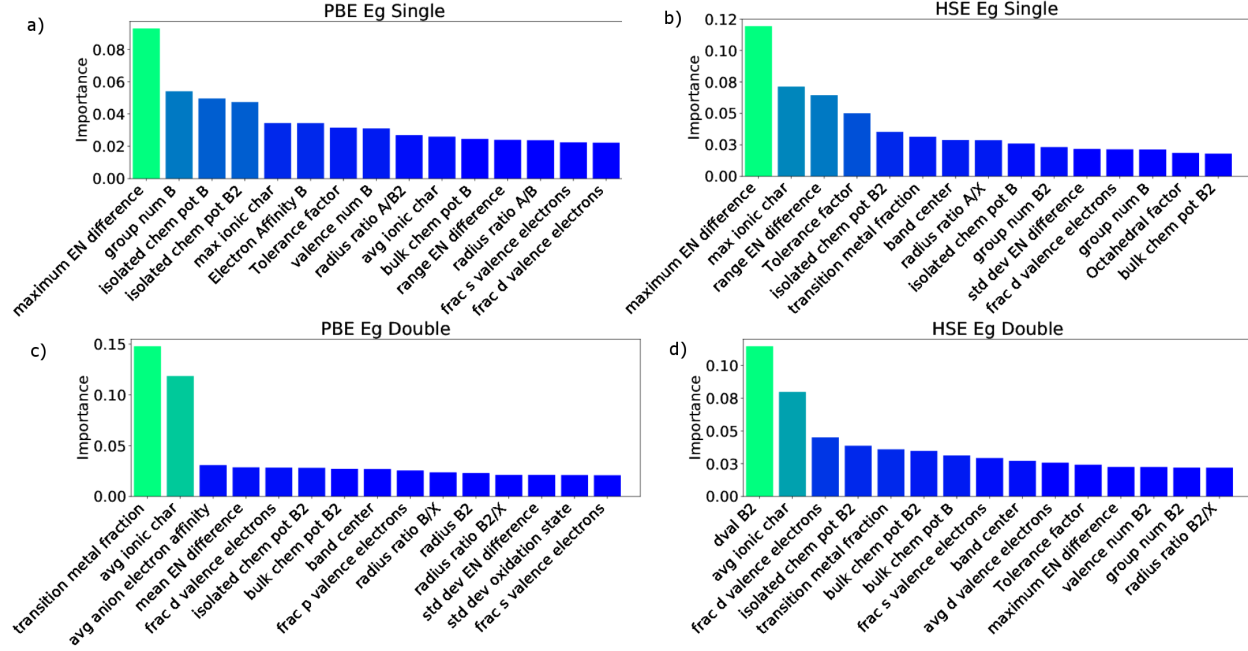
Figure 2.6: Relative feature importances for a) PBE and b) HSE E_g for single perovskites and c) PBE and d) HSE E_g for double perovskites.

metal content compared to single perovskites. The high ranking of these d valence electron descriptors suggests that the d valence electrons influence the band gap with contributions to band edge states in agreement with previous work by Deng *et al.*[76] In both double and single perovskites, electronegativity-derived features rank highly. These features are likely good indicators of which halide atom is in the material, which has been shown to be an important factor in determining the band gap by Deng *et al.*[76]

Figure 2.7 shows a plot of predicted E_g values against observed E_g values for HSE and PBE band gaps. The results are less accurate than E_F, but still somewhat accurate despite total reliance on compositional features in the training data. The RMSE values are lower in double perovskites likely due to more available training data.

2.3.3 Effective Mass Feature Importances and Model Accuracy

A list of relative feature importances for m_h^* and m_e^* for single and double perovskites are shown in Figure 2.8. Unlike the case for E_g and E_F, the Figure 2.8 does not distinguish any
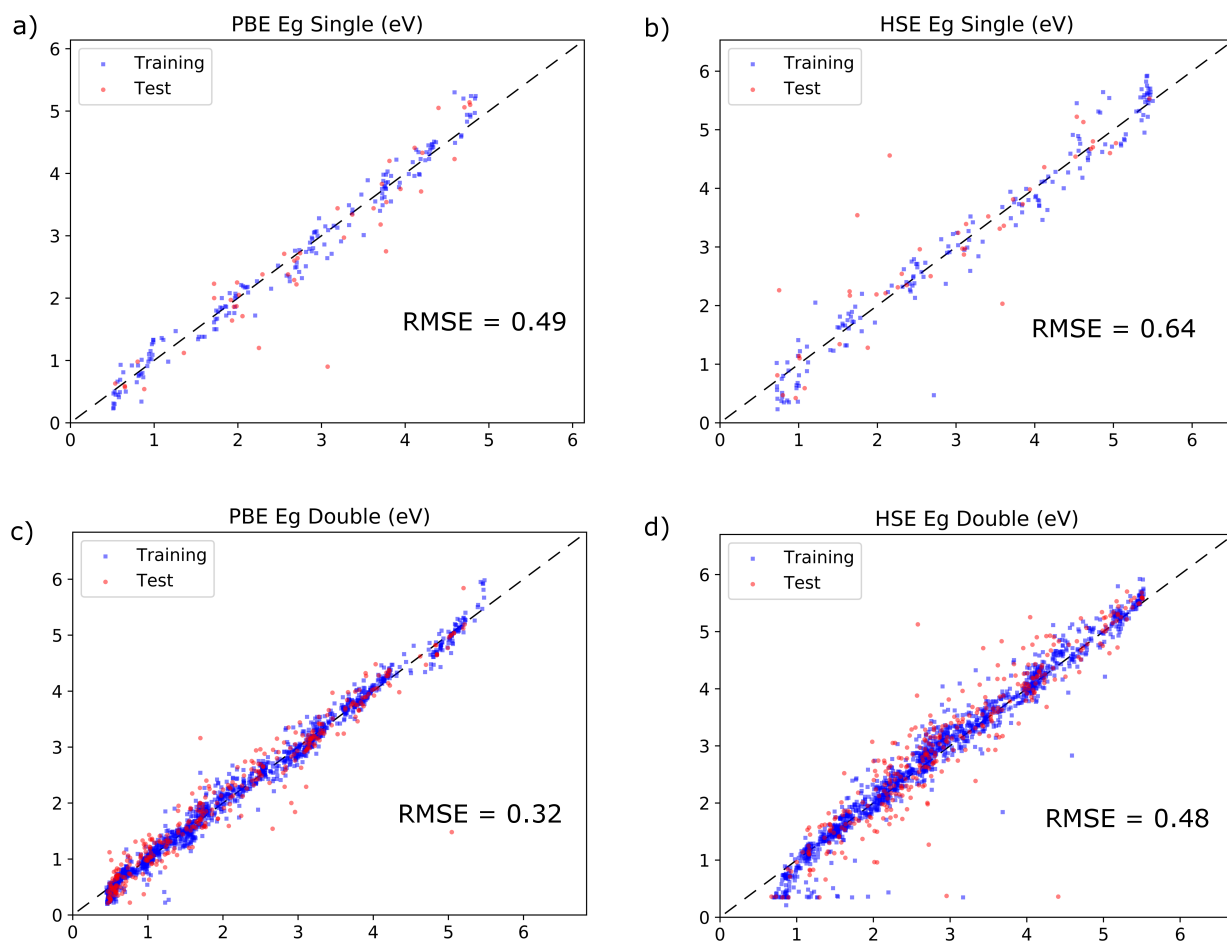
Figure 2.7: Predicted values plotted against observed values for a) PBE and b) HSE for single perovskite E_g and c) PBE and d) HSE for double perovskite E_g. The dashed line corresponds to 0 error between the predicted and observed values.
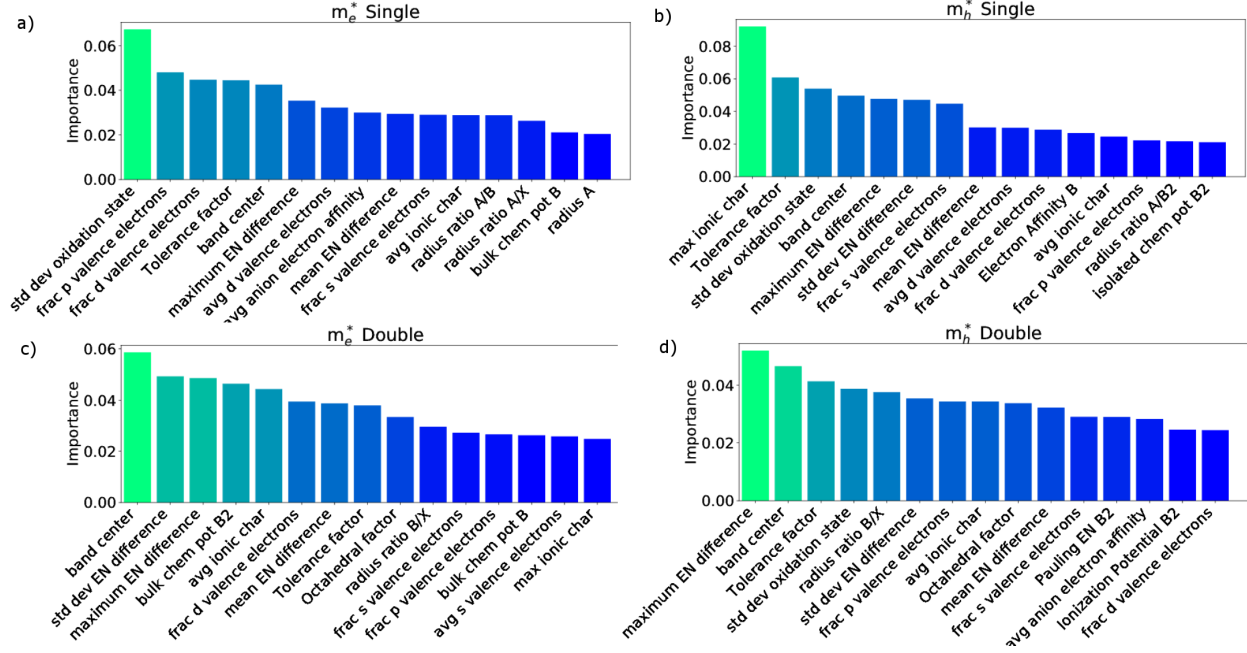
Figure 2.8: Relative feature importances for a) m_e^* and b) m_h^* for single perovskites and c) m_e^* and d) m_e^* for double perovskites.

particular features that stand out from the rest. For both m_h^* and m_e^* in single and double perovskites, electronegativity-derived features are ranked above the rest. In addition, the standard deviation of the oxidation states are also ranked highly. These features suggest that the halide and transition metal choice play an important role in the determination of effective masses. This is in agreement with previous work which has shown that only the inorganic perovskite components contribute to band edge states.[76] The high importance of s, p, and d valence electron fraction in single and double perovskites supports this idea, suggesting that band edge states influence charge carrier mobility. Some structure-related features are also shown to influence the charge carrier mobility, including the tolerance factor and atomic radius ratios. These features could be giving some indication of the bonding environment, which can influence the movement of charge carriers between ions.

Figure 2.9 shows a plot of predicted m_e^* and m_h^* values against observed values. The results show a high RMSE value with a poor alignment of data points to the dashed line, indicating poor model performance and low correlation of the features with the effective mass target values. The low accuracy could originate from the data used to train the model. The effective mass values are
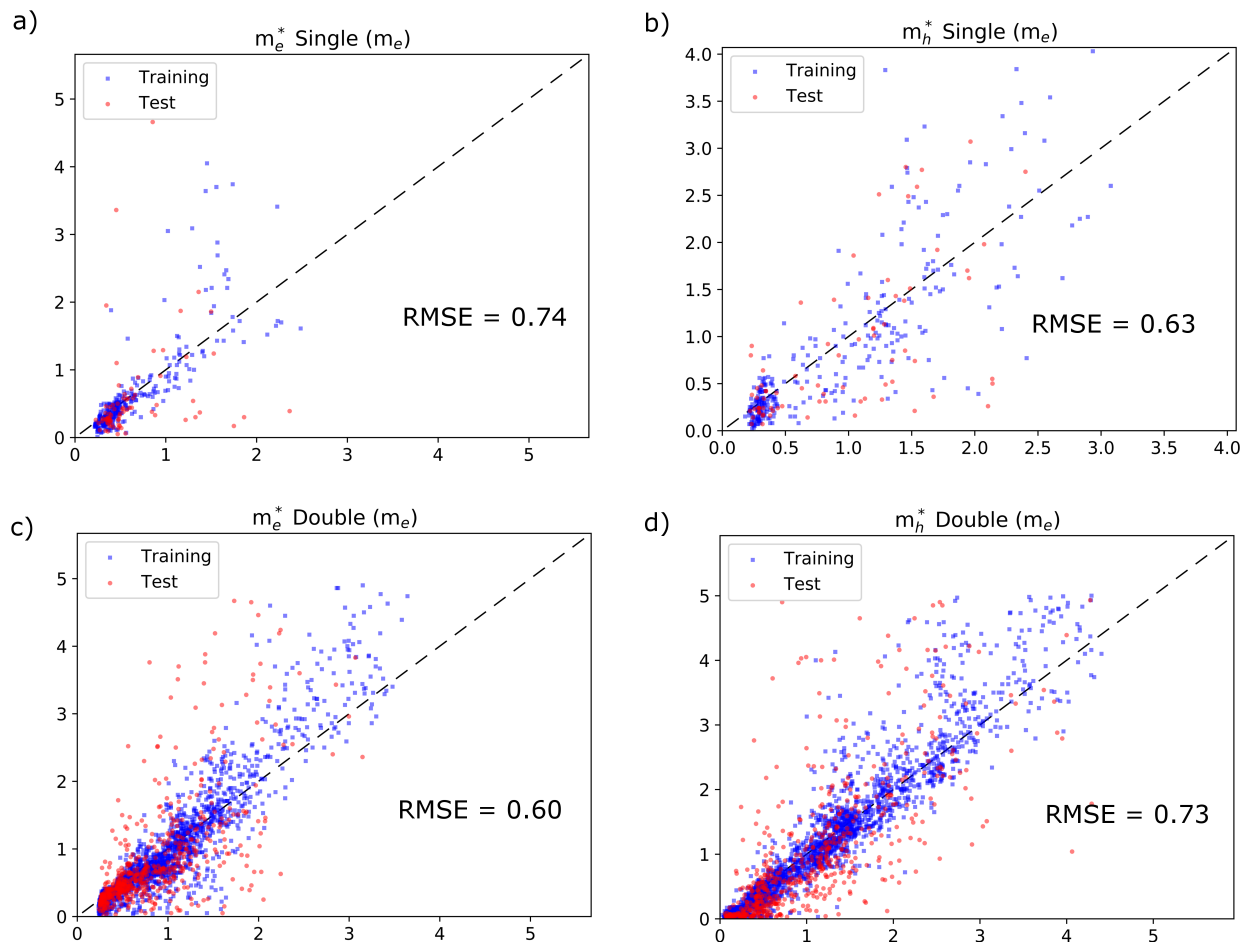
Figure 2.9: Predicted values plotted against observed values for a) m_e^* and b) m_h^* for single perovskites and c) m_e^* and d) m_h^* for double perovskites. The dashed line corresponds to 0 error between the predicted and observed values.

calculated from fits to the band edges, which may not be entirely reliable in calculating accurate effective mass values. Nonetheless, Figure 2.9 shows that the data points follow an upward trend, indicating the model can provide very rough estimates of the effective mass.

2.4   Conclusion

We have demonstrated the ability of a meta ensemble ML model in the prediction of E_F, E_g and m^* using solely compositional features. We achieve RMSE values of 0.09, 0.49, 0.64, 0.74, and 0.63 for PBE E_g, HSE E_g, E_F, m_e^*, and m_h^* respectively for single perovskites, and 0.05, 0.32, 0.48,

0.60, and 0.73 for E_F, PBE E_g, HSE E_g, m_e^*, and m_h^* respectively for double perovskites. We show that the the ionic character of the material is strongly correlated with the E_F, but less so with the E_g of single and double perovskites. The d valence electron-related descriptors are also found to be correlated with E_g, but only in double perovskites. This ML model is one step towards a more generalized approach to high-throughput prediction of hybrid perovskite materials for applications in stable, high performing solar cells. Future directions of this work include implementation of the model in software for rapid prediction of materials of any composition and an exploration of additional structural features extracted or extrapolated from the material composition.

Chapter 2, in full, is currently being prepared for submission for publication of the material. Wong, Joseph; Li, Yuheng; Jiang, Sicong; Yang, Kesong. The thesis author was the primary investigator and author of this material.

Chapter 3

Literature Review of 2D Hybrid Perovskites

3.1 Introduction

Hybrid organic-inorganic halide perovskites have emerged as one class of most promising light-harvesting materials for the next-generation solar cells because of their exceptional optoelectronic properties and low-temperature solution processability that allows for large-scale fabrication. [77, 78, 79, 80, 81, 61, 82, 83, 84, 85, 86, 87, 88, 89, 90, 91, 92, 93, 94, 95, 96, 97, 98, 99, 100, 101, 102, 59, 103, 104, 105, 106, 107, 108, 109] The hybrid halide perovskites are one class of semiconductors in a formula of ABX_3 that comprises a network of corner-sharing BX_6 octahedron. In this structure, A is an organic cation such as methylammonium (MA: $CH_3NH_3^+$); B is a divalent metal cation such as Pb^{2+} and Sn^{2+}, located in the center; and X is a monovalent anion such as Cl^-, Br^-, and I^-. These structural and compositional features determine their exceptional optoelectronic properties such as tunable band gaps,[87, 86, 61, 84, 91, 85, 104] high absorption coefficient,[83, 89, 84, 86, 91, 102] long carrier diffusion length[88, 89, 95, 110] and lifetime,[87, 93, 94, 95, 59, 103, 105, 106] low trap density,[95, 110] and high carrier mobility.[89, 90, 91, 86, 95, 97, 104] Just in the past few years, the power conversion efficiency (PCE) of these halide perovskites solar cells at lab-scale testing has increased from 3.8% to 22.1%.[111]

Despite promising applications of halide perovskites in the photovoltaic industry, three are still several major challenges that inhibit their large-scale industrial applications.[112, 98] These challenges include poor stability in ambient conditions, particularly in the moisture environment, and the demand for lead-free perovskites. For instance, $(MA)PbI_3$ will degrade into MAI and PbI_2 in ambient conditions in which the water molecules will facilitate the degradation process, sharply dropping perovskite thin film absorption in a matter of days.[65] Although encapsulation can mitigate the degradation from water molecules,[113] the hybrid perovskites were considered as intrinsically unstable in the long term due to unfavorable formation enthalpies.[66, 67]

Two-dimensional (2D) layered hybrid perovskites offer a promising solution to overcome this unstability issue.[112, 4, 114, 115] The 2D hybrid perovskites are composed of inorganic metal halide layers interdigitated between bulky organic molecules such as butylammonium (BA: $CH_3(CH_2)_3NH_3^+$). They have demonstrated high materials stability and robustness in the presence of water[115, 116] and reasonable performance and cheap solution processability.[4, 117, 118, 119, 120] Moreover, the interchangability of the large organic cation and the control of layer dimensionality allows for greater tunability and flexibility of the physical and optoelectronic properties.[121, 119] For instance, compared to three-dimensional (3D) hybrid perovskites, the 2D hybrid perovskites show more expandable optoelectronic properties such as larger exciton binding energies, enabling enhanced photoluminescence properties for room-temperature ligh-temitting-diode (LED) applications.[122, 117, 123]

In this review article, we provide an overview of current experimental and theoretical research progress of the 2D hybrid halide perovskites, including their fabrication, characterization, and device performance, as well as the theoretical and computational understanding and design particularly from first-principles density functional theory (DFT) calculations. The challenges and future research directions of this class of materials are also discussed.
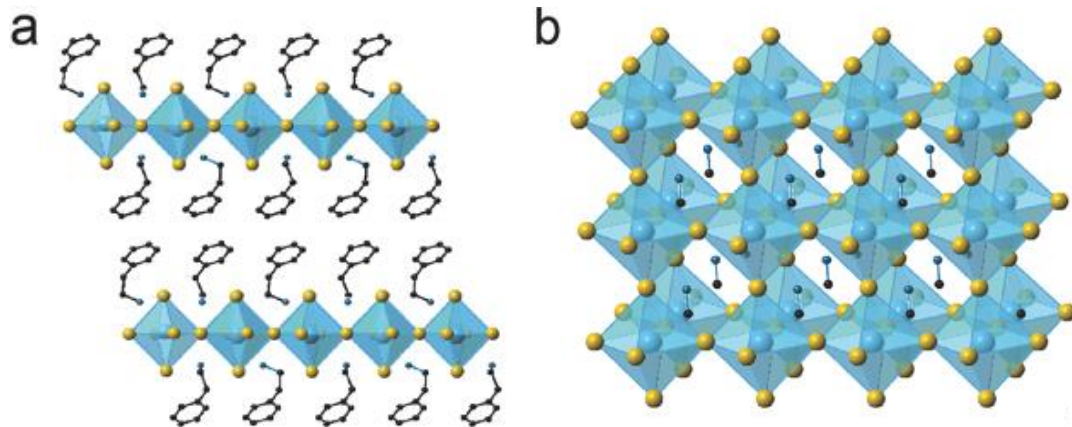
Figure 3.1: Schematic illustration of 2D and 3D perovskites. The yellow and blue balls indicate halide anions (X=I, Br) and Pb cations, respectively. The blue chain indicates organic molecules. Reproduced and adapted with permission from Ref [1].

3.2 Experimental Research

3.2.1 Preparation

Thin films are one critical component of high-performance devices including solar cells and LEDs. The quality of a thin film is mainly determined by its fabrication approach that could significantly influence its optoelectronic properties.[80, 84, 120] Compared to the 3D halide perovskites such as (MA)PbI$_3$ that often requires more complex fabrication methods to achieve high-quality films,[80, 79, 124] the 2D perovskites can form ultra-smooth thin films with high-surface-coverage, fine texture, and few grain boundaries from a simple one-step spin-coating approach mainly due to their 2D nature.[4] To have a clear understanding of the structural difference between the 2D and 3D hybrid perovskites, their structural representations are shown in Figure 3.1. Here we review several common approaches to fabricate thin films of 2D hybrid halide perovskites, including spin coating, mechanical exfoliation, solution-based processing, sonication-assisted synthesis approach, and self-doping based on the template of 2D hybrid perovskites. The schematic illustrations of these approaches are shown in Figure 3.2, and the details of each deposition technique are discussed below.
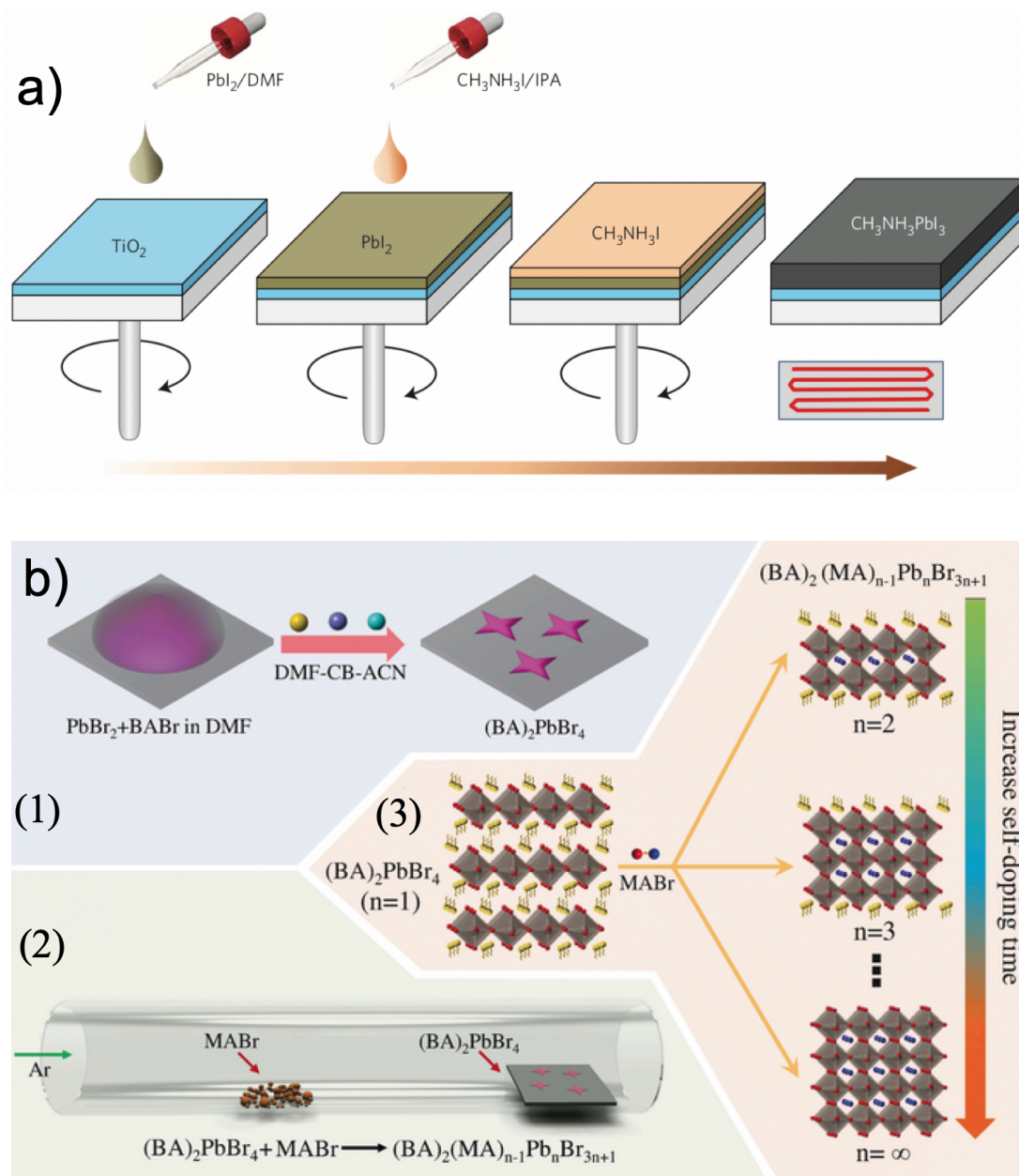
Figure 3.2: Schematic representation of the synthesis of hybrid perovskites. (a) Two-step spin-coating procedure for MAPbI$_3$. PbI$_2$ solution is firstly spin-coated on the mesoporous TiO$_2$ film, and then MAI solution is spin-coated on PbI$_2$. (b) A self-doping approach to prepare two-dimensional hybrid perovskite (BA)$_2$(MA)$_{n-1}$Pb$_n$Br$_{3n+1}$. It contains two sequential steps: (1) synthesis of two-dimensional (BA)$_2$PbBr$_4$ perovskite via a ternary solvent approach and (2) transformation of (BA)$_2$PbBr$_4$ into (BA)$_2$(MA)$_{n-1}$Pb$_n$Br$_{3n+1}$ perovskites via chemical vapor deposition of MABr. The illustration of the structural transformation in the second step is shown in (3). Reproduced and adapted with permission from Refs [83] and [125].

Spin Coating

The spin-coating technique is the most common approach to fabricate thin films of 2D halide perovskites through depositing perovskite solutions on a substrate.[4, 114, 83, 126, 127, 128, 129, 130, 120, 131, 121, 132] The halide perovskite solutions are typically prepared by dissolving organic and inorganic precursors in a dimethylformamide (DMF) solvent.[4, 117, 130, 132, 133, 121, 134] For example, Kanatzidis' research team synthesized 2D Ruddlesden–Popper layered perovskites, $(BA)_2(MA)_{n-1}Pb_nI_{3n+1}$ (n=1-4), from a stoichiometric reaction between PbI_2, MAI, and BA, and fabricated high-quality thin films through spin-coating perovskite solutions on mesoporous TiO_2 substrates.[4] The 2D films were formed immediately after spin-coating at room temperature, and the inorganic $[Pb_nI_{3n+1}]^-$ layers were found perpendicular to the substrate, which is likely beneficial for efficient hole diffusion. The perovskite solutions were prepared by dissolving perovskite powders in the DMF solvent. The synthesis of perovskite powers can be summarized as following several steps: i) dissolve PbO powder in a mixture of aqueous HI and an H_3PO_2, forming a bright-yellow solution; ii) add solid MAI to the hot solution, which initially causes a precipitation of a black powder and the powder rapidly redissolves under stirring; iii) add n-$CH_3(CH_2)_3NH_2$ and left the solution to cool to room temperature, allowing for a crystallization of perovskite. By using a similar fabrication route, Kanatzidis' research group also synthesized 2D Sn-based Ruddlesden–Popper perovskite $(BA)_2(MA)_{n-1}Sn_nI_{3n+1}$ (n=1-5).[114] This series of compounds were synthesized from a stoichiometric reaction of $SnCl_2\cdot2H_2O$, MAI, and BAI in an excess of aqueous HI and H_3PO_2 solutions. In this work, H_3PO_2 was used to suppress the oxidation of I^- to I_2 or I_3^-, as well as the oxidation of Sn^{2+} to Sn^{4+}; and a careful weighing of these starting materials in a ratio of 2:(n-1):n of BAI:MAI:SnCl$_2$ was required to avoid the formation of a mixture of different multilayered products. Moreover, a stoichiometric amount of BAI is found to be necessary to obtain pure compounds, unlike the half-stoichiometric amount of BA in their 2D Pb-based perovskites.[123]

By using the similar spin-coating approach, other 2D perovskite thin films have also been fabricated, including the quasi-2D perovskite $(PEA)_2(MA)_{n-1}Pb_nBr_{3n+1}$ (n=1-4) using phenylethy-

lammonium (PEA: $C_6H_5C_2H_4NH_3$) cations,[117, 118, 119, 135, 120] $(MA)_2Pb(SCN)_2I_2$,[130] $(C_6H_{11}NH_3)_2PbBr_4$ and $(C_6H_{11}NH_3)_2PbI_4$,[132, 132] $(PEA)_2PbZ_{4(1-x)}Y_{4x}$ (Z, Y = Cl, Br, or I),[133] and $(R-(CH_2)_nNH_3)_2PbX_4$.[121] Using a spin-coating approach, Cortecchia $et\ al.$ fabricated $(PEA)_2(MA)_{n-1}Pb_nI_{3n+1}$ films and found that these 2D perovskite films exhibit heterogeneous dimensionality phases using cathodoluminescence microscopy.[136] Specifically, $n = 1$ perovskites preferentially self-assembles near edges of $n = 2$ grains while higher dimensionality phases crystallize in the intergrain regions.

In addition to the simplicity, the spin-coating method also allows for some flexibility to the growth of 2D perovskite, enabling a control of crystal and grain morphology, which includes (i) layer orientation,[137] (ii) grain size,[115] (iii) composition,[138] and (iv) dimensionality,[139, 140] which are discussed as below.

(i) The first feature is that the layer orientation of 2D perovskite thin films can be controlled by varying the deposition solvent or spin speed. For instance, Cao $et\ al.$ demonstrates that thin films of $(BA)_2(MA)_{n-1}Sn_nI_{3n+1}$ (n=1-5) orient the $\{(CH_3NH_3)_{n-1}Sn_nI_{3n+1}\}^{2-}$ slabs parallel to the substrate when using dimethyl sulfoxide (DMSO) solvent, while this orientation can be perpendicular to the substrate when N,N-dimethylformamide (DMF) solvent is used.[114] In the case of $(BA)_2(MA)_{n-1}Pb_nI_{3n+1}$ (n=1-4), the DMF solvent was used,[4] and the $[Pb_nI_{3n+1}]$ slabs of thin films were also found perpendicular to the substrate, favoring charge transport, which is beneficial for the solar cell applications. In another study, Hamaguchi $et\ al.$ synthesized (n-$C_6H_{13}NH_3)_2(MA)Pb_2I_7$ and (n-$C_6H_{13}NH_3)_2(FA)Pb_2I_7$ (FA = formamidine) thin films using the standard spin-coating method, and by increasing the spin speed, they found the proportion of perpendicularly orientated layers increases.[137] Venkatesan $et\ al.$ demonstrated that the orientation of $(BA)_2(MA)_{n-1}Pb_nI_{3n+1}$ layers could be gradually changed from parallel to perpendicular to the substrate with increasing dimensionality n.[141]

(ii) Crystal size and grain morphology have been demonstrated to be controllable via the solvent evaporation temperature. The hot casting technique involves spin-coating on a heated substrate, leading to perovskites of near-single-crystalline quality. The high quality of perovskites provides

32

channels with fast charge transport, allowing charge carriers to travel across electrodes without inhibition of insulating spacer layers.[115] Sun *et al.* found that longer annealing times facilitate the decomposition of small-*n* quantum wells and the formation of large-*n* quantum wells in mixed dimensionality perovskite films.[131] Raghavan *et al.* showed that high-quality millimeter-sized crystals of $(BA)_2(MA)_{n-1}Pb_nI_{3n+1}$ can be synthesized via a slow evaporation at a constant temperature. These crystals demonstrated high crystallinity, phase purity, and spectral uniformity.[142] Yangui *et al.* also used a similar approach to synthesize crystals of $(CHA)_2CdBr_4$.[143]

(iii) The chemical composition of 2D perovskites can be varied by changing the precursor components during the perovskite crystal synthesis. For example, Cortecchia *et al.* fabricated 2D Cu-based, Cl/Br mixed halide perovskites by stoichiometrically mixing, then crystallizing perovskite powders in ethanol.[138] Zhou *et al.* introduced a ternary organic cation to form $(BA)_2(MA,FA)_3Pb_4I_{13}$ perovskite films by replacing MAI with FAI in the stoichiometric reaction between PbO, MAI, and BAI. At 20% FA, crystal grains increased from several hundred nanometers to several micrometers. At 40% and higher amounts of FA, grain size increased in the films, but the density decreased and more pinholes and cracks formed. At 60% FA, microparticles appeared on the surface and the film roughness increased three fold compared to 40% FA. These results suggest that the quasi-2D orientation does not change below 40%, but beyond 40%, the MA cannot be stoichiometrically replaced by FA.[144]

(iv) The dimensionality can be controlled with the addition of an MAI immersion step. The quasi-2D perovskite, $(IC_2H_4NH_3)_2(MA)_{n-1}Pb_nI_{3n+1}$, was synthesized by by Koh *et al.* using the standard spin-coating method for the pure 2D components followed by immersion in a CH_3NH_3I dipping solution for 1-5 minutes to increase the dimensionality.[140] Alongside dimensionality control, 2D/3D junctions can also be formed by a slow drying process of a 2D/3D perovskite precursor mixture. Grancini *et al.* used this method to synthesize 2D/3D $(HOOC(CH_2)_4NH_3)_2PbI_4/(MA)PbI_3$ perovskite junctions by mixing the precursors at different molar ratios (0-3-5-10-20-50%). The mixed solution was deposited on and infiltrated in an inert ZrO_2 scaffold followed by a slow drying-process, allowing the components to be reorganized before solidification. Similarly, Lin *et al.*

created 2D/3D stacking structures by spin-coating solutions of BA and BAI on top of 3D perovskite layers; and the BA treatment led to a smoother 2D layer with better coverage compared to BAI treatment.[126] Vassilakopoulou *et al.* were able to create blends of quasi-2D and 3D perovskites by dissolving weight ratios of perovskites solutions in DMF then spin-coating.[145]

Other Methods

Besides the mainstream spin-coating approach, other techniques have also been used to synthesize 2D perovskites flakes, crystals, and thin films. These techniques include i) mechanical exfoliation, ii) solution-based processing, iii) sonication-assisted synthesis approach, and iv) self-doping based on the template of 2D hybrid perovskites, as discussed below.

(i) The mechanical exfoliation method was used to produce the thin films of 2D perovskites. For instance, Yang's research team tried to produce the thin sheets of $(BA)_2PbBr_4$ from its large single crystal using mechanical exfoliation via tape and solvent exfoliation methods.[146] Unfortunately, most of the products were very thick flakes from the mechanical exfoliation and were randomly shaped particles from solvent exfoliation. They also found that the monolayer-thick particles were very small (less than $1\mu m$), suggesting that the hybrid perovskite layers are mechanically brittle. The mechanical exfoliation method was also used to produce ultrathin crystalline layers of $(BA)_2PbI_4$,[147] $(PEA)_2PbI_4$,[148] and $(BA)_2(MA)_{n-1}Pb_nI_{3n+1}$.[149]

(ii) The solution-based processing method was used to prepare the thin 2D hybrid perovskite $(BA)_2PbBr_4$ and its derivatives.[146] In this work, uniform square-shaped 2D crystals were prepared on a flat Si/SiO_2 substrate using a ternary co-solvent that contains dimethylformamide (DMF), chlorobenzene (CB), and acetonitrile. The three solvents have their own roles: the polar organic DMF was used to dissolve the $PbBr_4$-based inorganic materials; the CB reduces the solubility of $(BA)_2PbBr_4$ in DMF and promotes crystallization; and acetonitrile facilitates the formation of the ultrathin 2D hybrid perovskite sheets. Interestingly, unlike other 2D materials, a structural relaxation (lattice constant expansion) was found in the 2D hybrid perovskite sheets, which might be responsible for some emergent features such as the shift of band edge emission.[146] Chen *et al.* also

made ultrathin $(BA)_2PbBr_4$ perovskites using the same technique based on the dimethylformamide-chlorobenzene-acetonitrile ternary solvent.[150] It is noted that, by using chlorobenzene (CB) as co-solvent, thin films of $(MA)_2Pb(SCN)_2I_2$[151] and $(TFA)_2(MA)_{n-1}Pb_nBr_{3n+1}$ (TFA = 3,4,5-trifluoroanline)[152] were also synthesized via spin-coating approach.

(iii) The sonication-assisted synthesis approach was used by Xiong *et al.* to prepare crystals of $(H_2BDA)PbI_4$ (H_2BDA=1,4-butanediammonium dication) and $(HNPEIM)PbI_3$ (HNPEIM=N-phenyl-ethanimidamidine cation).[153] They mixed the precursors, sonicated the mixture for 5 minutes, and then froze the mixture in liquid nitrogen for 10 minutes. The mixture was then vacuum sealed, then placed in an oven at 120 °C for 7 days.[153] Neogi *et al.* also used a sonication technique to dissolve the precursors of $(CyBMA)PbBr_4$ prior to perovskite crystallization.[154] Yu *et al.* prepared 2D hybrid perovskite $(OA)_2PbBr_4$ via an ultrasonic-assisted postsynthetic refinement technique, and these refined 2D nanosheets can subsequently be used as a template for the formation of low-dimensional $CsPbBr_3$ with inherited size and morphology and enhanced optoelectronic properties.[155]

(iv) A generalized self-doping directed synthesis approach was also employed to prepare ultrathin 2D homologous $(BA)_2(MA)_{n-1}Pb_nBr_{3n+1}$ perovskites, in which the 2D $(BA)_2PbBr_4$ perovskites were used as templates and $(MA)^+$ as dopant.[125]

3.2.2 Characterization

Structures

The 2DHP have a general form $(R)_2(MA)_{n-1}MX_{3n+1}$, where R is an aliphatic or aromatic alkylammonium cation, MA is methylammonium ($CH_3NH_3^+$), M is a metal cation with a 2+ oxidation state (such as Pb, Sn, and Ge), X is a halide anion (such as I, Br, and Cl), and *n* is the dimensionality. One special case is so-called Dion–Jacobson perovskites, where the large organic cation has a 2+ charge leading to only one organic cation between each inorganic layer, following the formula $(R')(MA)_{n-1}MX_{3n+1}$.[2] Figure 3.3 illustrates the structural differences between the
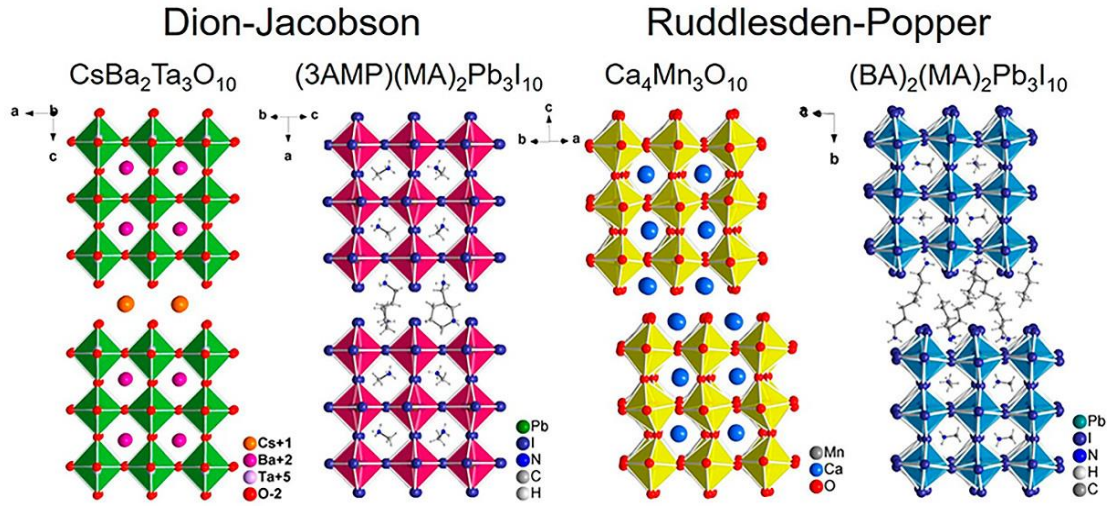
Figure 3.3: A structural comparison between Dion–Jacobson and Ruddlesden–Popper perovskite phases. Reproduced and adapted with permission from [2].

Dion–Jacobson perovskites and the well-known Ruddlesden–Popper perovskites. Unlike the case of Ruddlesden–Popper perovskites, in the Dion–Jacobson perovskites, inorganic octahedra corners of inorganic layers lay exactly above adjacent inorganic layers.[2]

The dimensionality, *n*, dictates the number of inorganic sheets placed between each organic layer. A schematic illustration of the 2D framework for *n* = 2-4 is given in Figure 3.4. At *n* = 1, the formula can be simplified as $(R)_2MX_4$, a strictly 2D perovskite material such as $(BA)_2PbBr_4$.[146] At *n* > 1, the formula includes the MA cation, describing a quasi-2D perovskite material where the MA cation is intercalated between inorganic layers such as in $(PEA)_2(MA)_2Pb_3Br_{10}$.[120] At *n* = ∞, the formula can be rewritten as $(MA)MX_3$, a 3D perovskite such as $(MA)PbI_3$.[84] A schematic progression of the dimensionality is shown in Figure 3.5.

The 2DHP is composed of distorted inorganic layers of $[MX_6]^{4-}$ interdigitated with organic cation bilayers. Several guidelines have been proposed for selecting suitable organic cations for incorporation within the layered perovskite frameworks:[90] i) the organic molecule must contain one or more terminal cation groups such as NH_3^+ that can interact with and hydrogen bond to the inorganic anion; ii) the organic cation must have appropriate width and shape (or the cross
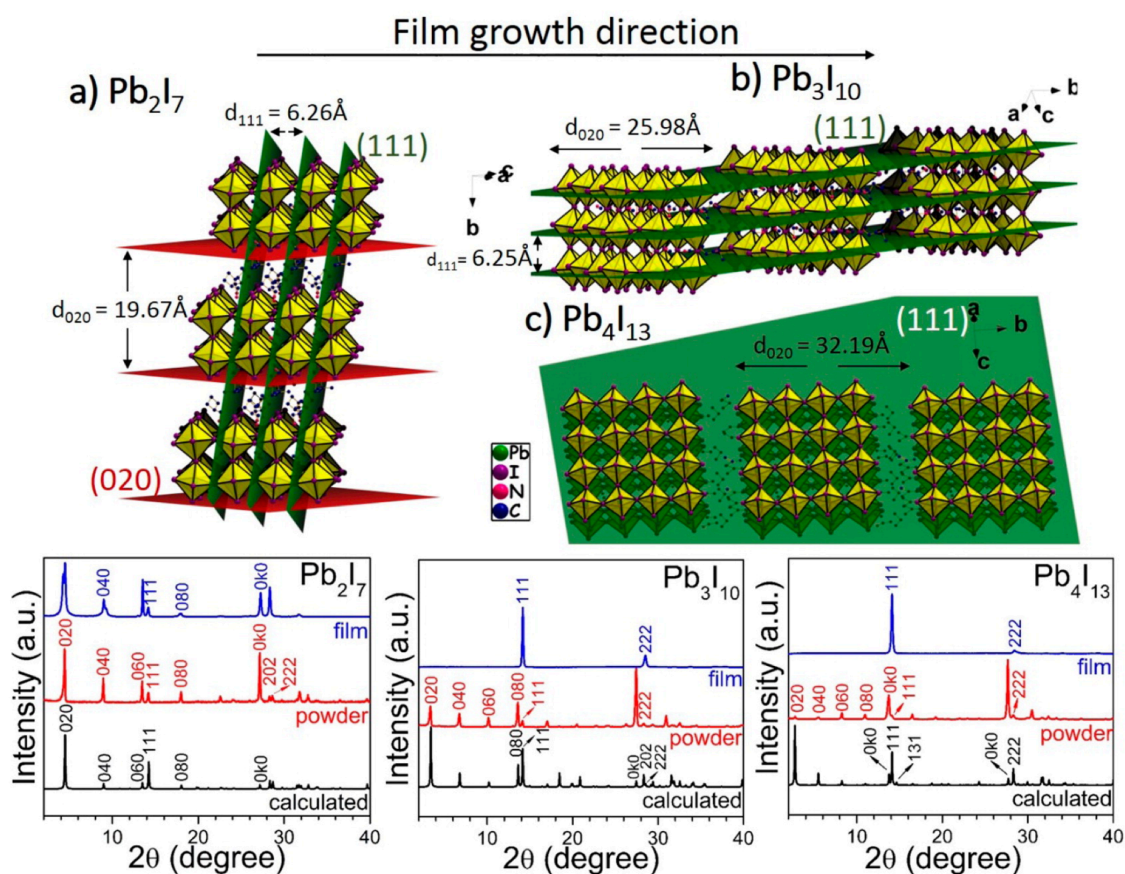
Figure 3.4: Structural characterization of thin films and bulk materials of hybrid perovskites from X-ray diffraction. (a) $(BA)_2(MA)Pb_2I_7$ ($n = 2$, $m = 4$), (b) $(BA)_2(MA)_2Pb_3I_{10}$ ($n = 3$, $m = 4$), and (c) $(BA)_2(MA)_3Pb_4I_{13}$ ($n = 4$, $m = 4$). The corresponding X-ray diffraction patterns of three systems are shown in (a'), (b'), and (c'), respectively. Reproduced and adapted with permission from [4].
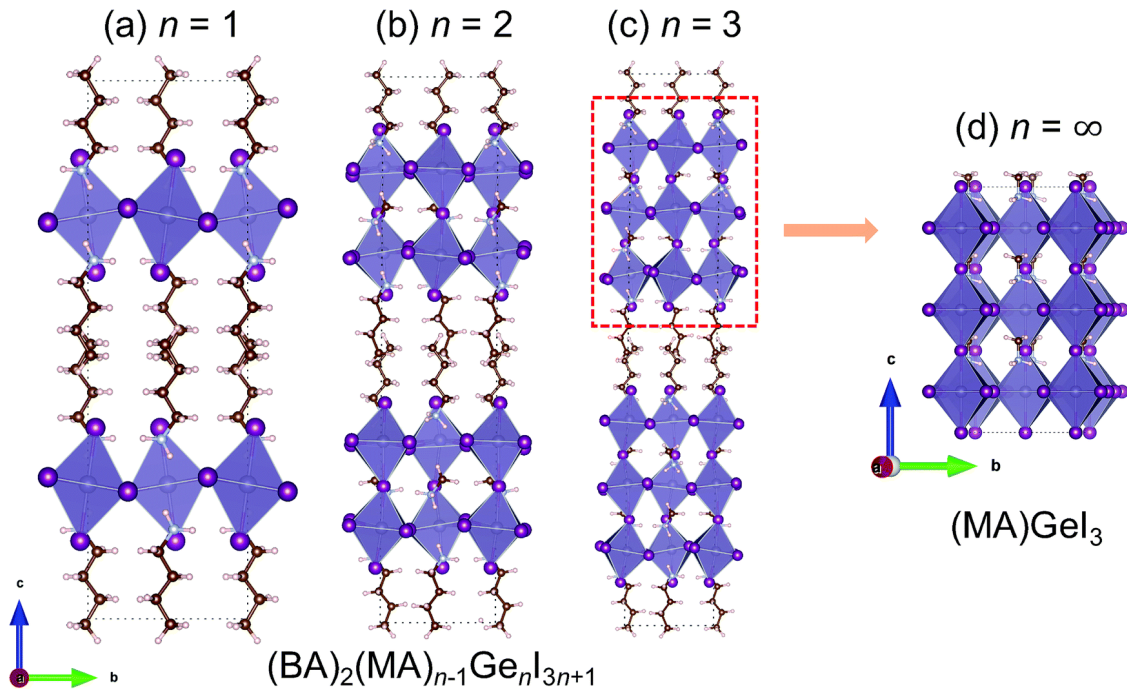
Figure 3.5: Scheme of the different structural dimensions of the hybrid perovskite $(BA)_2(MA)_{n-1}Ge_nBr_{3n+1}$. The butylammonium (BA) are barrier cations. Reproduced and adapted from [156].

sectional area of the molecule) that can fit into an area defined by the terminal halides from four adjacent corner-sharing octahedra; iii) the length of organic molecule can take a wide range of values compared to the width. The organic cation and the inorganic octahedra can each template the structural conformation of the other and consequently change materials properties. To provide an informative review of organic cations and inorganic frameworks, herein, we summarized the commonly used organic cations including their full names, abbreviations, and chemical formulas in Table 3.1, and the experimentally synthesized hybrid perovskites including their crystal lattice type, space groups, and lattice parameters in Table 3.2.

Table 3.1: List of organic cations in 2DHP: abbreviations, full name, and chemical formulas.

Abbreviation	Full Name	Chemical Formula	Ref
3AMP	3-(Aminomethyl)-piperidinium	$C_6H_9NH_2CH_2NH_3^{2+}$	[2]

38

Table 3.1: (continued):

Abbreviation	Full Name	Chemical Formula	Ref
4FA	4-Fluoroanillinium	$C_6H_4FNH_3^+$	[157]
4CA	4-Chloroanilinium	$C_6H_4ClNH_3^+$	[157]
4AMP	4-(Aminomethyl)-piperidinium	$C_6H_9NH_2CH_2NH_3^{2+}$	[2]
AVA	Aminovaleric Acid	$HOOC(CH_2)_4NH_3^+$	[139]
BZA	Benzylammonium	$C_6H_5CH_2NH_3^+$	[158]
BA	Butylammonium	$C_4H_9NH_3^+$	[123]
C6	Hexylammonium	$C_6H_{13}NH_3^+$	[159]
C12	Dodecylammonium	$C_{12}H_{25}NH_3^+$	[159]
C16	Hexadecylammonium	$C_{16}H_{33}NH_3^+$	[159]
C18	Octadecylammonium	$C_{18}H_{37}NH_3^+$	[159]
CA	4-Chloroanilinium	$ClC_6H_4NH_3^+$	[159]
CB	Cyclobutylammonium	$C_4H_7NH_3$	[159]
CHA	Cyclohexylammonium	$C_6H_{11}NH_3^+$	[143]
CHE	2-Cyclo-hexenylethanamine	$C_6H_9(CH_2)_2NH_3^+$	[121]
CM	Cyclohexyl-methanammmonium	$C_6H_{11}CH_2NH_3^+$	[121]
CP	Cyclopropylammonium	$C_3H_5NH_3^+$	[159]
CPe	Cyclopentylammonium	$C_5H_9NH_3^+$	[159]
CyBMA	Cis-1,3-bis-(methylaminohydrobromide)-cyclohexane	$C_6H_{10}(NH_3Br)_2^{2+}$	[154]
DD	Dodecylammonium	$NH_3(CH_2)_{12}NH_3^{2+}$	[159]
DMA	Dimethylammonium	$(CH_3)_2NH_2^+$	[160]
DMABA	4-Dimethylamino-butylammonium	$(CH_3)_2NH(CH_2)_4NH_3^+$	[161]
DMAPA	3-(Dimethylamino)-1-propylammonium	$(CH_3)_2NHCH_2NH_3^+$	[161]
DMEN	2-(Dimethylamino)-ethylammonium	$(CH_3)_2NH(CH_2)_2NH_3^+$	[161]
EDBE	2,2'-(Ethylenedioxy)-bis(ethylammonium)	$NH_3(CH_2)_2O(CH_2)_2O(CH_2)NH_3^{2+}$	[162]
FA	Formamidinium	$CH(NH_2)_2^+$	[3]
G	Guanidinium	$C(NH_2)_3^+$	[3]
HA	Histammonium	$C_3N_2H_4(CH_2)_2NH_2^{2+}$	[127]
H$_2$BDA	1,4-Butanediammonium	$NH_3(CH_2)_4NH_3^+$	[153]
HNPEIM	N-phenyl-ethanimidamidine	$C_6H_5NHCNH_2CH_3^+$	[153]
IMI	2,2'-Biimidazolium	$C_3H_2(NH)_2C_3H_2(NH)_2^{2+}$	[163]
MA	Methylammonium	$CH_3NH_3^+$	[66]
MFM	5-Methyl-2-furanmethanamine	$CH_3OC_4H_2CH_2NH_3^+$	[121]

Table 3.1: (continued):

Abbreviation	Full Name	Chemical Formula	Ref
N-MEDA	N^1-Methylethane-1,2-diammonium	$CH_3NH_2(CH_2)_2NH_3^+$	[164]
N-MPDA	N^1-Methylpropane-1,3-diammonium	$CH_3NH_2(CH_2)_3NH_3^+$	[164]
Ni(opd)$_2$(acn)$_2$	Di(o-phenylenediamine)-di(acetonitrile)nickelate	$Ni(C_6H_4(NH_2)_2)_2(CH_3CN)_2^{2+}$	[165]
OL	Oleylammonium	$CH_3(CH_2)_7(CH)_2(CH_2)_8NH_3^+$	[145]
PEA	Phenylethylammonium	$C_6H_5C_2H_4NH_3^+$	[120]
PMA	Phenylmethanammonium	$C_6H_5CH_2NH_3^+$	[166]
PYR	4,4'-Bipyridinium	$C_5H_4NHC_5H_4NH^{2+}$	[163]
TFA	3,4,5-Trifluoroaniline	$C_6H_2F_3NH_3^+$	[152]
TFM	(Tetrahydrofuran-2-yl)methanamine	$OC_4H_7CH_2NH_3$	[121]
TPM	2-Thiophenemethylamine	$SC_4H_4CH_2NH_3^+$	[121]

Table 3.2: List of 2DHP: chemical formula, crystal system, space group, and lattice parameters at the measured temperature.

compound	T (K)	crystal system	space group	a (Å)	b (Å)	c (Å)	β	Ref
(BA)$_2$GeI$_4$	293	Orthorhombic	Pcmn	8.722	8.272	28.014	90°	[62]
(BA)$_2$SnI$_4$	293	Orthorhombic	Pbca	8.837	8.619	27.562	90°	[62]
(BA)$_2$PbI$_4$	293	Orthorhombic	Pbca	8.863	8.682	27.57	90°	[62]
(BA)$_2$(MA)-Pb$_2$I$_7$	293	Orthorhombic	Cc2m	8.947	8.859	39.347	90°	[123]
(BA)$_2$(MA)$_2$-Pb$_3$I$_{10}$	293	Orthorhombic	C2cb	8.928	8.878	51.959	90°	[123]
(BA)$_2$(MA)$_3$-Pb$_4$I$_{13}$	293	Orthorhombic	Cc2m	8.927	8.882	64.383	90°	[123]
(BA)$_2$(MA)$_4$-Pb$_5$I$_{16}$	293	Orthorhombic	C2cb	8.905	77.013	8.931	90°	[167]
(MA)$_2$CuCl$_4$		Monoclinic	P121/a1	7.257	7.35	9.69	111.2°	[138]
(MA)$_2$CuCl$_2$Br$_2$		Orthorhombic	Acam	7.319	7.328	19.134	90°	[138]
(MA)$_2$CuClBr$_3$		Orthorhombic	Acam	7.397	7.369	19.322	90°	[138]
(MA)$_2$CuCl$_{0.5}$Br$_{3.5}$		Orthorhombic	Acam	7.428	7.469	19.308	90°	[138]
(MA)$_2$CuBr$_4$				7.801	7.624	19.129		[138]
(MA)$_2$FeCl$_4$	273	Tetragonal	I4/mmm	7.203	7.203	19.126	90°	[168]
(MA)$_2$FeCl$_4$	383	Orthorhombic	Pccn	5.12	5.12	19.272	90°	[168]
(MA)Pb-(SCN)$_2$I$_2$	298	Orthorhombic	Pnm2$_1$	18.58	6.267	6.466	90°	[169]

Table 3.2: (continued):

compound	T (K)	crystal system	space group	a (Å)	b (Å)	c (Å)	β	Ref
$(PEA)_2(MA)_2$-Pb_3I_10	100	Triclinic	P1	8.728	8.733	28.803	95.878°	[120]
$(PEA)_2CuCl_4$	100	Orthorhombic	Pbca	7.21	7.266	38.238	90°	[170]
$(PEA)_2CuCl_4$	370	Orthorhombic	Cmca	39.021	7.343	7.394	90°	[170]
$(4FA)_2CuCl_4$	150	Monoclinic	$P2_1/c$	15.511	7.379	7.093	99.004°	[157]
$(CA)_2CuCl_4$	150	Orthorhombic	Pccn	7.374	32.069	7.161	90°	[157]
$(CA)_2CuCl_4$	298	Monoclinic	$P2_1/c$	16.434	7.391	7.263	101.576°	[157]
$(CHA)_2CdBr_4$	300	Orthorhombic	$Cmc2_1$	26.641	8.673	8.605	90°	[143]
$(BZA)_2PbCl_4$	293	Orthorhombic	$Cmc2_1$	33.64	7.817	7.737	90°	[158]
$(BZA)_2PbBr_4$	293	Orthorhombic	Cmca	33.394	8.153	8.131	90°	[158]
$(BZA)_2PbI_4$	293	Orthorhombic	Pbca	9.156	8.689	28.776	90°	[127]
$(BZA)_2SnI_4$	293	Orthorhombic	Pbca	9.094	8.661	28.764	90°	[127]
$(HA)PbI_4$	293	Monoclinic	$P2_1/n$	8.916	20.034	8.993	91.875°	[127]
$(HA)SnI_4$	293	Monoclinic	$P2_1/n$	8.741	20.045	8.984	91.571°	[127]
$(CyBMA)$-$PbBr_4$	298	Orthorhombic	Pnma	8.5661	24.457	7.979	90°	[154]
$(3AMP)PbI_4$	293	Monoclinic	$P2_1/c$	8.673	18.4268	20.452	99.306°	[2]
$(3AMP)(MA)_3$-Pb_4I_{13}	293	Cubic	Ia	8.863	8.869	58.842	90°	[2]
$(4AMP)PbI_4$	293	Monoclinic	Pc	10.5	12.543	12.529	89.984°	[2]
$(4AMP)(MA)_3$-Pb_4I_{13}	293	Cubic	Ia	8.859	8.857	58.915	90°	[2]
α-(DMEN)-$PbBr_4$	293	Orthorhombic	Pbca	18.901	11.782	23.680	90°	[161]
β-(DMEN)-$PbBr_4$	293	Monoclinic	$P2_1/c$	17.625	11.982	18.724	90.44°	[161]
(DMAPA)-$PbBr_4$	293	Monoclinic	$P2_1/c$	10.717	11.735	12.127	111.53°	[161]
(DMABA)-$PbBr_4$	293	Orthorhombic	Aba2	41.685	23.962	12	90°	[161]
(N-MEDA)-$PbBr_4$	100	Orthorhombic	$P2_12_12_1$	6.076	8.393	23.743	90°	[164]
(N-MPDA)-$PbBr_4$	100	Monoclinic	$P2_1/c$	8.316	8.316	20.118	101.695°	[164]
(EDBE)-$PbCl_4$	100	Monoclinic	C2	7.732	7.542	13.293	102.481°	[162]
(EDBE)-$PbBr_4$	100	Monoclinic	$P2_1/c$	6.092	28.78	8.886	91.852°	[162]
(EDBE)-PbI_4	100	Monoclinic	Aba2	6.494	29.461	9.267	91.777°	[162]
$[Ni(opd)_2$-$(acn)_2]_n$-$[Pb_4I_{10}]_n$	293	Monoclinic	$P2_1/c$	13.981	7.888	19.746	95.303°	[165]

Table 3.2: (continued):

compound	T (K)	crystal system	space group	a (Å)	b (Å)	c (Å)	β	Ref
$(FA,G)PbI_4$	298	Monoclinic	C2/m	26.948	12.819	14.408	109.941°	[3]

The geometrical structures of 2D hybrid perovskite materials are often characterized by X-ray diffraction (XRD) and atomic force microscopy (AFM).[138, 4, 146, 148] Below, we review recent experimental characterization on four types of 2D and quasi-2D perovskites: (i) perovskites containing long chain organic molecules and MA, (ii) perovskites containing aromatic ring molecules, (iii) perovskites containing MA only, and (iv) perovskites containing dimethylammonium (DMA).

(i) The first class is perovskites containing long chain organic molecules with a chemical formula $R_2(MA)_{n-1}Pb_nI_{3n+1}$, in which the large organic cation, R, refers to an aliphatic alkylammonium chain ($C_mH_{2m+1}NH_3$) with a length of m, such as the butylammonium cation ($C_4H_9NH_3$, BA), where $m = 4$. For the compounds $(BA)_2MI_4$ ($n = 1$, m = 4, M = Ge, Sn, and Pb), their in-plane lattice constants increased as a function of the ionic radius of M cations, *i.e.*, from Ge to Sn and Pb. Mitzi found that $(BA)_2GeI_4$ crystallizes in a space group of *Pcmn* with a higher degree of inorganic octahedra distortion due to stereochemical activity of the Ge(II) nonbonding electrons.[62] Mitzi also found that $(BA)_2SnI_4$ and $(BA)_2PbI_4$ crystallize in a space group of *Pbca* with weaker lone-pair stereoactivity. The lattice constants of $(BA)_2PbBr_4$ ($n = 1$, $m = 4$) 2D perovskite sheets were found to be a = 8.41 Å, b = 8.6 Å, and c = 14.2 Å.[146] Stoumpos *et al.* also found $(BA)_2(MA)_{n-1}Pb_nI_{3n+1}$ (n = 1-4, m = 4) crystallizes in an orthorhombic lattice for all n values, but in centrosymmetric for n = 1 and noncentrosymmetric for n = 2-4. Compounds with an odd n value adopt a higher symmetry configuration compared to even n value compounds.[123] In this work, they found that the large BA cation requires a 7.8 Å gap between the perovskite layers and its CH_3CH_2-tail has a large degree of distortion than the $NH_3CH_2CH_2$-head. In addition, they showed that the ratio between the spacer cation and the smaller organic cation during crystal synthesis can be adjusted to control the perovskite dimensionality. Billing and Lemmerer found that the two reversible phase transitions in

$(C_mH_{2m+1}NH_3)_2PbI_4$ ($n = 1$, $m = 12$, 14, 16, and 18) occurring above room temperature correspond to changes in the packing of the inorganic layers, the positioning of the ammonium group relative to the inorganic layers, and the conformation of the hydrocarbon chains.[171]

(ii) The second class of 2D hybrid perovskites contain aromatic or cyclic ring cations such as $(PEA)_2(MA)_{n-1}Pb_nBr_{3n+1}$ (PEA = phenylethylammonium). The lattice parameters in triclinic $(PEA)_2(MA)_2Pb_3Br_{10}$ ($n = 3$) were measured to be: a = 8.728 Å, b = 8.733 Å, c = 28.803 Å, α = 92.734°, β = 95.878°, and γ = 90.254°.[120] $(PEA)_2(MA)_{n-1}Pb_nBr_{3n+1}$ (n = 1-4) perovskite crystals have distorted octahedral inorganic structures with a size of 6.3 Å.[117] Thin films of this material were found to be a collection of their grains with a variety of n values instead of a single-phase.[119] $(PEA)_2CuCl_4$ crystallizes in an orthorhombic phase with a space group number *Pbca* with lattice constants of a = 7.21 Å, b = 7.266 Å, and c = 38.238 Å below 340 K, and with a space group number *Cmca* and lattice constants a = 39.021 Å, b = 7.343 Å, and c = 7.394 Å above 340 K.[170] The Cd-based 2D perovskite, $(CA)_2CdBr_4$ (CA = cyclohexylammonium) crystallizes in a noncentrosymmetric and polar orthorhombic space group $Cmc2_1$ and has lattice constants a = 26.64 Å, b = 8.673 Å, and c = 8.605 Å.[143] The crystals of $(4FA)_2CuCl_4$ (4FA = 4-fluoroanilinium) were found to crystallize in a moniclinic phase at 150K.[157] This work also showed that $(CA)_2CuCl_4$ (CA = 4-chloroanilinium) crystallizes at 298K in the monoclinic phase, but undergoes a reversible phase transition at 150K from monoclinic to orthorhombic. $(BZA)_2PbCl_4$ (BZA = benzylammonium) crystallizes in an orthorhombic phase with a space group $Cmc2_1$ and has lattice constants a = 33.64 Å, b = 7.817 Å, and c = 7.734 Å at 293 K.[158] Similarly, $(BZA)_2PbBr_4$ also crystallizes in an orthorhombic phase with a space group *Cmca* and lattice constants a = 33.394 Å, b = 8.153 Å, c = 8.131 Å.[158] $(HA)PbI_4$ and $(HA)SnI_4$ (HA = histammonium) crystallizes in a monoclinic phase with a space group $P2_1/n$, in which the divalent HA cation was observed to bring layers close together, giving a certain 3D character to the structure; $(BZA)_2PbI_4$ and $(BZA)_2SnI_4$ crystallizes in an orthorhombic phase with a space group *Pbca*.[127] In these two materials, the inorganic octahedra are relatively undistorted, leading to slightly lower bandgaps,[127] unlike most 2D perovskites. $(CyBMA)PbBr_4$ crystallizes in an orthorhombic phase with a space group *Pnma*

and lattice constants a = 8.513 Å, b = 24.424 Å, and c = 7.937 Å. The Pb–Br–Pb bond angles were found to strongly deviate from planar geometry due to hydrogen bonding between the organic ligands and the $PbBr_4$ octahedra.[154] The structures of several divalent aromatic ring contained perovskites have also been studied from DFT calculations, in which distorted structures were found in a staggered arrangement and the interlayer distances were found small due to the strongly charged cations between organic layers.[163]

(iii) The third class of 2D hybrid perovskites contain MA organic cation only, in which the separation between inorganic layers is not caused by the large organic cation. For example, Cortecchia *et al.* showed that in $(MA)_2CuX_4$ (n = 1, X = Cl and Br), the lead-free 2D perovskite, interlayer separation is achieved by steric hinderance caused by the smaller ionic radii of the Cu^{2+} atoms.[138] It was found that $(MA)_2CuCl_{0.5}Br_{3.5}$ crystallizes in orthorhombic with a space group *Acam* and lattice constants of a = 7.428 Å, b = 7.468 Å, and c = 19.308 Å, in which a layered structure with a spacing of 10 Åwas confirmed from XRD. $(MA)_2CuCl_4$ crystallizes in a monoclinic phase with a space group *P121/a1* and lattice constants of a = 7.257 Å, b = 7.35 Å, and c = 9.969 Å. The Cu^{2+} inorganic layers in $(MA)_2CuCl_4$ and $(MA)_2CuBr_4$ were found to have a highly distorted octahedral coordination due to Jahn-Teller distortion. The lattice parameters of these intermediate mixed-halide Cu-based perovskites are summarized in Table 3.2.

$(MA)_2FeCl_4$ crystallizes in a high-symmetry tetragonal phase above 335 K with a space group *I4/mmm* and in the low-symmetry orthorhombic phase below 335 K with a space group *Pccn*. The lattice constants were measured to be a = 7.203 Å, b = 7.203 Å, and c = 19.126 Å below 335 K and a = 5.12 Å, b = 5.12 Å, and c = 19.272 Å above 335 K.[168] In $(MA)Pb(SCN)_2I_2$, S-bonded SCN^- ligands in the *trans* position on the Pb octahedra separate the inorganic layers in a manner similar to that of a large organic cation in other 2D perovskites. $(MA)Pb(SCN)_2I_2$ crystallizes in an orthorhombic lattice with a space group *Pnm2*$_1$ and lattice constants of a = 18.58 Å, b = 6.267 Å, and c = 6.466 Å.[169] The first-principles calculations by Tang *et al.* suggest that the SCN^- ion shortens the Pb–S bond lengths and increases the octahedra distortion, hydrogen bonds, and stability relative to undoped systems. The SCN^- ion was also found to strengthen Young's modulus

and enhances the piezoelectric properties.[172]
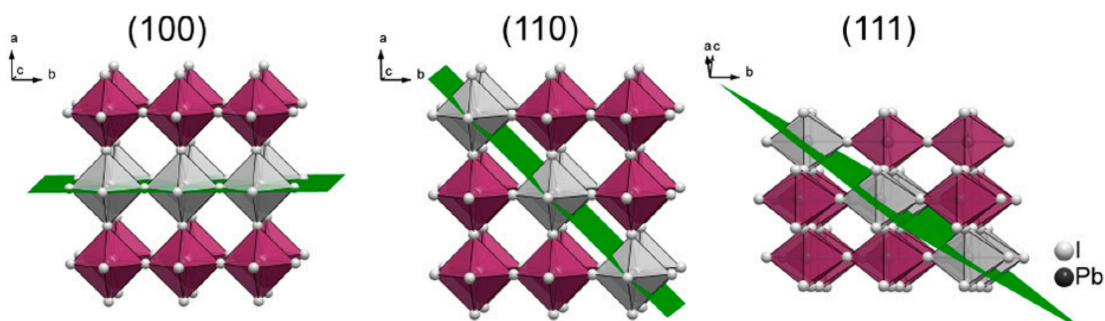
Figure 3.6: Schematic illustration of three types of derivation of 2DHP by cutting their parental cubic perovskite lattice along the planes a) (100), b) (110), and c) (111). Reproduced and adapted with permission from [3].

(iv) The fourth class of 2D perovskites are dimethyl- or diammonium-based materials. In this class of hybrid perovskite materials, the inorganic monolayers are oriented in the (110) direction of their parental cubic perovskite lattice, which is different from the case of the former three classes of perovskite materials. Figure 3.6 shows the three types of derivation of 2DHP by cutting their parental cubic perovskite lattice along the crystallographic planes (100), (110), and (111). For instance, in the 2D perovskite α-(DMEN)PbBr$_4$ (DMEN = 2-(dimethylamino)ethylamine), its organic layers are composed of highly corrugated (110)-oriented layers,[161] see Figure 3.7a. Figure 3.7b and 3.7c show the structures of monoclinic (DMAPA)PbBr$_4$ (DMAPA = 3-(dimethylamino)-1-propylamine) and orthorhombic (DMABA)PbBr$_4$ (DMABA = 4-dimethylaminobutylamine) which belong to conventional (100)-oriented family, respectively.[161] In addition to dimethyl cations, diammonium cations can also form similar structures, such as the (001) monoclinic perovskite (N-MPDA)PbBr$_4$ (1, N-MPDA = N^1-methylpropane-1,3-diammonium), the corrugated (110) orthorhombic perovskite (N-MEDA)PbBr$_4$ (2, N-MEDA = N^1-methylethane-1,2-diammonium), and monoclinic (EDBE)PbX$_4$ (EDBE = 2,2'-(ethylenedioxy)bis(ethylammonium), X = Cl, Br, I).[164, 162, 173] The corrugated perovskite (FA,G)PbI$_4$ (FA = formamidinium, G = guanidinium) contains two large diammonium cations that alternate between interlayer spaces. (FA,G)PbI$_4$ crystallizes in a monoclinic phase with a space group *C2/m* and lattice constants a = 26.948 Å, b = 12.819 Å, and c = 14.408 Å.[3] In

(DMA)$_7$Pb$_4$X$_{15}$ (X = Cl$^-$ or Br$^-$, DMA = dimethylammonium), linear Pb$_4$X$_{15}^{7-}$ chains are linked together to form somewhat corrugated layers. The DMA cations were also found to be ordered under 100 K, but disordered at higher temperatures around 275 K.[160]
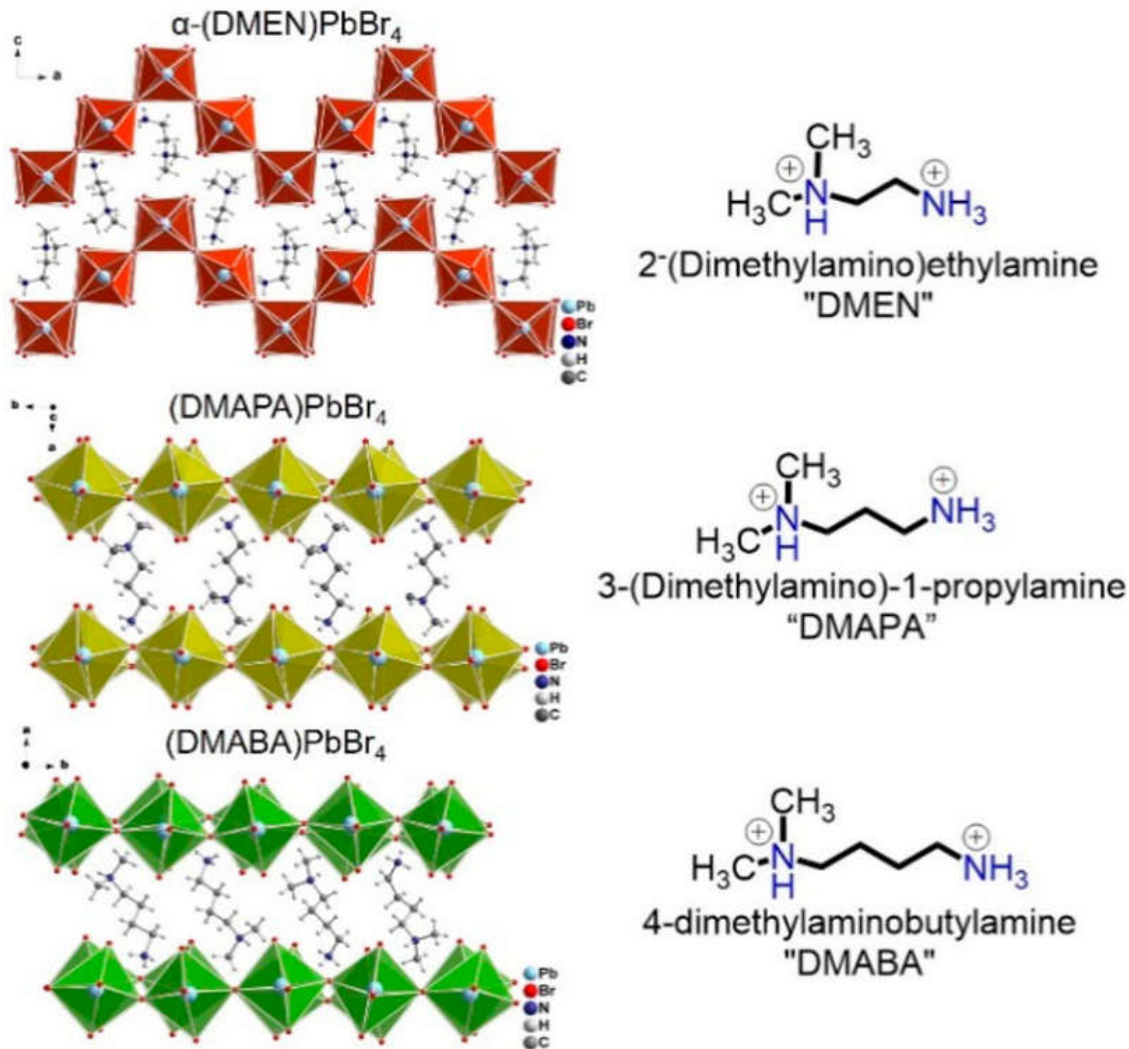
Figure 3.7: (Left) Crystal structures of 2DHPs a) α-(DMEN)PbBr$_4$ with (001) orientation, b) (DMAPA)PbBr$_4$ with (100) orientation, and c) (DMABA)PbBr$_4$ with (100) orientation and (Right) their respective organic barrier cations. Herein the orientation refers to that the 2D perovskites derives from their parental 3D structures by cutting the inorganic lattice along the crystallographic planes. Reproduced and adapted with permission from Ref [161].

In addition, it is worth mentioning that 2D perovskites can also be considered as multiple-quantum-well structures where the wells are the semiconducting inorganic layers and the barriers are the insulating organic layers.[174, 135] The quantum well thickness of the 2D hybrid perovskties

Table 3.3: Band gaps (eV) of several 2DHPs as a function of dimensionality, n.

Compound	n						Ref
	1	2	3	4	5	∞	
Experimental							
$(BA)_2(MA)_{n-1}Pb_nI_{3n+1}$	2.39	2.14	2.02				[134]
$(BA)_2(MA)_{n-1}Pb_nI_{3n+1}$	2.24	1.99	1.85	1.6		1.52	[4]
$(BA)_2(MA)_{n-1}Pb_nI_{3n+1}$	2.42	2.15	2.04	1.92	1.85		[5]
$(BA)_2(MA)_{n-1}Pb_nI_{3n+1}$	2.43	2.17	2.03	1.91		1.5	[123]
$(BA)_2(MA)_{n-1}Sn_nI_{3n+1}$	1.83	1.64	1.5	1.42	1.37	1.2	[114]
$(PEA)_2(MA)_{n-1}Pb_nI_{3n+1}$	2.4	2.2	2				[175]
$(PEA)_2(MA)_{n-1}Pb_nI_{3n+1}$	2.41	2.21	2.18	1.88	1.82	1.68	[119]
$(PEA)_2(MA)_2Pb_3I_{10}$			2.1				[120]
$(3AMP)(MA)_{n-1}Pb_nI_{3n+1}$	2.23	2.02	1.92	1.87	1.8	1.59	[2]
$(4AMP)(MA)_{n-1}Pb_nI_{3n+1}$	2.38	2.17	1.99	1.89	1.8	1.59	[2]
DFT							
$(PEA)_2(MA)_{n-1}Pb_II_{3n+1}$ (no SOC)	2.31	2.17	1.95				[175]
$(PEA)_2(MA)_{n-1}Pb_II_{3n+1}$ (with SOC)	1.43	1.2	0.91				[175]
$(BA)_2(MA)_{n-1}Pb_nI_{3n+1}$	1.99		1.78	0.96			[123]
$(BA)_2(MA)_{n-1}Pb_nI_{3n+1}$	2.0		1.7			1.2	[115]

was found to range between a few to tens of nanometers.[146] For instance, the thickness of $(BA)_2(MA)_{n-1}Pb_nI_{3n+1}$ (n = 1-4, m = 4) ranges from 0.641 nm to 3.139 nm for n = 1 to 4 respectively.[5] The thickness of $(C_6H_9C_2H_4NH_3)_2PbI_4$ (n = 1-3, m = 8) layers was determined to be 2.5, 4.1, and 5.7 nm for n = 1, 2, and 3 respectively.[148] Yaffe *et al.* measured the n = 1 nanosheet thickness to be 2.4 nm.[147]

Band Gaps

Band gaps of 2DHPs are one of the most important materials parameters in their optoelectronic applications and have been extensively studied via light absorption and photoluminescence spectra. Herein we summarized the bandgaps of 2DHPs in Tables 3.3, 3.4, and 3.5, and discussed

Table 3.4: Experimental band gaps (eV) of several 2DHPs as a function of composition, x.

Compound	0	0.125	0.25	0.5	0.75	0.875	1	Ref
$(PEA)_2Ge_{x-1}Sn_xI_4$	2.13	2.09	2.04	1.95				[176]
$(PEA)_2SnI_{4x}Br_{4(x-1)}$	2.66		2.47	2.28	2.13		1.97	[177]
$(HA)_2Pb_{x-1}Sn_xI_4$	2.05		1.78	1.76	1.74		1.67	[127]
$(BZA)_2Pb_{x-1}Sn_xI_4$	2.18		1.86	1.84	1.82		1.89	[127]
$(MA)_2CuCl_{4(x-1)}Br_{4x}$	2.48			2.12	1.9	1.8		[138]

their trends as the function of structural dimensionality and compositions.
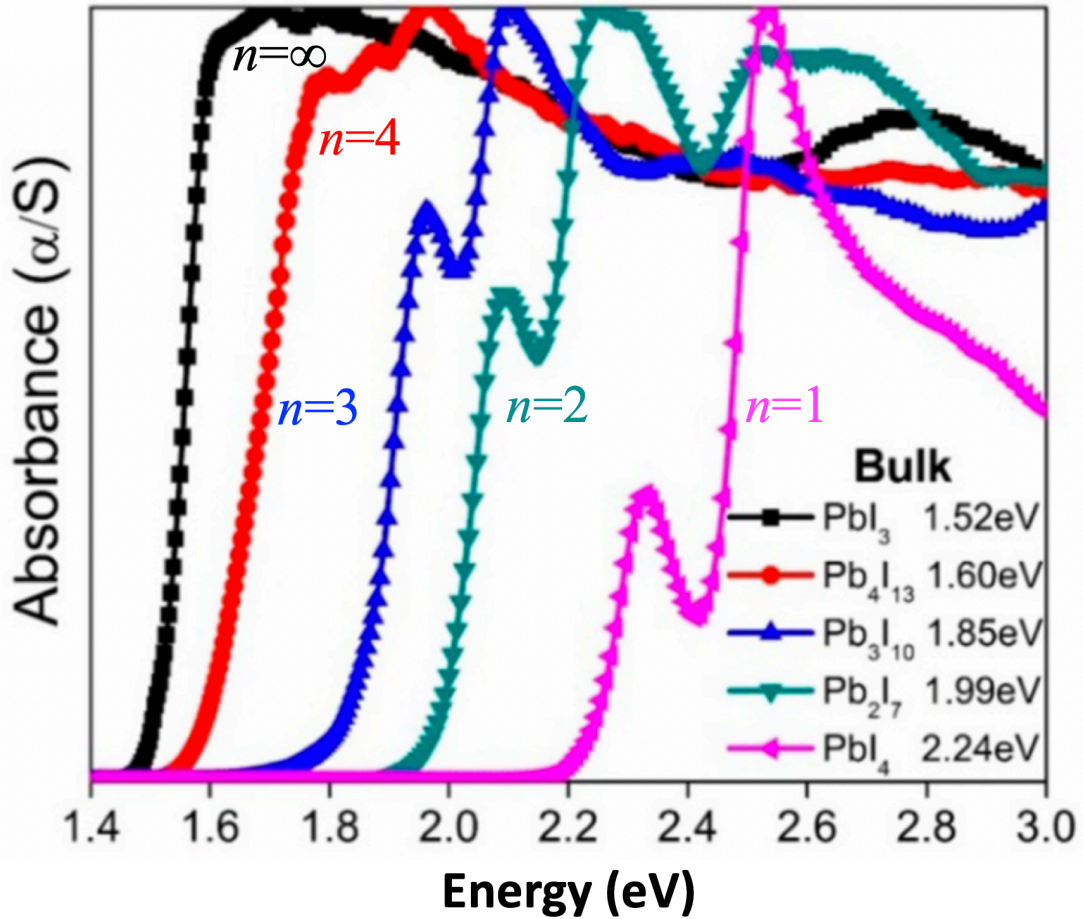
Figure 3.8: Optical band gaps of $(BA)_2(MA)_{n-1}Pb_nI_{3n+1}$ with $n=1, 2, 3, 4,$ and ∞ determined from light absorption spectra. Reproduced and adapted with permission from Ref [4].

Table 3.5: Band gaps (eV) of several single layer 2DHPs.

Compound	Bandgap (eV)	Ref	Compound	Bandgap (eV)	Ref
Experimental					
$(C12)PbI_4$	2.75	[159]	$(CHE)PbCl_4$	3.64	[121]
$(C16)PbI_4$	2.98	[159]	$(BZA)_2PbCl_4$	3.65	[158]
$(C18)PbI_4$	2.98	[159]	$(PEA)_2PbCl_4$	3.64	[133, 121]
$(CA)PbI_4$	3.25	[159]	$(PEA)_2PbBr_4$	3.07	[133]
$(CHE)PbI_4$	2.87	[159]	$(PEA)_2PbI_4$	2.4	[133, 129]
$(CP)PbI_4$	3.04	[159]	$(PEA)_2PbI_4$	2.49	[159]
$(CB)PbI_4$	2.88	[159]	$(MA)_2Pb(SCN)_2I_2$	2.04	[130]
$(CPe)PbI_4$	2.86	[159]	$(MA)_2Pb(SCN)_2I_2$	1.77	[169]
$(DD)PbI_4$	2.99	[159]	$[Ni(opd)_2(acn)_2]_n-[Pb_4I_{10}]_n$	2.67	[165]
$(CM)PbCl_4$	3.7	[121]	$(H_2BDA)PbI_4$	2.64	[153]
$(PMA)PbCl_4$	3.7	[121]	$(HNPEIM)PbI_3$	2.73	[153]
$(TPM)PbCl_4$	3.7	[121]	$\alpha-(DMEN)PbBr_4$	3	[161]
$(TFM)PbCl_4$	3.77	[121]	$(DMAPA)PbBr_4$	2.88	[161]
$(MFM)PbCl_4$	3.79	[121]	$(DMABA)PbBr_4$	2.85	[161]
DFT					
$(MA)_2Pb(SCN)_2I_2$	1.53	[116]	$(BZA)_2PbCl_4$	3.34	[158]
$(MA)_2Pb(SCN)_2I_2$	2.06	[130]	$(BZA)_2PbI_4$	1.42	[127]
$(H_2BDA)PbI_4$	2.01	[153]	$(BZA)_2SnI_4$	1.33	[127]
$(HNPEIM)PbI_3$	2.91	[153]	$(HA)PbI_4$	1.34	[127]
$(EDBE)PbI_4$	2.83	[178]	$(HA)SnI_4$	1.14	[127]

The first trend is that the band gaps of 2DHPs generally increase as the dimensionality decreases.[4, 123, 114, 5] The band gaps of $(BA)_2(MA)_{n-1}Pb_nI_{3n+1}$ were found to range from 1.52 ($n = \infty$) to 2.24 eV ($n = 1$) from photoluminescence spectra, as shown in Fig. 3.8.[4] Similarly, Stoumpos *et al.* found these values to range from 1.5 ($n = \infty$) to 2.43 eV ($n = 1$) with intermediate values of 1.91 ($n = 4$), 2.03 ($n = 3$), and 2.17 eV ($n = 2$); [123] Blancon *et al.* measured the band gaps to range from 1.85 ($n = 5$) to 2.42 eV ($n = 1$)[5] and Wu *et al.* found the band gaps to range from 2.02 ($n = 3$) to 2.39 eV ($n = 1$).[134] Lanty *et al.* measured the band gaps of $(PEA)_2(MA)_{n-1}PbI_{3n+1}$ to range from 2.41 ($n = 1$) to 1.68 eV ($n = \infty$) using time- and wavelength-dependent transient absorption.[119] The band gaps of $(3AMP)(MA)_{n-1}Pb_nI_{3n+1}$ and $(4AMP)(MA)_{n-1}Pb_nI_{3n+1}$ varied from 2.23 ($n=1$) to 1.87 eV ($n=4$) and 2.38 ($n=1$) to 1.89 eV ($n=4$) respectively.[2] Sn-based Ruddlesden–Popper perovskites demonstrate a similar trend, with band gaps ranging from 1.20 eV ($n = \infty$) to 1.83 eV ($n = 1$).[114]

In addition to dimensionality variation, the band gap can also be tuned through selection of the halide anions, large organic cations, and metal cations. A more electronegative halide anion generally leads to a larger band gap. For example, band gaps of Cu-based perovskites, $(MA)_2CuX_4$ ($n = 1$, X = Cl and Br), were found decrease from 2.48 eV to 1.8 eV, as increasing Br concentration in the molecular formula.[138] For $(PEA)_2PbX_{3n+1}$ (X = Cl, Br, I), their band gaps were measured to be 3.64 eV, 3.07 eV, and 2.4 eV for X = Cl, Br, and I, respectively.[133] A similar trend was measured in $(PEA)_2SnI_xBr_{4-1}$ with band gaps decreasing from 2.66 eV to 1.97 eV with increasing I concentrations.[177] Zhang *et al.* tuned the band gap of PbCl$_4$-based perovskites from 3.76 eV to 3.64 eV by using different large organic cations such as cyclohexyl-methanamine (CM, 3.7 eV), phenylmethanamine (PM, 3.7 eV), 2-thiophenemethylamine (TPM, 3.7 eV), (tetrahydrofuran-2-yl)methanamine (TFM, 3.77 eV), 5-methyl-2-furanmethanamine (MFM, 3.79 eV), 2-cyclohexenylethanamine (CHE, 3.64 eV), and PEA (3.64 eV).[121] It is noted that while the band gap can be varied via the choice of large organic cation, the band gaps do not involve the organic orbitals directly, as shown in a prior computational study.[179] Instead, Fraccarollo *et al.* show that the large organic cation indirectly influences the bandgap via the geometric distortions of

50

the inorganic octahedra using DFT calculations.[180] For $(HA)Pb_{1-x}Sn_xI_4$ and $(BZA)_2Pb_{1-x}Sn_xI_4$, the band gaps in both materials were found to decrease with increasing Sn concentration, with the lowest band gap of 1.74 eV at an intermediate value of x = 0.75 for $(BZA)_2Pb_{1-x}Sn_xI_4$.[127] The authors also found that the band gap decreases as the M–I–M angle approached 180°, ranging from 2.18 eV for $(BZA)_2PbI_4$ to 2.05 eV for $(HA)PbI_4$. Similarly, the bandgap of $(PEA)_2Ge_{1-x}Sn_xI_4$ (x = 0-0.5) decreases almost linearly from 2.13 to 1.95 eV with increasing Sn concentrations.[176]

There are two types of band gaps: direct and indirect. A direct band gap semiconductor has the conduction band minimum (CBM) and the valence band maximum (VBM) located at the same *k*-vector in the Brillouin zone, allowing for photon absorption and emission without a change in the momentum. Conversely, an indirect band gap requires a change in the momentum for photon emission and absorption.[181] Semiconductors with direct band gaps are often preferred because they have higher photon absorption rate.[182, 109] Many 2D perovskite materials are characterized to have a direct band gap.[147, 153, 130] For example, $(BA)_2PbI_4$ has a direct band gap of 2.4 eV;[147] $[Ni(opd)_2(acn)_2]_n$-$[Pb_4I_{10}]_n$ (opd = o-phenylenediamine; acn = acetonitrile) has a direct band gap of 2.67 eV (0.4 eV greater than PbI_2), meaning that the organic cation leads to a blue shift of the band gap with respect to PbI_2;[165] the single layered perovskites $(H_2BDA)PbI_4$ and $(HNPEIM)PbI_3$ have a direct band gap of 2.64 and 2.73 eV, respectively.[153]

The bandgap type can be predicted from Tauc plots.[183] As shown in Figure 3.9b and 3.9c, Xiao *et al.* found the $(MA)_2Pb(SCN)_2I_2$ material to be an indirect bandgap semiconductor with an indirect bandgap of 2.04 eV and direct bandgap of 2.11 eV.[130] However, the authors state that Tauc plots are often mistakenly used to predict the transition mode.[184] He states that both direct and indirect Tauc plots have linear parts which give different bandgap values, meaning it is difficult to determine the mode of transition by comparison of the plots given that the transition mode is an assumption to begin with. Because of this, it is hard to say if $(MA)_2Pb(SCN)_2I_2$ is truly an indirect semiconductor, and in this case, first-principles electronic structure calculations are effective tools to reveal the nature of the band gap type.

Besides the light harvestation for solar cells, the light absorption of 2D perovskites has also
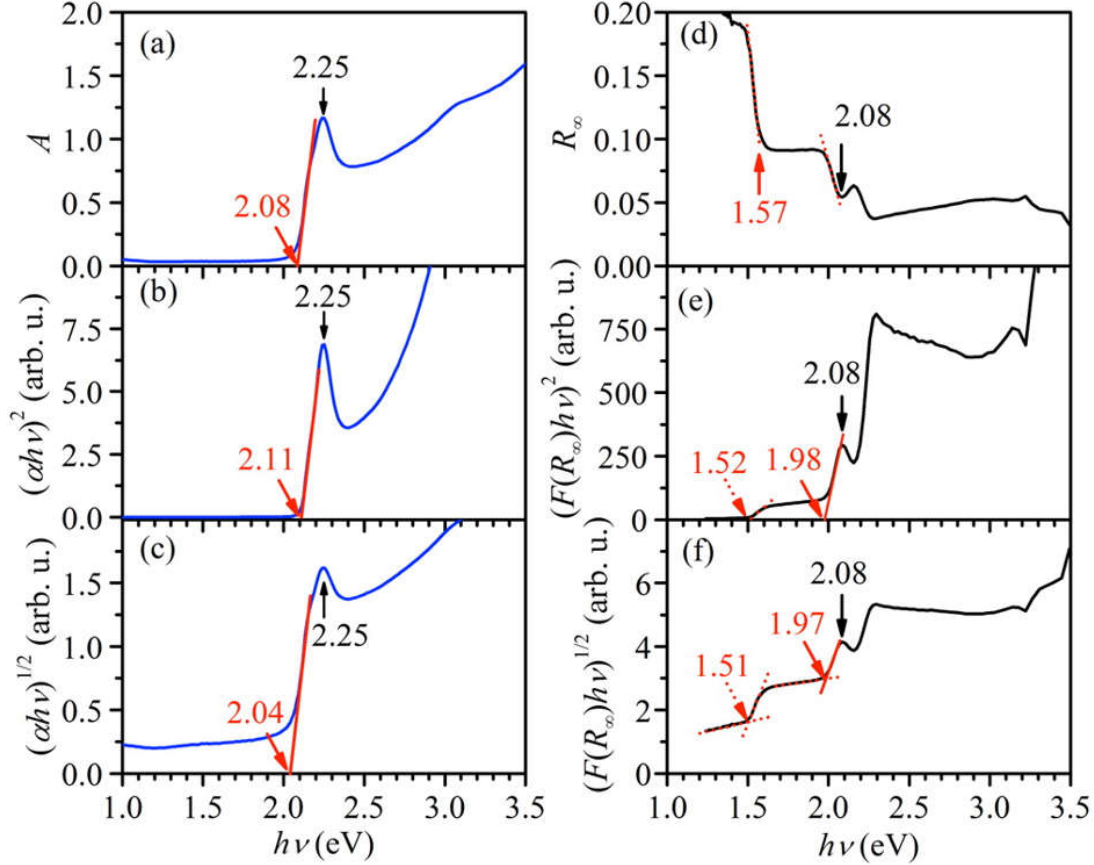
Figure 3.9: (a) Absorbance (A) spectrum of a $(MA)_2Pb(SCN)_2I_2$ thin film. (b,c) Tauc plots of the A spectrum corresponding to (b) a direct and (c) an indirect optical bandgap of $(MA)_2Pb(SCN)_2I_2$. (d) Diffuse reflectance (R_∞) spectrum of $(MA)_2Pb(SCN)_2I_2$ powders. (e,f) Tauc plots of the R_∞ spectrum corresponding to (e) a direct and (f) an indirect optical bandgap of $(MA)_2Pb(SCN)_2I_2$. Reproduced and adapted with permission from Ref [130]. Copyright 2016 American Chemical Society.

been studied for other optoelectronic applications including laser cooling, spin-state manipulation, and photodetection.[122, 185, 125] Liu *et al.* found a large two-photon absorption coefficient of 211.5 cm MW^{-1} in $(PEA)_2PbI_4$, about one order of magnitude larger than 3D perovskites, and a saturation effect excited by a 800 nm femtosecond laser.[1] These properties are attributed to quantum and dielectric confinement effects. Ha *et al.* achieved a maximum laser cooling of 58.7 K from room temperature for $(PEA)_2PbI_4$, demonstrating the potential use of 2D perovskites in optical cooling devices.[122] This optical refrigeration effect was considered to be caused by a strong photoluminescence upconversion and near unity external quantum efficiency. In addition, the optical

properties of 2D perovskites were also found to meet the criteria necessary for the ultrafast optical implementations in quantum information applications.[186] For example, Giovanni *et al.* observed a spin-selective optical Stark effect in $(PEA)_2PbBr_4$, $(PEA)_2PbI_4$, and $(PEA)_2PbI_4$, demonstrating a light-based method for room-temperature spin manipulation.[185] 2D perovskites also have potential applications in the photodetector devices. For example, Tan *et al.* built a photodetector using $(BA)_2PbBr_4$ with graphene as an electric contact, which shows a high responsivity ($\sim$2100 A/W), low dark current ($\sim 10^{-10}$ A), and high on/off current ratio ($\sim 10^3$).[187] Chen *et al.* produced a photodetector using the quasi 2D perovskite, $(BA)_2(MA)_{n-1}Pb_nBr_{3n+1}$, and their device achieved a photoresponsivity of 190 mA/W and an on/off current ratio of 2.3×10^3.[125]

Light Emission

Light emission of semiconductors have several major applications such as large-area display, indicator lights, and energy-efficient light sources.[188] c The organic-inorganic hybrid perovskites offer a high color purity regardless of crystal size because of their multiple quantum well structure.[189, 190, 135] In particular, the 2D hybrid perovskites are promising alternative light-emitters to organic light-emitting diodes and inorganic quantum dot LEDs because of their bandgap tunability and solution processability,[4, 123, 114, 5, 117, 130, 132, 133, 121, 134] Herein we summarized several typical features of light emission in the 2D hybrid perovskites, including the broadband emission, quantum efficiency, exciton binding energy, and exciton states.

Broadband Emission. 2D hybrid perovskites have been found to emit radiation across the entire visible spectrum upon UV excitation, generating white light.[164, 162, 132, 117, 123] This phenomenon is known as broadband emission, and it demonstrates the potential use of layered hybrid perovskites as single-source white-light phosphors. The first instance of broadband emission in layered hybrid perovskites was observed in 2014 by Dohner *et al.* in $(EDBE)PbX_4$ (X = Cl, Br, I), (N-MPDA)$PbBr_4$, and (N-MEDA)$PbBr_4$.[162, 164] Neogi *et al.* observed a broadband white-light emission in (CyBMA)$PbBr_4$, and attributed this broad emission to self-trapped states that are favored by deformations of the inorganic layers.[154] Mao *et al.* examined three 2D lead

bromide perovskite materials that exhibit similar features: α-(DMEN)PbBr$_4$, (DMAPA)PbBr$_4$, and (DMABA)PbBr$_4$. They found a direct relationship between increasing distortion of the inorganic layers and the broadening of photoluminescence (PL) emission, with the most distorted structure having the broadest emission and longest lifetime.[161] Cortecchia *et al.* compared the highly distorted perovskite (EDBE)PbI$_4$ with the less distorted perovskite (BA)$_2$PbI$_4$ and found that only (EDBE)PbI$_4$ can form lead vacancies that lead to the formation of I$_3^-$ and thus a broadened PL, implying an important role of structural distortion in the broadband emission.[178]

Yangui *et al.* studied the relationship between inorganic layer distortion and broadband PL emission in (C$_6$H$_{11}$NH$_3$)$_2$PbBr$_4$ and (CHA)$_2$CdBr$_4$, and explained this phenomenon from the perspective of self-trapped states.[191, 143] To be specific, they found two emission peaks at 2.94 eV corresponding to excitons confined in the inorganic layers and another peak at 2.53 eV corresponding to emission of the organic moiety in (CHA)$_2$CdBr$_4$.[143] They also found that the photoluminescence spectra varies with temperature due to phase transitions and changes in interlayer spacing, with a peak emission at 90K, and the white-light emission coexists with an excitonic edge emission at lower temperatures.[191, 143] A very recent study by García-Fernandez *et al.* also showed that (DMA)$_7$Pb$_4$X$_{15}$ exhibits a broadband PL related to the structural distortions of the inorganic octahedra.[160]

Hu *et al.* explored the mechanism of broadband white-light emission in the (110) 2D hybrid perovskite (*N*-MEDA)[PbBr$_4$] (*N*-MEDA = N^1-methylethane-1,2-diammonium) using a suite of ultrafst spectroscopic probes and concluded that the broadband emission is associated with a distribution of local minima in the excited-state potential energy surface with additional contributions from material defects and correlated self-trapped sites from ultrafast spectroscopic measurement.[173] In (EDBE)PbX$_4$ (X = Cl, Br, and I), Dohner *et al.* found an emission that originates from the bulk material rather than surface defect sites, along with contributions from strong electron-phonon coupling in a deformable lattice, with an inhomogeneous broadening due to a distribution of intrinsic trap states.[162]

In addition, it was also found that the photoluminescence (PL) of 2D hybrid perovskites

could be tuned. For instance, Dou *et al.* found a PL emission peak at 411 nm in the bulk crystal of $(BA)_2PbBr_4$ and a slightly shifted peak at 406 nm in its 2D sheets, and verified that this shift is caused by lattice expansions in the 2D sheets from DFT calculations.[146] Mitzi *et al.* observed a blue-shift in the emission peak from $(BA)_2GeI_4$ (690 nm) to $(BA)_2SnI_4$ (625 nm) to $(BA)_2PbI_4$ (525 nm) with a progressive increase in the peak sharpness.[62] Booker *et al.* found a red-shifted and broadband emission below 200 K in addition to excitonic photoluminescence in $(C6)_2PbI_4$ and $(C12)_2PbI_4$.[128] White light emission was also observed in the (001) perovskite (N-MPDA)$PbBr_4$ and the corrugated (110) perovskite (N-MEDA)$PbBr_4$, and the emission chromaticity can be tuned through halide substitution.[164]

Some other factors that influence the photoluminescence of 2D hybrid perovskites were also explored. For instance, Jia *et al.* observed an increased radiative electron-hole recombination in the 2D $(TFA)_2(MA)_{n-1}Pb_nBr_{3n+1}$ as compared to that in the 3D perovskites, and attributed this phenomenon to the reduced grain size in the quasi-2D perovskite films.[152] Sun *et al.* found that the optimal dimensionality constitution in films of quasi-2D perovskite lies between a low and high *n* value, where the film has the highest PLQE while still maintaining uniform film morphology.[131] Vassilakopoulou *et al.* found that mixtures of quasi-2D $(PEA)_2Pb_nBr_{3n+1}$ and 1D $(MA)CdBr_3$ entrapped in a polystyrene film led to green luminescence.[192] Daub and Hillebrecht measured a strong emission peak at 702 nm and a shoulder at 760 nm in $(MA)_2Pb(SCN)_2I_2$ via fluorescence spectroscopy.[169]

Quantum Efficiency. The performance metrics for light-emitting semiconductors include the internal and external quantum efficiency—the number of photons emitted by the active region and in total respectively per unit time divided by the number of injected electrons per unit time and the photoluminescence quantum efficiencies.[188] The 2D hybrid perovskites are found to have a much higher quantum efficiency than 3D hybrid perovskites. For example, Yuan *et al.* reported high photoluminescence quantum yield (PLQY) values of 10.1% and 10.6% in $(PEA)_2(CH_3NH_3)_{n-1}Pb_nI_{3n+1}$ for $n = 3$ and $n = 4$, respectively, in contrast to a nearly negligible PLQY for 3D perovskites at the same excitation intensity. Using this material, they designed an LED device with a record

external quantum efficiency of 8.8% with a corresponding radiance of 80 W sr^{-1}m^{-2} operating at near-infrared wavelengths.[119]

Byun *et al.* fabricated a LED device using 2D (PEA)$_2$PbBr$_4$ that shows a higher current efficiency and luminance thatn (MA)PbBr$_3$.[117] In this work, it was found that a mixture of the 2D (PEA)$_2$PbBr$_4$ with (MA)PbBr$_3$ forms a quasi-2D perovskite film that yields the highest luminescence (2935 cd m^{-2}) and current efficiency (4.9 cd A^{-1}) with a PLQE of 34%. The authors attributed this to fully homogeneous perovskite films that have a small particle size, low trap density, and decent charge transport properties. The optimal *n* values for PLQY in (PEA)$_2$(CH$_3$NH$_3$)$_{n-1}$Pb$_n$I$_{3n+1}$ are summarized in Figure 3.10. Lanzetta *et al.* found that the PLQE of thin films of (PEA)$_2$SnI$_x$Br$_{4-x}$ ranges from 0.24% to 0.04% and decreases as Br concentration increases, but remained consistently higher than that of the 3D perovskite, MASnI$_3$ (PLQE = 0.01%).[177] Using this material, they constructed an electroluminescent device reaching a luminance of 0.15 cd/m^2 at 4.7 mA/cm^2 and an efficacy of 0.029 cd/A at 3.6 V. The (TFA)$_2$(MA)$_{n-1}$Pb$_n$Br$_{3n}$-based LED prepared by Jia *et al.* demonstrated a maximum luminance of 1.2×10^3 cd/m^2 and current efficiency up to 0.4 cd/A, a twenty fold enhancement compared to that of (MA)PbBr$_3$.[152] The PLQE of (CyBMA)PbBr$_4$ was measured to be 1.5%,[154] and the room-temperature PLQE of (FA,G)PbI$_4$ was found to be 3.5%.[3]

Exciton Binding Energy. The excitonic properties including the exciton formation, diffusion, binding energy, and thermal quenching significantly influence the light-emission efficiency of an electroluminescent material.[193, 194, 195, 196, 197, 198] A high exciton binding energy strengthens the stability of excitons against thermal dissociation, allowing for potential applications in room temperature LED devices. Compared to their 3D counterparts, 2D perovskites have a much higher exciton binding energy due to sharp dielectric contrast between the high and low dielectric constants of the inorganic and organic layers respectively.[132, 135] The high frequency limit (ε_∞)—the dielectric constant—decreases with decreasing layer thickness, but its value is not affected by the size of aliphatic chains.[199] For example, Yangui *et al.* measured a large exciton binding energy (356 meV) in (C$_6$H$_{11}$NH$_3$)$_2$PbI$_4$ that was attributed to a large dielectric contrast
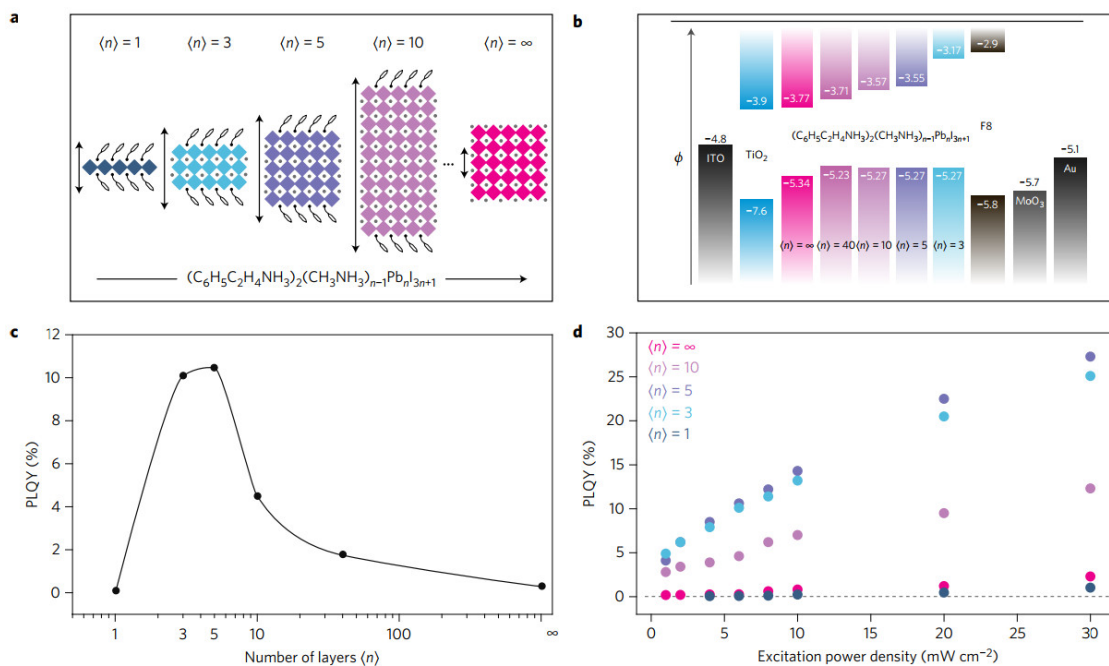
Figure 3.10: Unit cell structure, electronic bandstructure and photoluminescent properties of quasi-2D perovskites. a, Unit cell structure of $(C_8H_9NH_3)_2(MA)_{n-1}Pb_nI_{3n+1}$ perovskites with different <n> values, showing the evolution of dimensionality from 2D ($n = 1$) to 3D ($n = \infty$). b, Electronic band structure of perovskites with different <n> values, combined with the band structure of ITO, TiO2, F8, MoO3 and the Au electrode. ϕ, electric potential. c, Summary of the PLQY for perovskite films with different <n> values at a low excitation intensity (6 mW cm-2). d, Evolution of the PLQY with increasing excitation intensity for perovskites with different <n> values. The data show a steeper and earlier (lower threshold intensity) rise in PLQY for quasi-2D perovskites compared with 2D and 3D perovskites. Reproduced and adapted with permission from Ref [119]. Copyright 2016 Springer Nature.

between organic and inorganic layers.[132] An exciton binding energy of 377 meV and a sharp excitonic peak at 3.24 eV were reported in $(CHA)_2CdBr_4$.[143] Yaffe *et al.* found that the excitons of $(BA)_2PbI_4$ are stable at room temperature with binding energies of 490 meV and have properties that are strongly influenced by changes in the dielectric environment.[147] Blancon *et al.* reported exciton binding energies of $(BA)_2(MA)_{n-1}Pb_nI_{3n+1}$ to range from an average value of 220 meV, 270 meV, and to 380 meV for $n > 2$, $n = 2$ and $n = 1$, respectively, approximately one order of magnitude greater than in 3D lead halide perovskites.[5] Neogi *et. al.* measured an exciton binding energy of 340 meV in $(CyBMA)PbBr_4$.[154]

The exciton binding energy of 2D hybrid perovskite was also studied from first-principles calculations. For instance, in our previous work on $(BA)_2(MA)_{n-1}Ge_nI_{3n+1}$, the calculated exciton binding energies range from 202 meV to 190 meV to 150 meV to 34 meV for $n = 1, 2, 3$, and ∞ respectively.[156] Tsai *et al.* calculated the exciton binding energy of $(BA)_2(MA)_{n-1}Pb_nI_{3n+1}$ at $n = 3$ and 4 to be close to that of $(MA)PbI_3$, in agreement with the absence of excitonic signatures in their optical absorption spectra.[115] This suggests that the excitons in $(BA)_2(MA)_{n-1}Pb_nI_{3n+1}$ at $n = 3$ and 4 are nearly ionized at room-temperature, leading to free carrier-dominated charge transport.

Triplet Exciton State. A triplet exciton state is a bound electron-hole pair that has a total spin angular momentumof 1, allowing for three values of spin component m_s (-1, 0, 1). These triplet exciton states constitute 75% of excitons that are generated during charge injection. Harnessing these triplet excitons in phosphorescent molecules enables the potential of attaining 100% internal quantum efficiency in phosphor-doped LEDs.[200, 201] The triplet exciton properties of 2D perovskites demonstrate their potential for thin film triplet photosensitizers applications including desulfurization of light oil,[202] photooxidation,[203] and photodynamic therapy.[204] Younts *et al.* demonstrated efficient generation of triplet exciton states in the solid 2D $(MA)_2Pb(SCN)_2I_2$ perovskite films, with a corresponding photoluminescence quantum efficiency of 11.7% at 160K and extremely long diffusion lengths of about 152 nm for the generated triplet excitions, which allows an efficient transport across the entire thin film. Accordingly, due to the efficient exciton

formation and extraction at the material/molecule interface, a viable thin film triplet photosensitizer can be realized in $(MA)_2Pb(SCN)_2I_2$.[151]

Other Excitonic Properties. Other properties including excitonic band gap, excitonic peak, and exciton-phonon scattering are discussed here. Smith *et al.* found the exciton band of $(PEA)_2(MA)_2Pb_3I_{10}$ ($n = 3$) to be 2.06 eV,[120] close to the ideal value (1.9 eV) for the higher band-gap absorber in a dual-absorber tandem device,[205] which can surpass the Shockley-Queisser limit.[206] Abdel-Baki *et al.* measured an excitonic peak at 2.397 eV in $(PEA)_2(MA)PbI_4$, and found that the exciton relaxation fits to a bi-exponential decay with a free exciton lifetime of $\tilde{1}00$ ps and intraband lifetime of < 140 fs.[135] They suggested that the excitons are delocalized in $(PEA)_2(MA)PbI_4$ ($n = 1$), pointing to the importance of the organic layer in the optoelectronic properties of 2D perovskites.[135]

Cao *et al.* reported that for Sn-based Ruddlesden–Popper perovskites, $(BA)_2(MA)_{n-1}Sn_nI_{3n+1}$, excitonic peaks only exist in the single-layered compounds, suggesting that they have lower exciton binding energy due to higher dielectric constants.[114] Vassilakopoulou *et al.* found that the excitonic band gap depends on the organic molecule in addition to the crystal structure.[145] Guo *et al.* investigated the intrinsic exciton relaxation pathways in the layered $(C_4H_9NH_3)_2(CH_3NH_3)_{n-1}Pb_nI_{3n+1}$ (n = 1, 2, and 3) structures from time-resolved and temperature-dependent PL studies.[149] They found that the PL decay rate increases with temperature, implying an exciton–phonon scattering. Their results also indicate that scattering *via* deformation potential by acoustic and homopolar phonons is the main scattering mechanism, which suggests that exciton decay is protected from scattering by charge defects and polar optical phonons, leading to the efficient screening of Coulomb potential as in 3D perovskites..

Tunning Excitonic Properties. The excitonic properties can be tuned by modifying the number of inorganic layers, halide composition, or large organic cation selection. DFT calculations by sapori *et al.* verify that the high frequency limit (ε_∞), or the dieletric constant, decreases with decreasing layer thickness, but that its value is not affected by the size of aliphatic chains.[199] Niu *et al.* found that exciton amplitude scales linearly with increasing number of layers due to disorder

causing inhomogeneous broadening of the exciton resonance.[148] Lanty *et al.* found that exciton absorption peaks show a parabolic relationship with increasing composition of larger halide anions, reaching a maximum at a 50-50 composition of large and small anions.[133]
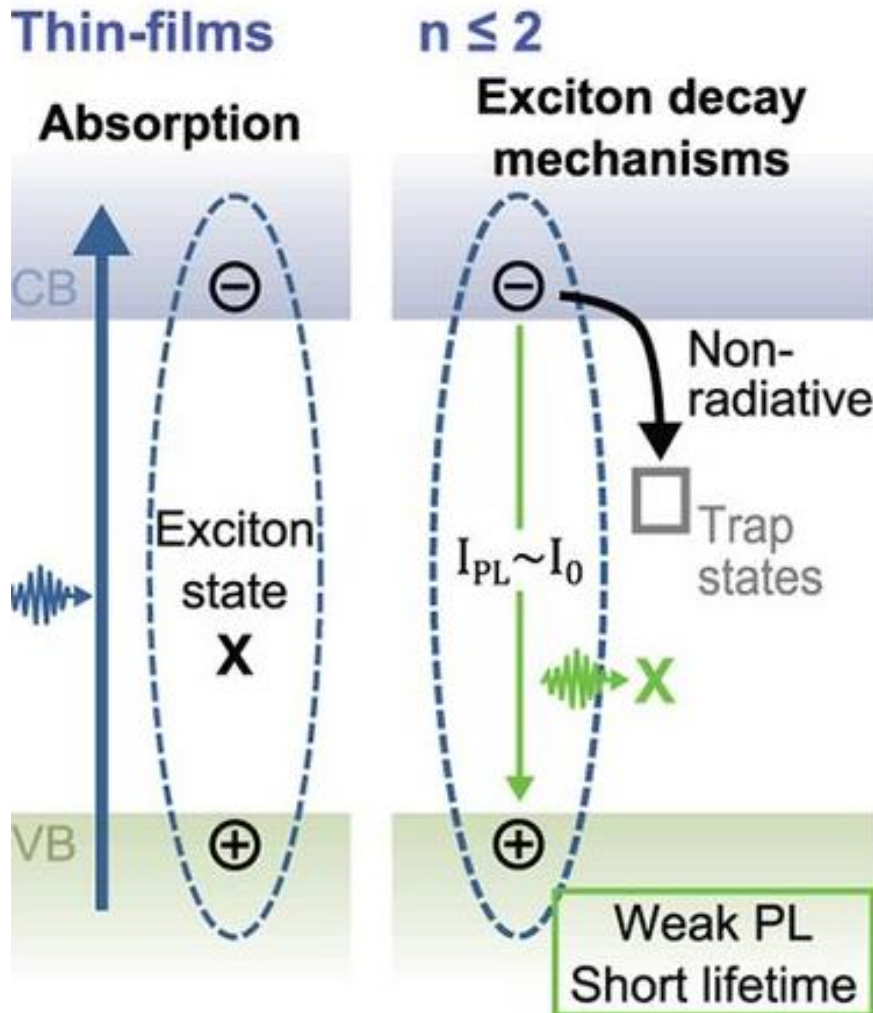
Figure 3.11: A schematic of a generated exciton state and a possible decay mechanism via trap states. Reproduced and adapted with permission from Ref [5]. Copyright 2017 American Association for the Advancement of Science

Trap States

Trap states refer to deep states in the band gap of a semiconductor that immobilize charge carriers and inhibit charge transport, which is detrimental to the solar cell performance. To maximize

solar cell efficiency, the density of trap states should be minimized to reduce competing electron-hole recombination channels.[207, 208] Wu et $al.$ studied excitonic trap states in $(BA)_2Pb_{n-1}I_{3n+1}$ and a trend of increasing trap states with decreasing layer thickness and increasing relative surface area, and attributed this to the localization of the trap states at the crystallite surface.[134] They concluded that the trap states are likely caused by the electron-phonon coupling and are enhanced at surfaces/interfaces. In contrast, Blancon et $al.$ found that edge states in the layered 2D perovskites $(BA)_2(MA)_{n-1}Pb_nI_{3n+1}$ ($n > 2$) extended the optical absorption from visible to near infrared and more importantly provided a direct pathway to dissociate excitons into free charge carriers, which substantially improved the performance of optoelectronic deivces.[5]

Byun $et.$ $al.$ found that a higher proportion of 2D material in $(PEA)_2(MA)_{n-1}Pb_nBr_{3n+1}$ reduces deep traps, thereby reducing non-radiative recombination.[117] The quasi-2D perovskite, $(PEA)_2(MA)_{n-1}Pb_nBr_{3n+1}$, by Yuan $et.$ $al.$ was found to concentrate carriers on small bandgap grains, resulting in increased local excitation intensity and high PLQY by outcompeting non-radiative recombination sites.[119] Zhou et $al.$ found that appropriate FA^+ incorporation into $(BA)_2(MA,FA)_3Pb_4I_{13}$ produces high-quality films that can reduce nonradiative recombination centers.[144] Peng et $al.$ found low self-doping in single crystals of $(PEA)_2(MA)_{n-1}Pb_nI_{3n+1}$ ($n = 1, 2, 3$), over 3 orders of magnitude lower than that of typical 3D hybrid perovskites. They proposed that the self-doping concentration difference results from the large organic cations which effect a defect-suppressing crystallization process. This low self-doping property of 2D perovskites reduces the electronic noise in photodetectors, allowing for potential applications in optoelectronic devices that measure weak signals.[175]

Multiferroic Properties

Ferroelectricity and ferromagnetism refer to the stable and switchable electrical polarization and magnetization in a material, respectively. Some layered organic-inorganic hybrid compounds have demonstrated ferromagnetic or ferroelectric properties. For instance, the compounds A_2CuCl_4 (where A = 4-fluoroanilinium and 4-chloroanilinium) were found to exhibit long-range ferromag-

netic ordering.[157] Liao *et al.* reported a high-temperature molecular ferroelectric behavior in $(BZA)_2PbCl_4$ with a curie temperature T_c = 438 K and ferroelectric polarization P_s = 13 μ C cm^{-2}.[158] Han *et al.* synthesized the layered perovskite-like $(MA)_2[Fe^{II}Cl_4]$ and studied its structural and magnetic phase transitions.[168] The authors reported a structural phase transition from high-symmetry *I4/mmm* (T > 335 K) to the low-symmetry *Pccn* (T < 335 K), and found a hidden-canted antiferromagnetic ground state that can be transformed into a canted antiferromagnet with a metamagnetic critical field greater than 200 Oe. The inorganic-organic hybrid $(PEA)_2CuCl_4$ is a ferromagnetic insulator and its inorganic component consisting of 2D perovskite-like sheets exhibit a long-range ferromagnetic order below 13 K.[209, 210] Arkenbout *et al.* reported that the cooperative distortion of the inorganic octahedra caused by Jahn-Teller distortion introduces an antiferrodis-tortive arrangement of the octahedra, thus leading to the ferromagnetic interactions.[211] Polyakov *et al.* observed a coexistence of ferromagnetic and ferroelectric ordering in the $(PEA)_2CuCl_4$ with an improper ferroelectric order below 340 K and a ferromagnetic order below 13 K.[170] By using XRD measurement, they showed that the electric polarization arises from the spatial ordering of hydrogen bonds that link PEA cations to the inorganic $CuCl_6$ octahedra. The buckling of the corner-linked $CuCl_6$ octahedra induces the hydrogen bond ordering that is also coupled to magnetic superexchange, suggesting that the material has potentially large magnetoelectric coupling.

High Water Stability

One of the major challenges preventing 3D perovskites from industrial application is low stability, especially in the presence of ambient water vapor. 2D perovskites serve as a promising solution to this challenge, demonstrating higher stability in the presence of water vapor compared to the 3D material.[112] According to XRD analysis, $(BA)_2(MA)_2Pb_3I_{10}$ exposed to 40% humidity for 2 months did not reveal a PbI_2 peak, demonstrating high moisture resistance.[4] In the Sn-based perovskites, unencapsulated $MASnI_3$ exposed to air degraded to zero in 3 minutes while $(BA)_2(MA)_3Sn_4I_{13}$ under similar conditions only gradually degraded after 30 minutes. When encapsulated, $(BA)_2(MA)_3Sn_4I_{13}$ was found to retain 90% of its original efficiency after one

month.[114] The near-single-crystalline-quality device by Tsai *et al.* placed under 65% humidity yielded similar results, retaining 70% of its original PCE after 94 days while the traditional 3D device falls to < 10% after the same amount of time.[115] Their results are summarized in Figure 3.12. The unencapsulated 2D/3D stacking structures by Lin *et al.* exposed to heating at 95 °C for 100 h maintained 96.5% and 88.2% efficiency for BA and BAI treatments respectively while their control device degraded to 69.6%.[126]

Vassilakopoulou *et al.* fabricated stable, single layer LED devices composed of mixtures of quasi-2D $(OL)_2(MA)_{n-1}Pb_nX_{3n+1}$ (OL = Oleylamine), $(PEA)_2(MA)_{n-1}Pb_nX_{3n+1}$, or $(C12)_2(MA)_{n-1}Pb_nX_{3n+1}$. They exposed the devices to air and light in an unheated and humid environment and found that they continued to show stable light emission after four months via PL and PL excitation spectra.[145] Cheng *et al.* demonstrated that unlike $MAGeI_3$, $(PEA)_2Ge_{0.5}Sn_{0.5}I_4$ did not show any diffraction peaks of GeI_4 after being exposed to ambient air at 50% relative humidity for 15 h.[176] The 2D/3D perovskite junction device composed of $(AVA)_2PbI_4/(MA)PbI_3$ (AVA = Aminovaleric acid) fabricated by Grancini *et al.* showed no loss in performance after > 10,000 hours.[139] Iagher *et al.* found that incorporating Cs into $n = 40$ quasi-2D perovskites of $(R)_2(A)_{n-1}Pb_nI_{3n+1}$ (R = PEA, BA, or CHA, A = MA and/or Cs) led to traces of PbI_2 in the XRD spectra that were not present in the pure quasi-2D perovskite devices after exposure to 205 h of 1 sun illumination and 50% humidity. They attributed this lower stability to the mixture of cations of different ionic radii, leading to strains in the perovskite structure. They also found that the aromatic ring-containing perovskites demonstrate better stability than their cyclic ring-containing counterparts.[212] The LED devices of Jia *et al.* composed of $(TFA)_2(MA)_{n-1}Pb_nBr_{3n+1}$ showed no changes in the XRD pattern after exposure to 2688 h in air. The high stability is attributed to the hydrophobicity of the F atoms and the stabilizing intermolecular hydrogen bonds.[152]

63
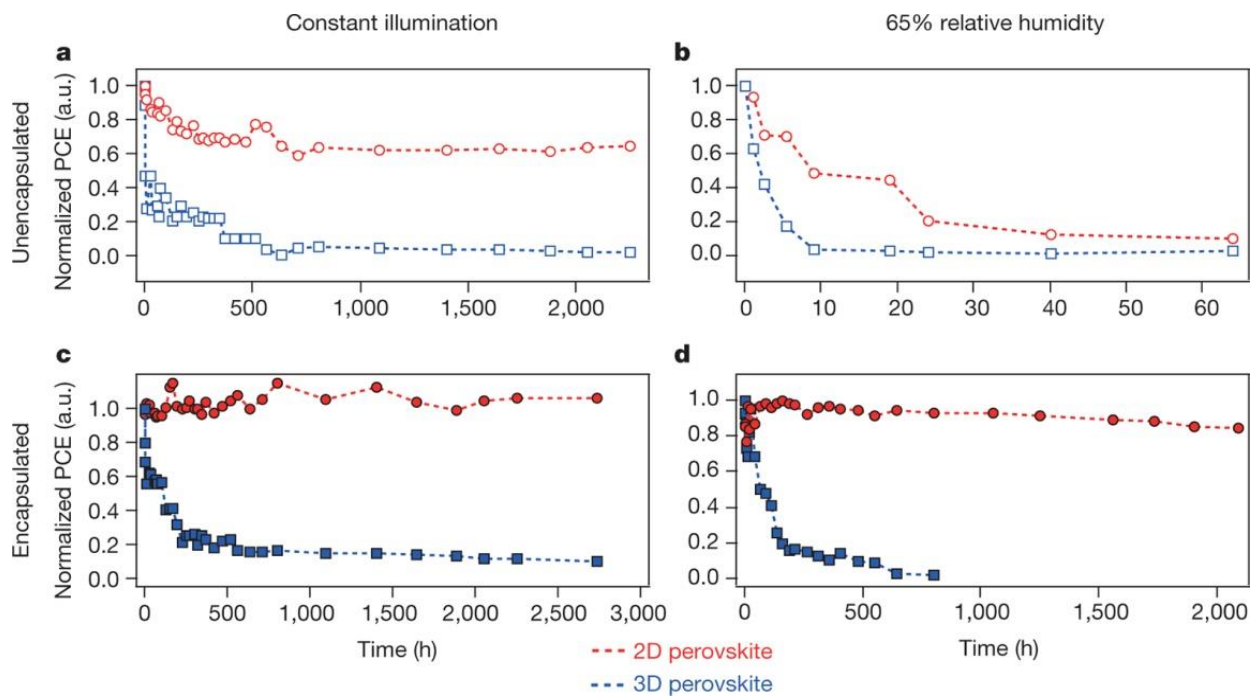
Figure 3.12: a, c, Photostability tests under constant AM1.5G illumination for 2D ((BA)$_2$(MA)$_3$Pb$_4$I$_{13}$; red) and 3D ((MA)PbI$_3$; blue) perovskite devices without (a) and with (c) encapsulation. b, d, Humidity stability tests under 65% relative humidity at in a humidity chamber for 2D ((BA)$_2$(MA)$_3$Pb$_4$I$_{13}$; red) and 3D ((MA)PbI$_3$; blue) perovskite devices without (b) and with (d) encapsulation. PCE, power conversion efficiency; a.u., arbitrary units. Reproduced and adapted with permission from Ref [115]. Copyright 2016 Springer Nature.

Table 3.6: The photovoltaic performances of several 2D perovskite-based solar cells.

Compound	PCE (%)	$V_{OC}(V)$	J_{sc} (mA/cm^2)	FF (%)	Ref
$(BA)_2(MA)_2Pb_3I_{10}$	4.02	0.929	9.43	46	[4]
$(BA)_2(MA)_3Pb_4I_{13}$	12.51	1.01	16.76	74.13	[115]
$(BA)_2(MA)_4Pb_5I_{16}$	8.71	1	11.44	75.79	[167]
$(BA)_2(MA)_3Sn_4I_{13}$	2.53	0.376	8.7	45.7	[114]
$(PEA)_2(MA)_2Pb_3I_{10}$	4.73	1.18	6.72	60	[120]
$(PEA)_2(MA)_{49}Pb_{50}I_{151}$	8.5	1.46	9.0	65	[118]
$(MA)_2CuCl_2Br_2$	0.017	0.256	0.216	32	[138]
$(HOOC(CH_2)_4NH_3)_2PbI_4/(MA)PbI_3$	14.6	1.025	18.84	75.5	[139]
$(C6)_2(MA)Pb_2I_7$	0.336	0.71	1.33	35.5	[137]
$(C6)_2(FA)Pb_2I_7$	1.26	0.733	2.98	57.4	[137]
$(C6)_2(Cs)Pb_2I_7$	0.103	0.327	0.682	46.2	[137]
$(IC_2H_4NH_3)_2(MA)_{n-1}Pb_nI_{3n+1}$	8	0.893	14.33	63	[140]
$(IC_2H_4NH_3)_2(MA,FA)_{n-1}Pb_nI_{3n+1}$	9.03	0.883	14.88	69	[140]
$(HA)PbI_4$	1.13	0.91	2.65	46.7	[127]
$(PEA)_2(MA)_{39}Pb_{40}I_{121}$ + 10% Cs	12.6	0.9	24	59	[212]
$(BA)_2(MA)_{39}Pb_{40}I_{121}$ + 10% Cs	10.2	0.86	21.4	55	[212]
$(CHA)_2(MA)_{39}Pb_{40}I_{121}$ + 10% Cs	10.6	0.86	21.9	56	[212]
$(3AMP)(MA)_3Pb_4I_{13}$	7.32	1.06	10.17	67.6	[2]
$(4AMP)(MA)_2Pb_3I_{10}$	2.02	0.99	3.05	66.4	[2]
$(BA)_2PbI_4/(MA)PbI_3$	19.56	1.11	22.49	78	[126]
$(BA)_2(MA)_{n-1}Pb_nI_{3n+1}/(MA)PbI_3$	18.85	1.09	22.59	77	[126]
$(BA)_2(MA)_{0.8}FA_{0.2})_3Pb_4I_{13}$	12.81	0.999	18.12	70.79	[144]

3.2.3 Device Performance

There have been several groups that have fabricated solar cells incorporating 2D perovskites, however these devices do not yet show efficiencies comparable to those of the 3D perovskite $(MA)PbI_3$. The device performances of 2D perovskite based solar cells have been summarized in Table 3.6. There are four criteria used to evaluate solar cell performance: (1) PCE, (2) open circuit voltage (V_{OC}), (3) short circuit current density (J_{sc}), and (4) fill factor (FF). These four parameters are different measurements of the useful energy output of a solar cell device. An ideal solar cell should demonstrate high values for each of these four parameters. (1) The PCE is the ratio between useful energy output and energy input in percentage. (2) The V_{OC} is the maximum voltage a solar cell will provide at zero current in volts. (3) The J_{sc} is the current across the solar cell in amperes per unit area when the solar cell is short circuited, where the voltage is zero. (4) The FF is the power at the maximum power point (P_m) divided by V_{OC} and the short circuit current (I_{sc}) in percentage as shown below:

$$FF = \frac{P_m}{V_{oc} \times I_{sc}} \tag{3.1}$$

A 2D perovskite solar cell device composed of $(BA)_2(MA)_2Pb_3I_{10}$ fabricated by Cao *et al.* has shown a photogenerated V_{OC} of 929 mV, J_{sc} of 9.43 mA/cm^2, FF of 46% and a PCE of 4.02% under AM 1.5G solar illumination.[4] By raising the dimensionality by two to yield $(BA)_2(MA)_4Pb_5I_{16}$, Stoumpos *et al.* achieved a PCE of 8.71%, V_{OC} of 1.0 V, J_{SC} of 11.44 mA/cm^2, and a FF of 75.79%.[167] Their Sn-based 2D perovskite device by Cao *et al.* has shown a photogenerated V_{OC} of 376 mV, J_{sc} of 8.7 mA/cm^2, FF of 45.7 % and conversion efficiencies around 2%.[114] The near-single-crystalline-quality perovskite thin film solar cell fabricated by Tsai *et al.* showed a peak PCE of 12.51%, V_{OC} of 1.01 V, J_{sc} of 16.76 mA cm^{-2}, and FF of 74.13%. They attributed this superior performance to enhanced charge transport and mobility due to near-perfect vertical orientation of the 2D layers relative to the substrate. Figure 3.13 summarizes their device architecture and characterization.[115] A device composed purely of the quasi-2D

perovskite $(PEA)_2(MA)_{n-1}Pb_nBr_{3n+1}$ (n = 40, 50, and 60) demonstrated a PCE of 6.3%, V_{OC} of 1.3 V, J_{sc} of 8.4 mA/cm^2, and FF of 50% without hole transport material (HTM) and V_{OC} of PCE of 8.5%, 1.46 V, J_{sc} of 9.0 mA/cm^2, and FF of 65% with HTM. They found V_{OC} and efficiency to peak at n = 40-50, attributing this result to reduced mobility and transport.[118] Smith *et al.* have shown that a device employing $(PEA)_2(MA)_2Pb_3I_{10}$ as the absorber can demonstrate a PCE up to 4.73% with a V_{OC} of 1.18 V, J_{sc} of 6.72 mA/cm^2, and FF of 60%.[120] The solar cell composed of $(MA)_2CuCl_2Br_2$ by Cortecchia *et al.* yielded a PCE of 0.017%, with a V_{OC} of 256 mV, J_{sc} of 216 μA/cm2, and FF of 32%.[138] Grancini *et al.* combined the 2D perovskite, $(HOOC(CH_2)_4NH_3)_2PbI_4$, with the high efficiencies of the 3D perovskite, $(MA)PbI_3$, to design a highly stable 2D/3D perovskite junction with 14.6% PCE, V_{OC} of 1.025 V, J_{sc} of 18.84 mA/cm^2, and FF of 75.5%.[139] The solar cell devices by Hamaguchi *et al.* composed of $(C6)_2(FA)Pb_2I_7$ demonstrated a maximum PCE of 1.26%, J_{sc} of 2.98 mA/cm^2, V_{OC} of 0.733 V, and FF of 57.4%. They attributed these low PCE values to a lack of light absorption in a narrow wavelength range (550-600 nm). They also found a higher short-circuit photocurrent density with a higher proportion of perpendicular orientation growth relative to the substrate.[137] The device by Koh *et al.* composed of the quasi-2D perovskite, $(IC_2H_4NH_3)_2(MA)_{n-1}Pb_nI_{3n+1}$, demonstrated a conversion efficiency over 9%. They found efficiency to increase with prolonged dipping in the MAI solution up to 4 minutes, after which it began decreasing. The efficiency was also found to improve with preferential crystal orientation and with the addition of the FA cation.[140] Mao *et al.* reached a PCE of 1.13%, V_{OC} of 0.91 V, J_{sc} of 2.65 mA/cm^2, and FF of 46.7% in their device containing $(HA)PbI_4$.[127] In n = 40 quasi-2D perovskites, the performance improved with the addition of 10% Cs across devices containing PEA, BA, and CHA based perovskites.[212] The Dion–Jacobson perovskite devices by Mao *et al.* obtained a PCE of 7.32% and 2.02%, a J_{sc} of 10.17 mA cm^{-2} and 3.05 mA cm^{-2}, a V_{OC} of 1.06 V and 0.99 V, and a FF of 67.6% and 66.4% for $(3AMP)(MA)_3Pb_4I_{13}$ and $(4AMP)(MA)_2Pb_3I_{10}$ respectively.[2] In the 2D/3D stacking structures by Lin *et al.*, BA treated devices reached a PCE of 19.56%, J_{sc} of 22.49 mA/cm^2, V_{OC} of 1.11 V, and FF of 0.78 while their BAI-treated devices obtained a PCE of 18.85%, J_{sc} of 22.59 mA/cm^2, V_{OC} of 1.09 V, and FF of

0.77. They attributed the enhanced efficiency to the healing of the surface defects due to the 2D perovskite formation.[126] The quasi-2D perovskite $(BA)_2(MA)_{0.8}FA_{0.2})_3Pb_4I_{13}$ by Zhou *et al.* obtained a PCE of 12.81%, V_{OC} of 0.999 V, J_{sc} of 18.12 mA/cm^2, and FF of 70.79%.[144]

3.3   Theoretical Research

In this section, we discussed recent first-principles computational and theoretical studies of 2DHPs. The calculated band structures of semiconductors from first-principles calculations often provide useful insights into the electronic properties of materials including the type of band gap, charge carrier mobility, and orbital-resolved contributions to the valence band and conduction band. The layered structural characteristics of 2D materials strongly affect their stability and electronic properties including charge carrier transport and band gap. Some common findings of 2DHPs include bandgap tunability through adjusting layer thickness or compositions,charge carrier mobility anisotropy, and high chemical stability.

3.3.1   Tunable Band Gaps

2DHPs typically have a tunable band gap as a function of the thickness of inorganic layers and exhibit wider band gaps compared to 3D hybrid perovskites. [120, 213, 214] For instance, in our previous first-principles computational studies of $(BA)_2(MA)_{n-1}Ge_nI_{3n+1}$,[156] we found that band gap decreases with increasing *n* values, ranging from 1.88, 1.83, 1.69 to 1.57 eV for n = 1, 2, 3, and ∞, as shown in Figure 3.14. Moreover, the conduction band is mainly composed of Ge 4*p* states while the valence band is mainly composed of I 5*p* states, neither having any contribution from the organic molecules near the band edges. Peng *et al.* calculated the band gaps of $(PEA)_2(MA)_{n-1}Pb_nI_{3n+1}$ to be 2.31 (*n* = 1), 2.17 (*n* = 2), and 1.95 eV (*n* = 3) without spin-orbit coupling, in good agreement with their experimental findings, while 1.43 (*n* = 1), 1.20 (*n* = 2), and 0.91 eV (*n* = 3) with spin-orbit-coupling.[175] The calculated band gaps of $(BA)_2(MA)_{n-1}Pb_nI_{3n+1}$ were found to range from 1.2 (bulk) to 2.0 eV (monolayer),[115] comparable to the experimental values of
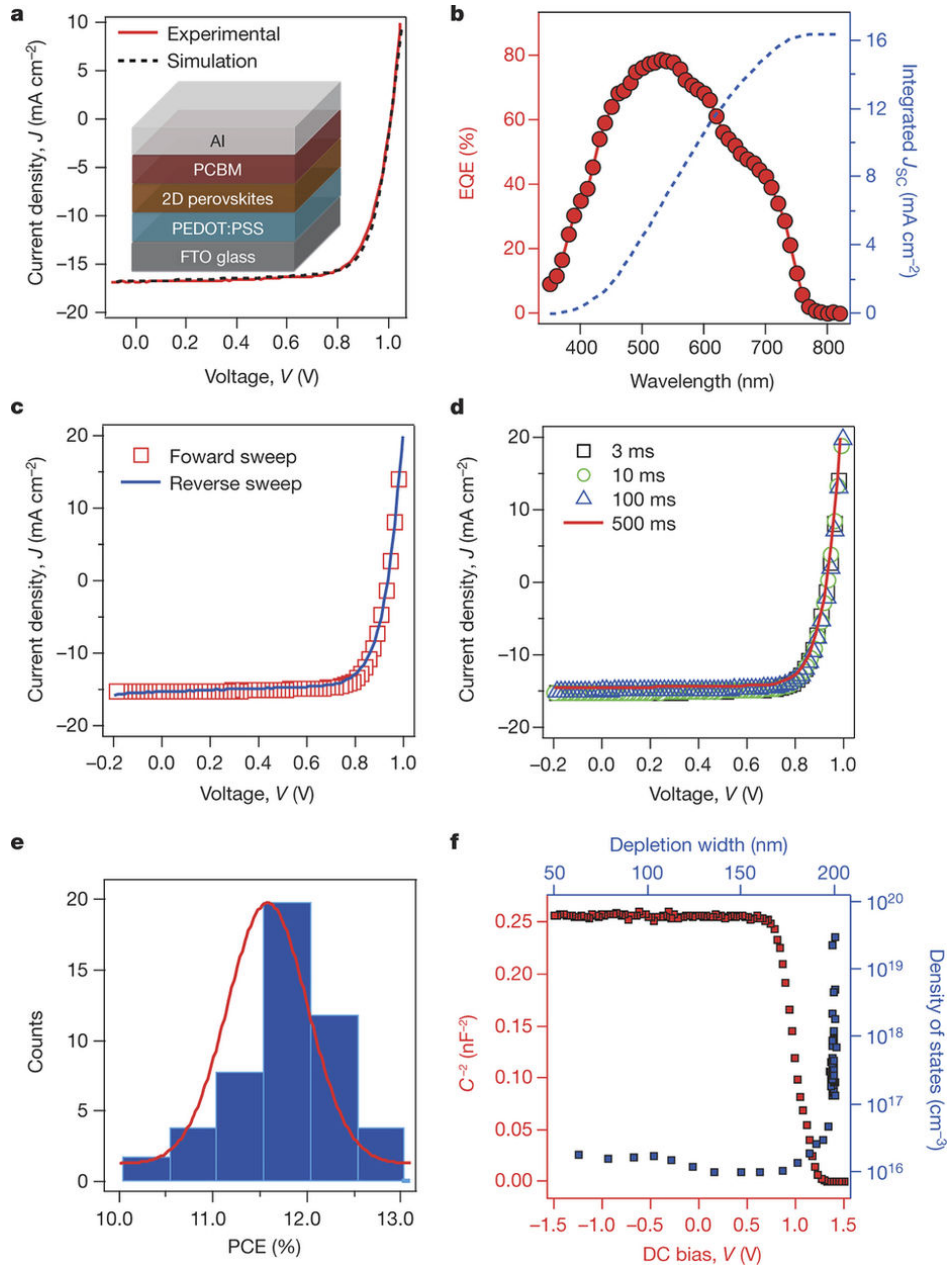
Figure 3.13: a, Experimental (red) and simulated (black) current-density-voltage (J–V) curves using 2D $(BA)_2(MA)_3Pb_4I_{13}$ perovskites as the absorbing layer with a schematic of the device architecture. b, External quantum efficiency (EQE; red) and integrated short- circuit current density (JSC; blue) as a function of wavelength. c, d, J–V curves for hysteresis tests under AM1.5G illumination measured with the voltage scanned in opposite directions (c) and with varying voltage delay times (d). e, Histogram of device PCE over 50 measured devices, fitted with a Gaussian distribution (red). f, Capacitance-d.c. bias (C–V) curves (red) for a typical device and the corresponding charge density profile (blue). Reproduced and adapted with permission from Ref [115]. Copyright Springer Nature.
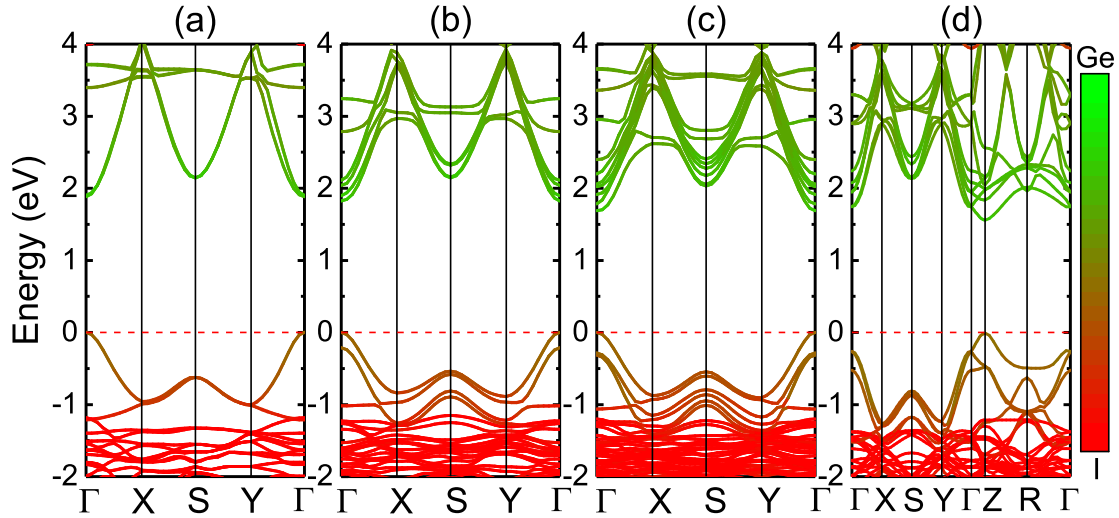
Figure 3.14: Calculated HSE06 projected-band structures of 2D $(BA)_2(MA)_{n-1}Ge_nI_{3n+1}$ and 3D $MAGeI_3$ perovskites, (a) $n=1$, (b) $n=2$, (c) (a) $n=3$, and (d) $n=\infty$, along the $\Gamma(0,0,0)$-$X(0.5,0,0)$-$S(0.5,0.5,0)$-$Y(0,0.5,0)$-$\Gamma(0,0,0)$-$Z(0,0,0.5)$-$R(0.5,0.5,0.5)$ path through the first Brillouin zone. The Fermi level is set to be zero and indicated by the red horizontal dash line. The relative contribution of Ge and I are marked by color, in which green (red) corresponds to the state originating from Ge (I). Reproduced and adapted from [156]. with permission from The Royal Society of Chemistry.

1.52 (bulk) to 2.24 eV (monolayer).[4] Grancini *et al.* carried out first-principles calculations for the 2D/3D perovskite interface, $(HOOC(CH_2)_4NH_3)_2PbI_4/(MA)PbI_3$, and found that at the $(HOOC(CH_2)_4NH_3)_2PbI_4/(MA)PbI_3$ junction, there is a 0.14 eV CB upshift which induces a 0.09 eV larger interface gap compared to the 3D bulk, consistent with their experimentally observed 0.13 eV PL blue shift.[139]

In addition to tuning band gaps of 2DHPs through quantum size effects, another common approach is to adjust compositions of materials. For instance, Lanty *et al.* found that the band gaps of mixed halide perovskites, $(PEA)_2PbZ_{4(1-x)}Y_{4x}$ (Z, Y = Cl, Br, or I), can be tuned from 2.4 to 3.1 and 3.7 eV through changing compositions of anions. The authors also demonstrated that these mixed halide perovskites can be considered as psuedobinary alloys like $Ga_{1-x}Al_xAs$, $Cd_{1-x}Hg_xTe$ inorganic semiconductors in which the Y and Z atoms are distributed randomly and uniformly rather than being grouped into some aggregates in the crystal, allowing for a similar model to be applied to describe the crystal's excitons.[133] Cortecchia *et al.* demonstrated bandgap tunability

of Cu-based perovskites, $(MA)_2CuCl_xBr_{4-x}$, through Cl/Br ratio modification using *ab initio* DFT calculations.[138] The calculated band gaps range from 3.09 to 3.00, to 2.88, and to 2.86 eV for x = 4, 2, 1, and 0.5 respectively. Fraccarollo *et al.* calculated band gaps of $(IMI)SnI_4$ and $(PYR)SnI_4$ with values around 1.34-1.78 eV using first-principles DFT calculations by including SOC and GW effects, and attributed the low band gap to the degenerate levels at the bottom of the conduction bands that are strongly localized in the interlayer space.[215]

3.3.2 Mobility Anisotropy

The behavior of charge carriers in semiconducting materials plays an important role in the functionality of optoelectronic devices. To ensure efficient charge transfer, the charge carriers should have high mobility, long lifetimes, and low effective masses. One important character of 2DHPs is the conductivity anisotropy similar to that of two-dimensional electron gases in semiconductor heterostructures.[216] This characteristic means that the charge carriers are highly mobile parallel to the inorganic layers, but immobile in the perpendicular direction across the insulating organic layers.[130, 123, 116, 138] In the side of theoretical and computational studies, the conductivity anisotropy is often indicated by the electron and hole effective masses from the first-principles electronic structure calculations. For instance, in our prior work on $(BA)_2(MA)_{n-1}Pb_nI_{3n+1}$, our calculations show low charge carrier effective masses within the 2D plane but extremely large effective masses in the out-of-plane direction, implying a strong moiblity anistropy.[156] Similar phenomena also occur in other 2DHPs, such as $(BA)_2Pb_nI_{3n+1}$,[123] $(MA)_2Pb(SCN)_2I_2$,[116] and $(MA)_2CuCl_xBr_{4-x}$.[217] Figure 3.15 shows crystal structure, Brillouin zone, electronic band structure, and density of states of the 2DHP $(MA)_2Pb(SCN)_2I_2$.[130] The flat bottom conduction band and top valence band along the *k*-path T-R and Γ-X suggest that the calculated effective masses for holes and electrons approach infinity, and these two reciprocal paths correspond to the *a* direction of the crystal structure in the real space, see Figure 3.15a-c. This implies that the charge carriers do not travel between the inorganic layers and thus are tightly confined to the 2D inorganic
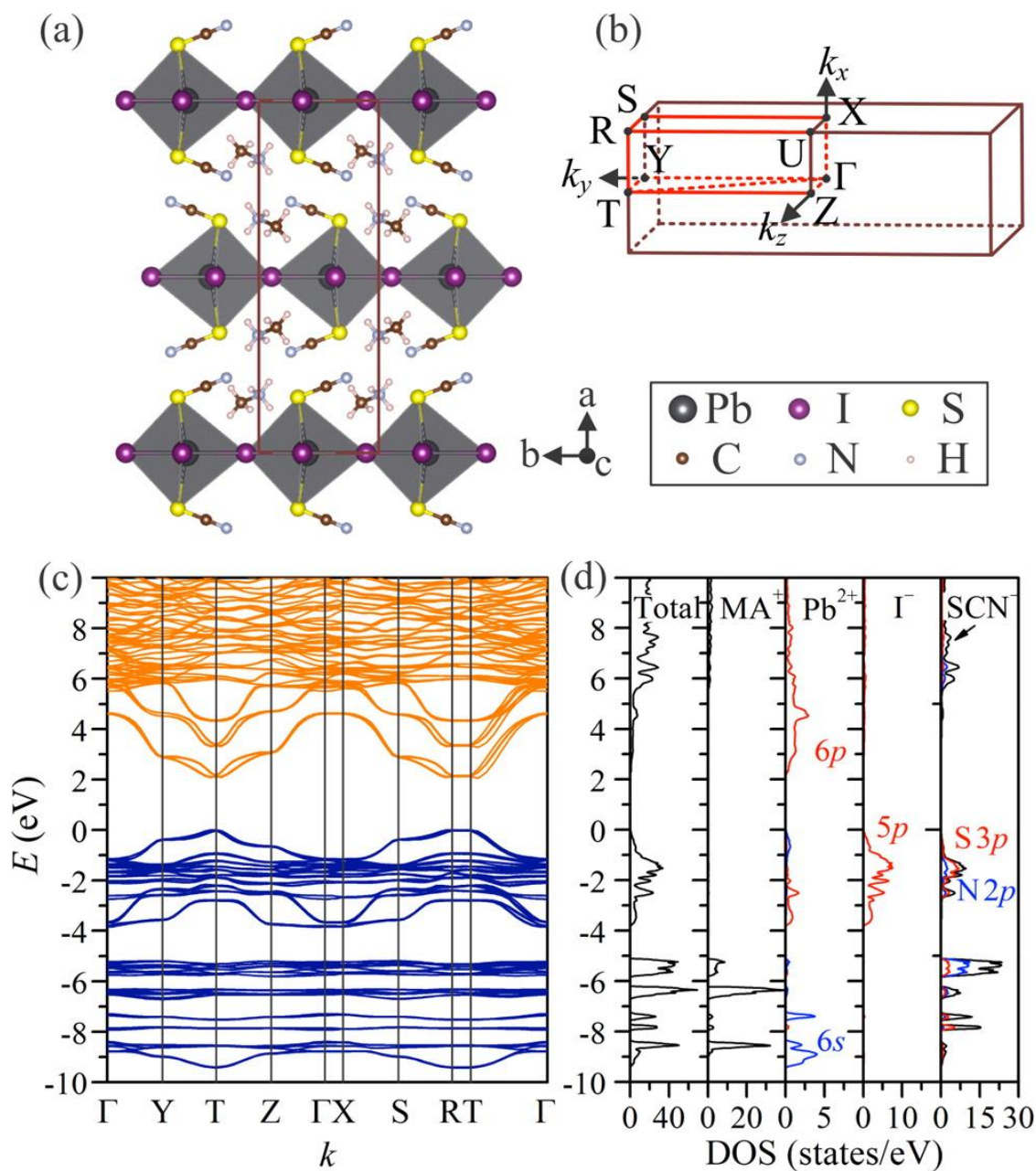
Figure 3.15: Structural and electronic properties of orthorhombic $(MA)_2Pb(SCN)_2I_2$. (a) Crystal structure viewed along the [001] direction, (b) first Brillouin zone and the k-path used to calculate electronic band structure, (c) calculated electronic band structure and (d) density of states with the $HSE^{\alpha=43\%}$+SOC method. Reproduced and adapted with permission from Ref [130]. Copyright 2016 American Chemical Society.

plane, indicating a strong mobility anisotropy. The calculated density of states (DOS) shows that

valence band mostly consists of I $5p$ and S $3p$ states while the conduction band mainly consists of

Pb 6*p* states, see Figure 3.15d. The calculated effective masses for several 2D perovskite materials are summarized in Table 3.7.

3.3.3   Defect States

Defects and self-doping can significantly influence the electronic and optical properties of a semiconductor, including the charge carrier recombination rate, charge transport, and light absoprtion and emitting.[218, 219] Therefore, the effects of defects and self-doping must be accounted for to optimize device performance and reproducibility. Liu *et al.* investigated electronic activities of defects in 2D perovskite Rb_2PbI_4 using first-principles calculations.[220] They found that deep-level defects can form easily at high μ_I (chemical potential of I) conditions, and this is significantly different from the case of 3D perovskites in which the deep-level defects are difficult to form and the dominating defects all have shallow states.[221, 222] Figure 3.16 shows the calculated electronic levels of point defects. Accordingly, they conclude that defects in 2D perovskites can be tuned to be less harmful to the electronic properties by adjusting the crystal synthesis conditions to be Pb-rich and I-poor. In addition, they also found that defects (point defects, grain boundaries, and edges) are unlikely to cause *n*-doping as in the 3D system. Booker *et al.*'s first-principles calculations indicate that iodide vacancies do not form gap states while interstitial iodide introduce deep gap states around 0.65 eV above the valence band in the 2DHP $(C_6H_{16}N)_2PbI_4$ and $(C_{12}H_{28}N)_2PbI_4$.[128] The authors' results show that the electron transition energy from the conduction band edge to these localized levels is around 2.1 eV, which is in good agreement with the white emission at 2.0 eV (625 nm).

3.3.4   Stability

2DHP and quasi-2DHP have demonstrated higher chemical stability than the 3D hybrid perovskites according to several theoretical studies. In our previous work, we have calculated

Table 3.7: Calculated effective masses parallel and perpendicular to 2D layer planes in units of the free electron rest mass, m_0.

Compound	Type	Parallel		Perpendicular	Ref
$(BA)_2PbI_4$	e^-	0.082		∞	[123]
$(BA)_2(MA)_2Pb_3I_{10}$	e^-	0.097		∞	[123]
$(BA)_2(MA)_3Pb_4I_{13}$	e^-	0.094		∞	[123]
$(BA)_2PbI_4$	h^+	0.144		∞	[123]
$(BA)_2(MA)_2Pb_3I_{10}$	h^+	0.141		∞	[123]
$(BA)_2(MA)_3Pb_4I_{13}$	h^+	0.153		∞	[123]
$(MA)_2CuCl_4$	e^-	0.31		0.58	[138]
$(MA)_2CuCl_2Br_2$	e^-	0.51		1.86	[138]
$(MA)_2CuClBr_3$	e^-	0.57		2.39	[138]
$(MA)_2CuCl_{0.5}Br_{3.5}$	e^-	0.52		4.04	[138]
$(MA)_2CuCl_4$	h^+	1.71		∞	[138]
$(MA)_2CuCl_2Br_2$	h^+	2.67		∞	[138]
$(MA)_2CuClBr_3$	h^+	1.51		∞	[138]
$(MA)_2CuCl_{0.5}Br_{3.5}$	h^+	1.55		∞	[138]
$(PEA)_2PbI_4$	e^-	0.278			[175]
$(PEA)_2(MA)Pb_2I_7$	e^-	0.198			[175]
$(PEA)_2(MA)_2Pb_3I_10$	e^-	0.214			[175]
$(PEA)_2PbI_4$	h^+	0.604			[175]
$(PEA)_2(MA)Pb_2I_7$	h^+	0.391			[175]
$(PEA)_2(MA)_2Pb_3I_10$	h^+	0.232			[175]
$(MA)_2Pb(SCN)_2I_2$	VBM	0.2			[116]
$(MA)_2Pb(SCN)_2I_2$	CBM	0.14			[116]
		T-Z [010]	T-Y [001]		
$(MA)_2Pb(SCN)_2I_2$	e^-	0.88	0.34	∞	[130]
$(MA)_2Pb(SCN)_2I_2$	e^-	0.37	0.58	∞	[172]
$(MA)_2Pb(SCN)_2I_2$	e^-(SOC)	0.17	0.2	∞	[172]
$(MA)_2Pb(SCN)_2I_2$	h^+	0.99	2.36	∞	[130]
$(MA)_2Pb(SCN)_2I_2$	h^+	1.61	1.43	∞	[172]
$(MA)_2Pb(SCN)_2I_2$	h^+(SOC)	0.36	0.45	∞	[172]
$(BA)_2GeI_4$	e^-	0.19	0.18		[156]
$(BA)_2(MA)Ge_2I_7$	e^-	0.23	0.14		[156]
$(BA)_2(MA)_2Ge_3I_{10}$	e^-	0.22	0.13		[156]
$(MA)GeI_3$	e^-	0.22	0.20		[156]
$(BA)_2GeI_4$	h^+	0.28	0.27		[156]
$(BA)_2(MA)Ge_2I_7$	h^+	0.34	0.31		[156]
$(BA)_2(MA)_2Ge_3I_{10}$	h^+	0.27	0.26		[156]
$(MA)GeI_3$	h^+	0.28	0.31		[156]
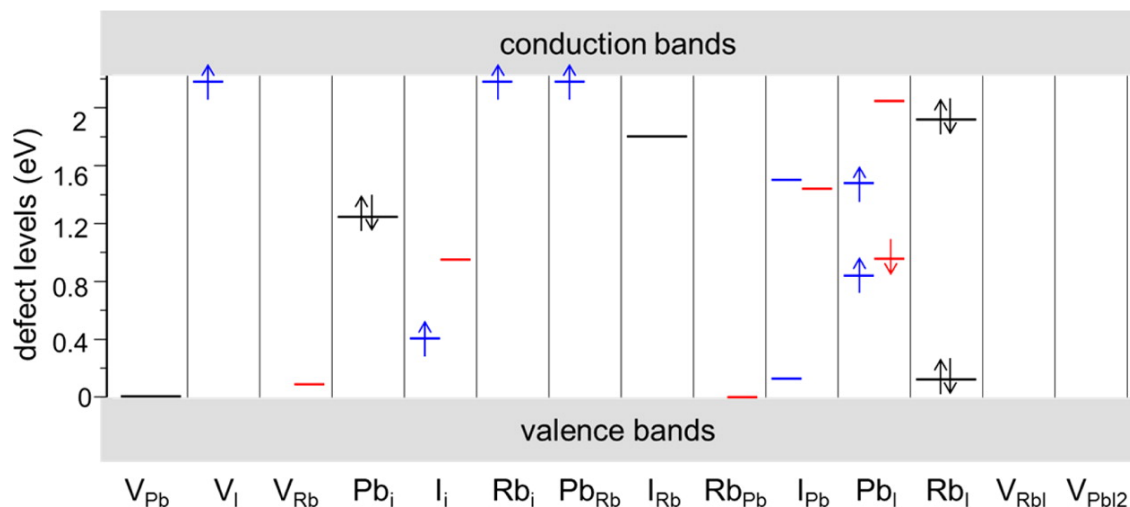
Figure 3.16: Calculated electronic levels of point defects in 2D perovskite $Rb_2Pb_2I_4$. The long and short bars denote two degenerate states and a single state, respectively. The blue and red colors indicate spin polarized states; and the occupied states are marked by arrows. Reproduced and adapted with permission from Ref [220]. Copyright 2016 American Chemical Society.

decomposition energies of $(BA)_2(MA)_{n-1}Pb_nI_{3n+1}$ ranging from 1.13 eV to 0.69 eV to 0.62 eV to 0.23 eV for $n = 1, 2, 3$, and ∞ respectively, demonstrating much higher decomposition energies and stability at lower n values.[156] Ganose *et al.*'s first-principles calculations show that the 2D layered compound $(MA)_2Pb(SCN)_2I_2$ is thermodynamically stable with respect to phase separation.[116] Quan *et al.* reported that the quasi-2DHP films exhibit improved stability while retaining the high performance of the conventional 3D perovskites using DFT calculations.[223] Figure 3.17 shows the evolution of materials stability and formation energy of $(C_8H_9NH_3)_2(CH_3NH_3)_{n-1}Pb_nI_{3n+1}$ as a function of n. Stoumpos *et al.* reported the large-scale synthesis, crystal structure, and optical characterization of layered perovskite $(BA)_2(MA)_{n-1}Pb_nI_{3n+1}$, and found that the noncentrosymmetric structures of these compounds are energetically more favorable than the centrosymmetric structures from first-principles density functional theory calculations.[123]
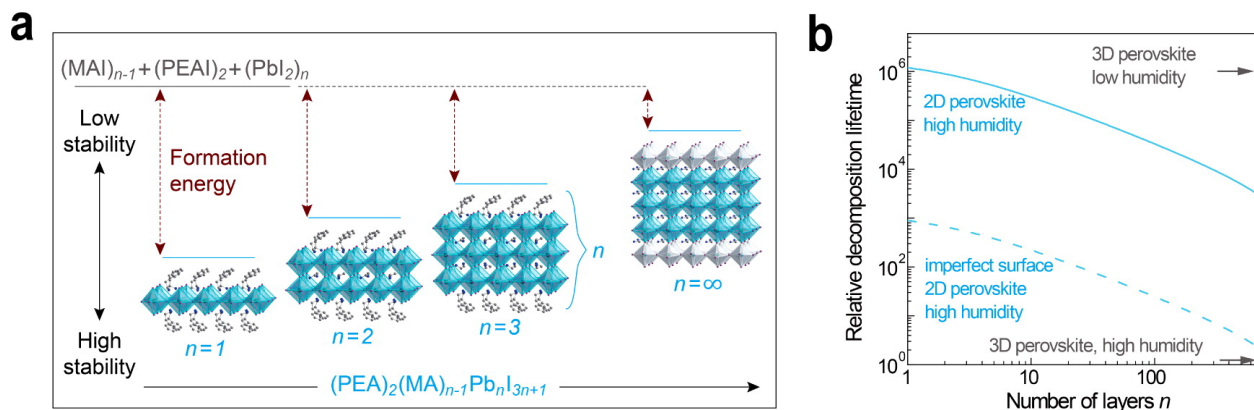
Figure 3.17: Evolution of materials stability as a function of *n* for the 2DHP $(C_8H_9NH_3)_2(CH_3NH_3)_{n-1}Pb_nI_{3n+1}$. Reproduced and adapted with permission from Ref [223]. Copyright 2016 American Chemical Society.

3.4   Summary and Outlook

This review covered the main themes of current research in the area of 2D hybrid perovskites. Although these materials have a variety of chemical compositions, they all demonstrate similar properties and synthesis routes. The most common synthesis route involves dissolving the perovskite precursors in DMF then spin-coating the solution onto a substrate. Their structure consists of distorted inorganic layers separated by large organic molecules and kept together by van der waals forces. This structure influences the perovskite's electronic properties and improves stability, even in the presence of water. The bandgap energies tend to be larger in fewer layer systems than in the 3D perovskite. The dielectric constant and charge carrier mobility are confined to the inorganic layers. Device performance is not yet comparable to that of the 3D perovskite. Theoretical studies are in good agreement with the experimental results and also provide insight into the anisotropic behavior of excitons, the dielectric constant, and charge carrier mobility in the material.

2D perovskites offer a promising solution to the stability issue in their 3D counterparts, however there is still much more work needed to improve the efficiency to allow them to be viable alternatives to 3D perovskite solar cells. There are some topics that could use greater clarity in the literature. Some possible work could include developing methods to shift the bandgap from indirect to direct in certain types of 2D perovskites or performing further study on how the distortion of the

76
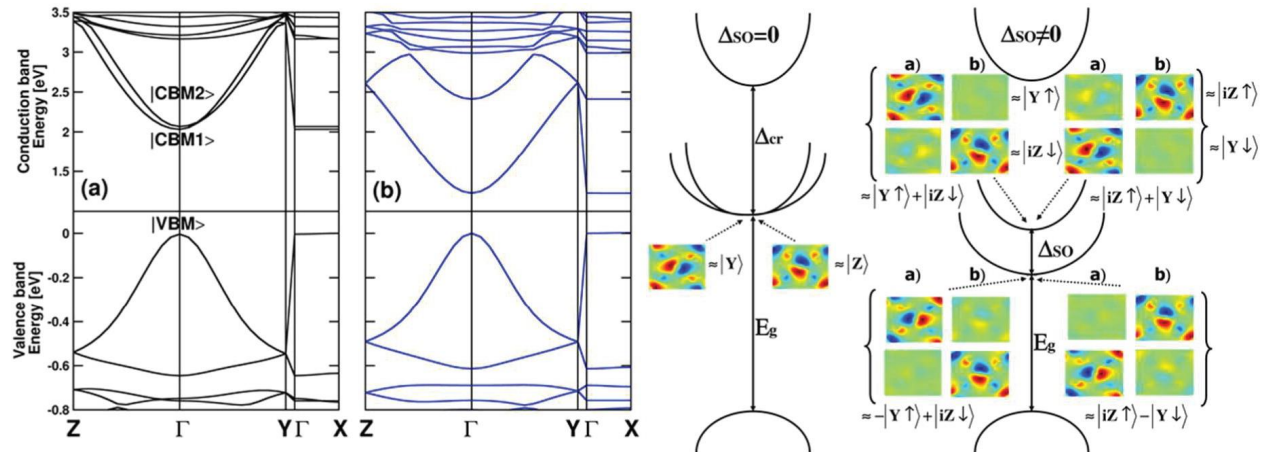
Figure 3.18: (Left) Electronic band structure of the layered HOP ([pFC$_6$H$_5$C$_2$H$_4$NH$_3$]$_2$PbI$_4$), (a) without and (b) with SOC at the GGA level of theory with the ABINIT code.[231] Energy levels are referenced to the valence band maximum. (Right) General schematic representations of a layered HOP electronic band diagram without and with SOC (Δ_{SO}). Δ_{cr} represents the anisotropy of the crystal field. This panel includes the (a) real and (b) imaginary parts of the complex spinorial components of the first and second CBM states with spin-up component on top of the spin-down component. Reproduced and adapted from Refs [231], and [232]. Copyright 2015 American Chemical Society.

inorganic layers affects electronic properties. Some more clarity could also be provided regarding the origin of trap states in low dimensionality perovskites. Due to the availability of low-temperature thin film deposition methods,[224, 225, 4] hybrid perovskites can be applied in flexible electronic devices.[226, 227, 90, 228, 229] Vassilakopoulou *et al.* embedded a mix of 2D and 3D perovskites into porous silica matrices to form flexible photoluminescent films, whose photoluminescence was not affected after prolonged exposure to water.[230] Aside from this example, reports of flexible 2D perovskite devices are sparse in the literature and remain an open area for exploration.

Beyond the DFT studies performed thus far, a semi-empirical solid state physics approach can overcome the limitations of DFT techniques in providing predictions and comparisons with experimentally derived physical parameters. From a solid state physics approach to DFT modeling, Even *et al.* suggest a treatment of layered perovskites as composite materials with very weak interactions between the inorganic layers, with a reconstruction of the whole Hartree potential profile by pieces. This allows complete conduction and valence band alignments of the organic

and inorganic layers and leads to a confinement potential for charge carriers in the inorganic layer. They also found that SOC leads to a nondegenerate state at the CBM and band dispersion at the CBM and VBM, which corresponds to a favorable configuration for optical activity. A comparison of electronic structures with and without SOC in DFT calculations is shown in Figure 3.18. They found that the optical process is governed by three active Bloch states at the Γ point of the reduced BZ (two Bloch states for the CBM and one for the VBM) with a reverse ordering compared to anisotropically bonded semiconductors. They propose that transverse electric optical activity indicates that light is absorbed at the bandgap energy only for an electrical polarization parallel to the layer.[232] Pedesseau *et al.* use solid state physics concepts and DFT simulation tools to perform a comparison between 3D and 2D hybrid perovskites. They also introduce the tetragonal D_{4h} symmetry for 2D perovskites, allowing for an analysis of the effects of brillouin zone folding on spin orbit coupling (SOC), electronic band structures, and loss of inversion symmetry.[233] Traore *et al.* provide an computationally affordable first-principles method to calculate charge carrier confinement potentials by conceptualizing 2D perovskites as composite materials consisting of pseudoinorganic and -organic components.[234]

Chapter 3, in full, is currently being prepared for submission for publication of the material. Wong, Joseph; Yang, Kesong. The thesis author was the primary investigator and author of this material.

Chapter 4

Configurational Entropy Analysis of Y-Stabilized Zirconia Grain Boundaries

4.1 Introduction

Yttria-stabilized zirconia (YSZ) is widely used as a thermal barrier coating (TBC) in gas turbine engines because of its exceptional material properties such as low thermal conductivity,[235, 236] chemical inertness,[237] phase stability at room and operational temperature,[238, 239] and a close thermal expansion match with the typical nickel-base superalloy substrate.[240] In recent years, however, the YSZ-based TBC in gas turbine engines has been exposed to a new challenge in the form of dust and sand ingestion. It is believed that the sand enters the combustion chamber and attacks the integrity of the TBC through a combination of physical and chemical effects.[241] The mechanisms behind the chemical infiltration may involve impurity segregation to grain boundaries (GBs) and the formation of siliceous phases,[242] impurity-silicates,[241] and oxide-silicon interfaces.[243] These combined effects degrade and ultimately destroy the capacity of the TBC to protect the turbine blades from the heat of the combustion chamber.[244] Closely involved in this process is the formation of calcium–magnesium–alumino silicate (CMAS). It is generally believed that the molten CMAS infiltrates the TBC upon contact at GBs,[245, 246, 247] absorbing both ziconia

and yttira and later diffusing away from GBs, and subsequently attacks the platinum-modified nickel aluminide bond coat at high temperature (over 1250° C).[244, 248, 249, 250] The CMAS infiltration through GBs implies that the impurities tend to aggregate at grain boundaries rather than internal bulk region. [251, 252, 253] Therefore, to understand the failure mechanism and damage propagation of TBCs, it is essential to investigate the impurity segregation behavior at YSZ GBs.

Significant efforts have been made to study impurity segregation in zirconia grain boundaries. Matsuda *et al.* used secondary ion mass spectrometry (SIMS) to study Ca diffusion in polycrystalline 10 mol% cubic YSZ (c–10YSZ), and observed no segregation of Ca to GBs.[254] However, a subsequent SIMS analysis by Kowalski *et al.* in c–8YSZ found a strong segregation tendency, in which Ca was almost exclusively observed at GBs. [255] Guo *et al.* studied the segregation behavior of trace SiO_2 in Al_2O_3-doped c–9YSZ samples containing both amorphous and crystalline GBs using electron probe microanalysis (EPMA) and energy-dispersive X-ray spectroscopy (EDS).[256] Interestingly, despite the presence of trace SiO_2 in their reaction powders, the authors could detect Si only within amorphous GBs rather than crystalline GBs. In 15 mol% CaO-stabilized cubic zirconia, Aoki *et al.* found that the segregation behavior of Si impurities depends on the grain size, with nearly zero segregation in the samples with the smallest grain sizes of 0.14 Âţm.[257] These results are surprising in light of the fact that the bulk solubility of SiO_2 in stabilized zirconia, roughly 0.0025 mol%, [257] is exceedingly low compared to that of CaO (19 mol%).[258] This is because, in principle, the segregation tendency is greater for the impurity with lower bulk solubility.[259, 260, 261] In short, these experimental results suggest that grain size and GB crystallinity have significant effects on the segregation tendencies of impurities, even those with low bulk solubility.

Despite substantial experimental study, a complete understanding of impurity segregation in YSZ remains elusive. This is primarily due to a lot of variations in experimental setup such as grain size, impurity concentration, and stabilizing oxides, which adds a certain level of complexity to the computational and theoretical studies. In fact, prior theoretical studies have generally been limited to studying the distribution of intrinsic defects in YSZ, such as yttrium substitutions (YZr)

or oxygen vacancies (VO). For example, Lee *et al.* reported that both YZr and VO show a modest segregation tendency to the Σ 5 (310)/[001] GB of c–10YSZ using a hybrid Monte CarloMolecular Dynamics simulation. [262] A later experimental and theoretical work found that both YZr and VO segregate to the Σ 13 (510)/[001] GB, but that VO segregates more strongly.[263] Nevertheless, few theoretical studies particularly at the quantum mechanics level have examined the distribution of extrinsic substitutional impurities in zirconia or YSZ systems. Therefore, a comprehensive theoretical study of impurity segregation is essential to fundamental understanding of impurity segregation in YSZ and to the further development of hot-corrosion-resistant YSZ-based TBCs.

While density functional theory (DFT) is currently the most successful approach to compute the total energy and electronic structure of matter, no DFT study of the YSZ GB yet exists. This is because YSZ is a chemically-disordered material with respect to the distribution of oxygen vacancies (VO) and yttrium dopants (YZr).[264] This disorder, combined with high doping concentrations of about 6-10 mol%, complicates first-principles calculations via DFT, and thus prior DFT calculations of YSZ have generally been limited to relatively simple bulk structures. For example, thanks to the use of a 96-atom bulk supercell model of YSZ, it was possible to evaluate the stability of 453 unique structures from first-principles DFT calculations. [265]

In this work, we used first-principles DFT calculations to examine Σ 5 (310)/[001] symmetric tilt YSZ GBs, as well as two closely related GBs of pristine zirconia and hafnia, and carried out a comprehensive analysis of impurity segregation in these systems. To perform the impurity segregation analysis, we first examined all microstate configurations of the YSZ GBs to determine possible ground state GB structures. We then calculate the configurational entropy to determine which of these possible ground states are statistically probably to exist. Below we discuss the thesis author's contribution to this work, namely the determination of ground state configurations and the calculation of configurational entropy of the YSZ system. The primary author of this work, Dr. Mazier Behtash, contributed a majority of the remaining work on impurity segregation in YSZ and GBs of zirconia and hafnia.

4.2 Computational Details and Structural Models

DFT calculations were carried out using the Vienna ab initio Simulation Package (VASP). [266] The projector augmented wave (PAW)[39] pseudopotentials were employed for electron-ion interactions. The generalized gradient approximation (GGA) parametrized by Perdew-Burke-Ernzerhof (PBE) [40] was used to describe the electron exchange-correlation potentials. A 400 eV cut-off energy for the plane wave basis set was used during structural relaxation, and a 2 x 2 x 1 Γ-centered k-point mesh is well-converged for self-consistent calculations. Subsequent single-point total energy calculations were carried out using the Gaussian method with a 4 x 4 x 1 Γ-centered k-point mesh, with a 480 eV cut-off energy for the plane wave basis set. All the atomic positions were relaxed until all components of the residual forces were smaller than 0.03 eV/Å, and the convergence threshold for self-consistent-field iteration was set to 10^{-5} eV. The Σ 5 (310)/[001] GB was selected for this study due to its relatively low energy and high symmetry, enabling the construction of large GB models suitable for impurity segregation analysis via DFT. Several prior MD studies have considered the Σ 5 (310)/[001] for these reasons. [262, 267] The lattice constants of our 240 atom ZrO_2 GB model are 5.14 Å, 8.13 Å, and 65.02 Åfor a, b, and c respectively.

We generated Σ 5 (310)/[001] symmetric tilt GBs of cubic ZrO_2 from an optimized unit cell. he optimized lattice parameter of the ZrO_2 unit cell is 5.14 Å, consistent with the bulk experimental value of 5.10 Å.[268] We build c–YSZ Gs from this pristine ZrO_2 GB and introduce a suitable number of V_O and Y_{Zr}, making the composition comparable with the experimental case. Considering the intrinsic symmetry of the periodic ZrO_2 GB model, we introduced two Y atoms and one oxygen vacancy in one half region of one ZrO_2 grain, and then applied mirror symmetry operation to get the same distribution of Y atoms and oxygen vacancy in the other grain. That is, substituting two Zr atoms with two Y atoms from 20 cation sites and removing one O atom from 40 anion sites leads to a total number of all the possible structural configurations of C_{20}^2 x C_{40}^1 =7600, which corresponds to a 5 mol% Y_2O_3, or 5YSZ.

To have a statistical analysis of the energetics of the 7600 configurations, we carried out
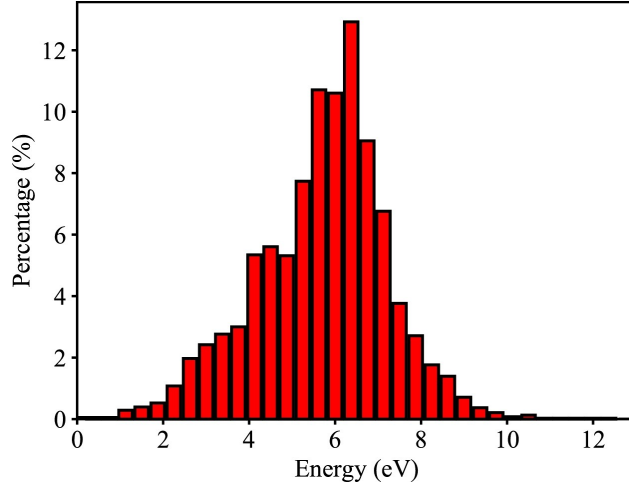
Figure 4.1: Energy distribution of 7600 structural configurations of 5YSZ GB model. All these structures are relaxed by empirical potential calculations.

empirical-potential calculations to relax all the 7600 structures using General Utility Lattice Program (GULP).[269] The related force field parameters were adopted from Ref.[270] The calculated energies are shown in Figure 4.1, which follows a Gaussian distribution with a spanning of about 13 eV. This result is in good agreement with prior empirical-potential calculations on the supercell model of 8YSZ bulk material.[271]

Next, we analyzed the contributions of vibrational and configurational entropies of the 7600 configurations. The vibrational entropy at 1000K was estimated from the phonon spectra calculated in GULP. As discussed below, the vibrational entropy will be considered by adding their contributions in the total energy of each configuration for estimating the configurational entropy, following the same approach in Dong's *et al.* simulation work.[271] The configurational entropy term, *ST*, can be calculated with the Boltzmann entropy formula,

$$S = -k_B \sum_{i=1}^{W} P_i \ln P_i, \qquad (4.1)$$

where k_B is the boltzmann constant, W is the number of configurations, and P_i is the probability of

the system existing in microstate i. We consider our system to be a canonical ensemble, where the system is in thermal equilibrium with a heat bath at a constant temperature. In a canonical ensemble, P_i can be calculated from

$$P_i = \frac{g_i e^{-\Delta E/k_B T}}{\sum_{i=1}^{W} g_i e^{-\Delta E/k_B T}}, \tag{4.2}$$

where g_i is the degeneracy of microstate i according to structural symmetry, ΔE is the microstate energy difference relative to the lowest energy configuration, and T is the temperature.[272] ΔE is obtained directly from optimized structures, and T is set to 1000K (about 1/3 of the melting point of ZrO_2).[271]

4.3   Results and Discussion

From 4.1 and 4.2, we calculated the configurational entropy term of our 7600 YSZ grain-boundary structures to be 0.0165 eV. This value is less than the results of Dong *et al.* who calculated a configurational entropy term of 0.08 eV because our 5YSZ system has far fewer possible configurations compared to their 100,000 randomly sampled 8YSZ configurations. By adding the contributions of vibration entropy to the total energy, we re-calculated the configurational entropy to be 0.02 eV. This indicates that only states within about 0.02 eV above the lowest energy are present at 1000K. In other words, only few structures with total energy lying at the very left end of the distribution in Figure 4.1 can be formed, and interestingly, the Y atoms are near the GB core in all these structures. Therefore, the YSZ GB structure with the lowest energy was selected for studying the impurity segregation behavior using DFT calculations, see its local structures from different view angles in Figure 4.2
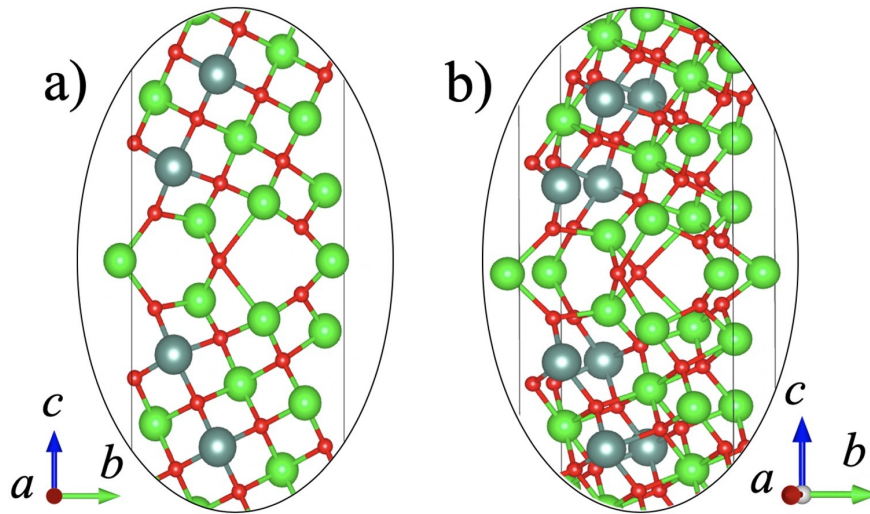
Figure 4.2: Schematic illustrations of local structures of YSZ GB from different view angles.

4.4   Conclusion

In summary, we have performed a statistical analysis of 7600 YSZ GB configurations from empirical-potential calculations. From vibrational and configurational antropy calculations of these microstates at 1000K, we determined that only states within about 0.02 eV above the lowest energy are present at 1000K. These states correspond to only a few structures with total energy lying at the lowest energy point of the total energy distribution. We found that these states contain Y atoms near the GB core. Knowing only these states are probably to exist, we were able to study the defect segregation tendencies in Σ 5 (310)/[001] YSZ GB structures.

Chapter 4, in part, is a reprint of the material as it appears in the Journal of the European Ceramic Society, 2019. Behtash, Mazier; Wong, Joseph; Jiang, Sicong; Luo, Jian; Yang, Kesong. Dr. Mazier Behtash was the primary investigator of this material.

Chapter 5

AIMSGB: Usage Introduction

5.1   Introduction

Grain boundaries are a type of interface that has importance in material properties. Of all possible grain boundaries, the coincidence site lattice (CSL) grain boundary has been the focus of research attention. The CSL grain boundary contains some atomic sites that coincide with sites of another grain, forming coincidence sites. These coincidence sites form a supercell called the CSL.

Given the rapid progress of high-throughput computational techniques and materials informatics, an algorithm to produce such CSL grain boundaries in a high-throughput fashion would be an invaluable asset to grain boundary research. In a previous paper, we provide such an algorithm to efficiently build a CSL grain boundary called aimsgb.[273] However, we did not provide practical instructions to apply aimsgb to real use cases. In this work, we strive to fill this gap by providing detailed documentation on the usage of the aimsgb algorithm.

5.2   Building Procedures

There are five macroscopic degrees of freedom (DOF) required to describe a grain boundary from crystallography. Three of them are represented by the rotation axis o (two DOFs) and the

rotation angle θ (one DOF). The remaining two describe the normal $\boldsymbol{n}$ to the grain boundary plane. The relative orientation between $\boldsymbol{o}$ and $\boldsymbol{n}$ determines the grain boundary type: tilt ($\boldsymbol{o} \perp \boldsymbol{n}$), twist ($\boldsymbol{o} \parallel \boldsymbol{n}$), and mixed grain boundaries. For our purposes, the necessary parameters can simply be extracted using `aimsgb list` or the `GBInformation` object in the aimsgb python module.

Aimsgb builds grain boundaries according to the following algorithm outline:

(1) Derive the rotation angle from a given rotation axis and Σ value.

(2) Create a rotation matrix from the rotation angle and rotation axis.

(3) Calculate the CSL matrix from the rotation matrix and Σ value.

(4) Use the CSL matrix to generate two grains, and combine them according to a given grain boundary plane, creating the grain boundary.

The theory behind this algorithm is discussed in greater depth in our previous paper.[273] The execution of this algorithm for grain boundary modeling can be performed via two approaches: (1) the command-line and (2) the aimsgb python module.

5.2.1   Command-line

The command-line is advantageous for quick and simple construction of a small number of grain boundary structures. Grain boundary structures can created following the general syntax: `aimsgb argument [-options]`. The argument that must be passed to aimsgb can be one of the following: (1) `list` and (2) `gb`

The `list` argument is used to generate a table of possible grain boundary parameters for a particular rotation axis, *uvw*. These parameters can be passed following the syntax: `aimsgb list rotation-axis [max_sigma]`. Figure 5.1 illustrates an example output table of `aimsgb list` which contains information regarding rotation angles, θ, grain boundary planes, and the CSL for each possible sigma value up to `max_sigma`. By default, `max_sigma` is set to 30, however a larger number can be specified to generate information for larger sigma values.

The gb argument is used to generate a file containing the lattice parameters and atomic coor-

```
Grain boundary information for rotation axis: 001
Show the sigma values up to 17 (Note: * means twist GB)
|  Sigma  |  Theta  | GB Plane    | CSL          |
|---------+---------+-------------+----------|
|    5    |  53.13  | (2 -1 0)    | 2   1   0    |
|         |         | (1  2 0)    | -1   2   0   |
|         |         | (0  0 1*)   | 0   0   1    |
|    5    |  36.87  | (3 -1 0)    | 3   1   0    |
|         |         | (1  3 0)    | -1   3   0   |
|         |         | (0  0 1*)   | 0   0   1    |
|   13    |  67.38  | (3 -2 0)    | 3   2   0    |
|         |         | (2  3 0)    | -2   3   0   |
|         |         | (0  0 1*)   | 0   0   1    |
|   13    |  22.62  | (5 -1 0)    | 5   1   0    |
|         |         | (1  5 0)    | -1   5   0   |
|         |         | (0  0 1*)   | 0   0   1    |
|   17    |  28.07  | (4  1 0)    | 4  -1   0    |
|         |         | (-1 4 0)    | 1   4   0    |
|         |         | (0  0 1*)   | 0   0   1    |
|   17    |  61.93  | (5  3 0)    | 5  -3   0    |
|         |         | (-3 5 0)    | 3   5   0    |
|         |         | (0  0 1*)   | 0   0   1    |
```

Figure 5.1: Grain boundary information table generated via `aimsgb list 001`.

dinates of a grain boundary structure. To generate the grain boundary structure, the rotation axis, sigma, grain boundary plane, and initial structure file must be passed to aimsgb following the form: `aimsgb gb rotation-axis sigma plane_h plane_k plane_l initial_structure [-options] [out]`. The grain boundary parameters can be obtained from the output of `aimsgb list` as shown in Figure 5.1. There are also optional arguments that can be passed to modify the grain boundary object, such as: (1) `ua` and `ub`, (2) `dl`, (3) `t`, (4) `ad`, and (5) `fmt`.

1. `ua` and `ub` specify the size in number of units of grain A and grain B respectively. Figure 5.2 illustrates the differences in a resulting structure when specifying `ua` and `ub`.

2. `dl` enables the deletion of grain A or B's top or bottom layers. The top and bottom layer of each grain can be removed following the format, `#b#t#b#t`, where the first `b` and `t` pair correspond to bottom and top layers of grain A respectively and the second pair to grain B. Figure 5.3 illustrates resulting structures when specifying varying values for `dl`.

3. `t` specifies the tolerance factor used to assign a structure's layers. Each layer corresponds to a unique plane along the grain boundary that is parallel to the grain boundary plane. Each of these layers contains all the atoms in the structure that are within a certain distance specified by the tolerance factor. By default, `t` is set to 0.25 Å. In most cases, the default value will suffice, however there are some cases when changing the tolerance is necessary as shown in Figure 5.4. In this structure, the atoms are slightly distorted from their original positions. When no layer-wise manipulations are performed, there is no difference in the resulting structure when the tolerance is changed (Figure 5.4a). However, when layer-wise manipulations are performed, such as layer deletion, a tolerance value that is too low will assign the distorted atoms to separate layers, resulting in the structure in Figure 5.4b. Increasing the tolerance to encompass the nearby atoms will assign the atoms to the correct layers as intended (Figure 5.4c). On the other hand, a tolerance value that is too large can yield unexpected results as in Figure 5.4d.
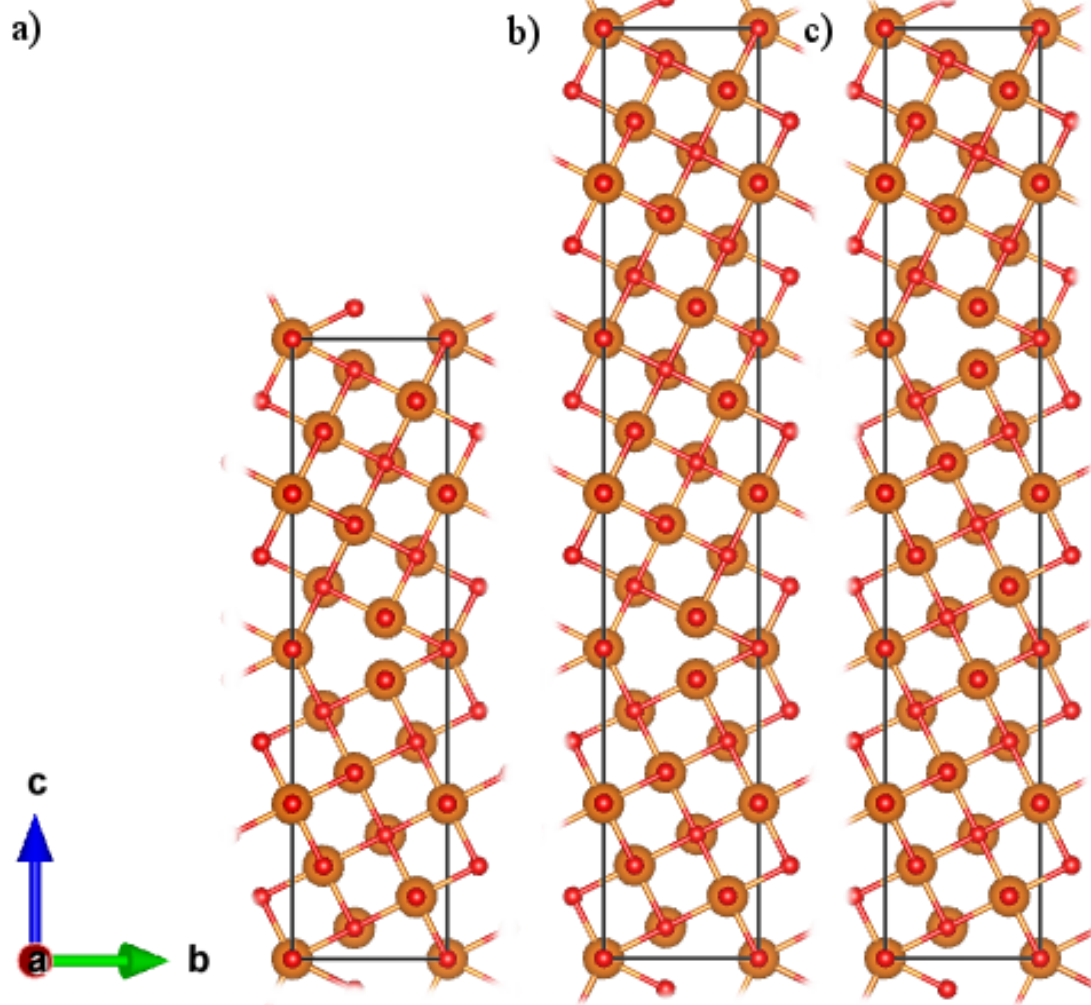
Figure 5.2: Grain boundaries generated using `aimsgb gb 001 5 1 2 0 POSCAR_mgo` a) `-ua 1 -ub 1`, b) `-ua 1 -ub 2`, and c) `-ua 2 -ub 1`.
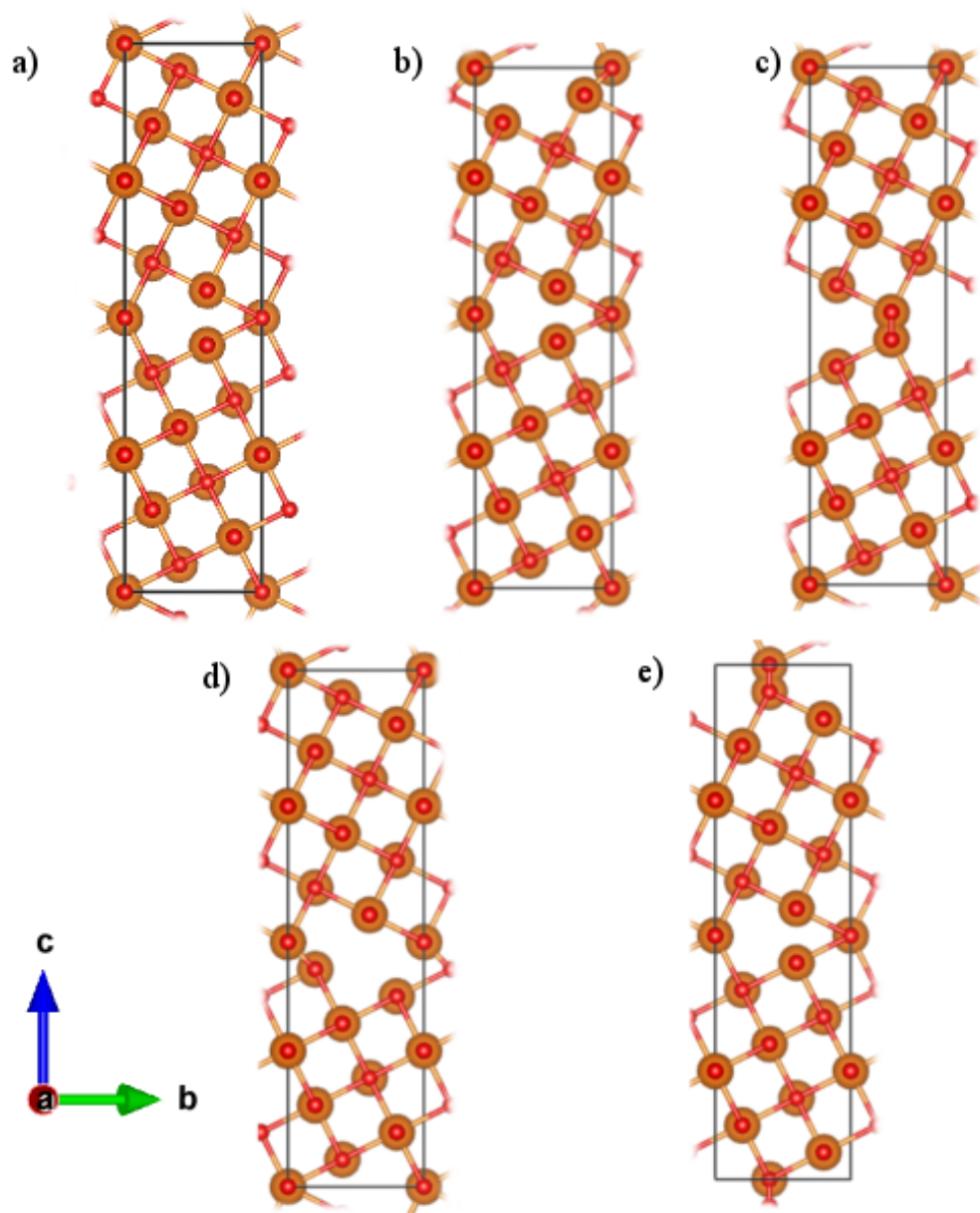
Figure 5.3: Grain boundaries with top or bottom layers removed using `aimsgb gb 001 5 1 2 0 POSCAR_mgo -dl` a) `0b0t0b0t` (default), b) `0b0t0b1t`, c) `0b0t1b0t`, d) `0b1t0b0t`, and e) `1b0t0b0t`.
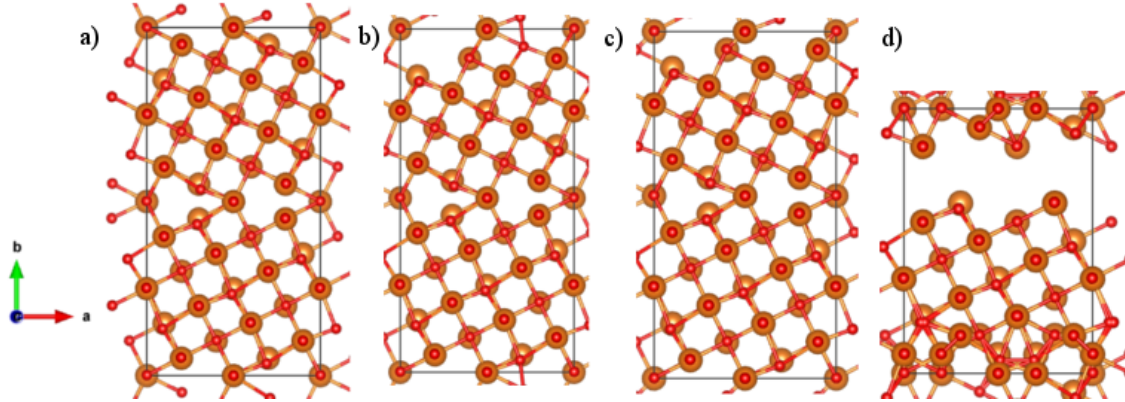
Figure 5.4: Slightly distorted grain boundaries with one top layer removed using various tolerance values. a) `-t 0.25` (no layer deletion performed), b) `-t 0.25 -dl 0b0t0b1t`, c) `-t 0.5 -dl 0b0t0b1t`, d) `-t 1.5 -dl 0b0t0b1t`

4. `ad` sets a vacuum thickness in angstroms between the grains at each interface as shown in Figure 5.5.

5. `fmt` sets the format for the output file. Possible formats include: poscar (default), cif, cssr, and json.

5.2.2   Python Module

The python module is useful if constructing a large number of grains or if integrating aimsgb with another software package. There are three classes defined by aimsgb: (1) the Grain class, (2) the GrainBoundary class, and (3) the GBInformation class.

The `Grain` class defines grain objects which inherit methods and properties of the `Structure` class from pymatgen. `Grain` objects can be created via several methods: `from_dict`, `from_file`, `from_magnetic_spacegroup`, `from_sites`, `from_spacegroup`, and `from_str`. These methods are documented in detail in pymatgen's `Structure` module. `Grain` objects also contain several additional methods which facilitate grain boundary construction: (1) `make_supercell`, (2) `delete_bt_layer`, (3) `sort_sites_in_layers`, and (4) `build_grains`.

1. The `make_supercell` method is similar to pymatgen's `Structure.make_supercell`, how-
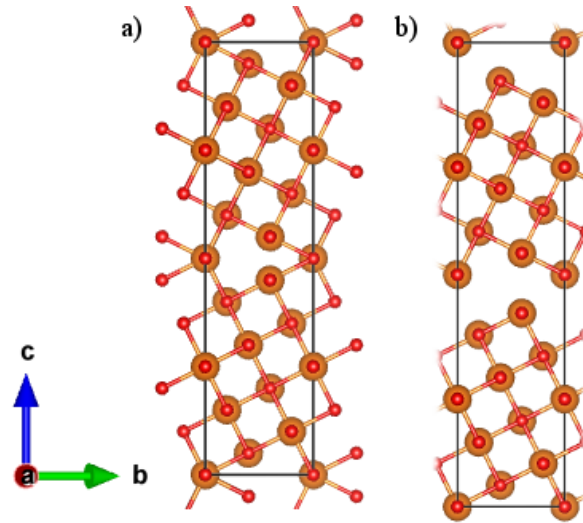
Figure 5.5: Grain boundaries generated while specifying the interface distance according to `aimsgb gb 001 5 1 2 0 POSCAR_mgo`. a) `-ad 0` (default) and b) `-ad 0.75`

ever the aimsgb version takes extra precaution to ensure the fractional coordinates and lattice parameters are compatible for grain boundary construction. Like the pymatgen version, it takes one argument, a scaling matrix in the form of a) a 3x3 scaling matrix defining linear combinations of the original lattice vectors, (b) a list of 3 scaling factors, or (c) a number by which to scale all lattice vectors.

2. The `delete_bt_layer` method deletes the bottom or top layer of the grain. `delete_bt_layer` takes one required and two optional arguments: `bt`, `tol`, and `axis`. `bt` can be the character, "t" or "b", referring to the top or bottom layer of the grain. `tol` refers to the tolerance used to assign layers (default = 0.25 angstroms). `axis` refers to the direction along which to count the layers. The direction can be set to 0 (x), 1 (y), or 2 (z, default). Typically, the normal to the grain boundary is passed for the axis. The normal to the grain boundary can be obtained from a grain boundary object's `gb_direction` attribute.

3. The `sort_sites_in_layers` method takes two optional arguments: `tol` and `axis`. `tol` is the tolerance used to assign layers (default = 0.25 angstroms). `axis` refers to the direction along which to count the layers. Generally, the normal to the grain boundary is passed for

the axis. The normal to the grain boundary can be obtained from a grain boundary object's `gb_direction` attribute.

4. The `build_grains` method constructs and returns the two grains of a grain boundary by using the given CSL and the object as an initial structure. `build_grains` takes two required arguments and two optional arguments: `csl`, `gb_direction`, `uc_a`, and `uc_b`. The `csl` can be obtained manually from `aimsgb list` or from the `GBInformation.get_gb_info` method.

The `GrainBoundary` class defines an object containing all the grain boundary parameters and `Grain` objects necessary for grain boundary construction. `GrainBoundary` objects can be created following the format, `GrainBoundary(axis, sigma, plane, initial_structure)`. Once a `GrainBoundary` is created, the grain boundary parameters can be extracted following the format, `GrainBoundary_object.property`, where `property` can be one of the following: (1) `rot_matrix`, (2) `theta`, (3) `csl`, (4) `grain_a`, or `grain_b`. Besides the grain boundary properties, the `GrainBoundary` class defines one method: (5) build_gb.

1. The `rot_matrix` refers to the rotation matrix used to calculate the coincidence site matrix.

2. The `theta` refers to the rotation angle used to determine the rotation matrix.

3. The `csl` refers to the CSL matrix.

4. The `grain_a` and `grain_b` attributes correspond to the two grain objects used to construct the grain boundary structure.

5. The `build_gb` method constructs and returns the grain boundary structure as a grain object. It takes several optional arguments which perform additional operations on the grain boundary structure, including: `add_if_dist`, `delete_layer`, and `tol`. These arguments are passed in the same format as their counterparts in the command-line version of aimsgb.

94
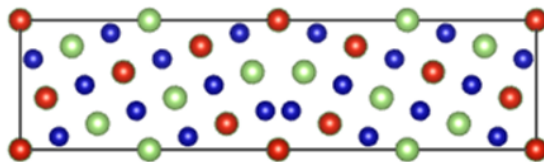
Figure 5.6: The simplest example of building a grain boundary from a poscar file.

5.2.3 The GBInformation class

The `GBInformation` class is useful for extracting grain boundary information automatically, with minimal intervention by the user. `GBInformation` objects can be instantiated by passing the rotation axis and max sigma value following the form, `GBInformation(axis, sigma, specific=bool)`. A bool for `specific` can be passed to specify if the grain boundary information generated is for one specific sigma value or all sigma values up to `max_sigma`. By default, `specific` is set to `False`. There is one primary method that is defined by the GBInformation class that is used to extract grain boundary information: (1) `get_gb_info`.

1. The `get_gb_info` returns all the information on sigma, rotation angle, grain boundary planes, and CSL matrix in the form of a dictionary of dictionaries, where each key corresponds to a sigma value and each value corresponds to the rotation angle, grain boundary planes, and CSL for a particular sigma value.

All the classes defined by aimsgb can be imported via `from aimsgb import *`. The Lattice module from pymatgen will also be used to modify lattice parameters in some examples. Figure 5.6 shows the simplest method to build a grain boundary structure. The grain boundary parameters are used to instantiate a `GrainBoundary` object. The `build_gb` method constructs the grain boundary and returns it as a `Grain` object and the `to` method of the `Grain` object writes the `grain` object to a file named "`POSCAR`".

95

```
initial_struct = Grain.from_file(poscar)
axis = [0,0,1]

#find all possible sigma values with respective gb info and store them in a dict
info = {}
for sigma in range(3,30,2):
    try:
        info.update(GBInformation(axis, sigma, specific=True))
    except ValueError:
        pass

#loop through all sigma info in order of increasing theta angle, building gb with each sigma value pair
stp = {}
for sigma, value in sorted(info.iteritems(), key=lambda (s,v): min(v['theta'])):
    stp['sigma'] = sigma
    stp['theta'] = min(value['theta'])
    theta_index = value['theta'].index(min(value['theta'])) #used to get a plane corresponding to the smallest theta
    stp['plane'] = value['plane'][theta_index][0]
    gb = GrainBoundary(axis, stp['sigma'], stp['plane'], initial_struct)
    gb.build_gb(to_primitive=False).to(filename=poscar+"_gb{0:.2f}.vasp".format(stp['theta']), fmt="poscar")
    print poscar + " grain boundary written to " + poscar+"_gb{0:.2f}.vasp".format(stp['theta'])
```
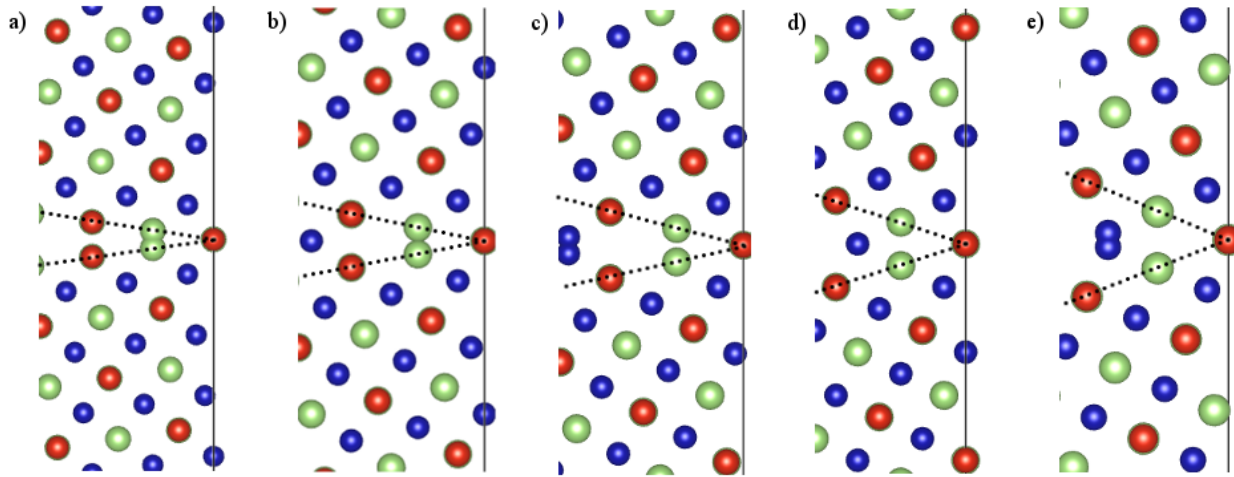

Figure 5.7: Build grain boundaries in order of increasing θ using the GBInformation class: a) 16.26°, b) 22.62°, c) 28.07°, d) 36.87°, and e) 43.6°

Figure 5.7 demonstrates the usage of the GBInformation class to generate grain boundaries in the order of increasing θ. GBInformation objects are created for Σ values 3-30 and stored in a dictionary. This dictionary is looped through in order of the smaller θ value for each Σ. In each loop, the grain boundary parameters are extracted and used to construct a grain boundary object which is then written to a file.

Figure 5.8 demonstrates a method to progressively increase the number of layer deletions performed on a grain boundary structure. The string for the delete_layer argument in build_gb is updated with a larger number with each loop. A GrainBoundary object is created and the interlayer distance is stored to keep the two grains from moving closer together with each layer

```
axis = [0,0,1]
sigma = 25
plane = [1,7,0]
initial_struct = Grain.from_file(poscar)

#build gb, but with increasing number of layer deletions
for i in range(0,5):
    delete = "0b{}t0b{}t".format(i, i)
    gb = GrainBoundary(axis, sigma, plane, initial_struct)
    ind = gb.gb_direction              #the direction normal to the grain boundary plane
    layers = gb.grain_a.sort_sites_in_layers(tol=0.05, axis=ind)
    l_dist = abs(layers[0][0].coords[ind] - layers[1][0].coords[ind])    #distance between layers

    #delete layers, but dont move the grains closer together after deletion
    gb.build_gb(delete_layer=delete, add_if_dist=l_dist*i).to(filename="POSCAR_"+delete, fmt="poscar")
    print poscar + " grain boundary written to " + "POSCAR_"+delete
```
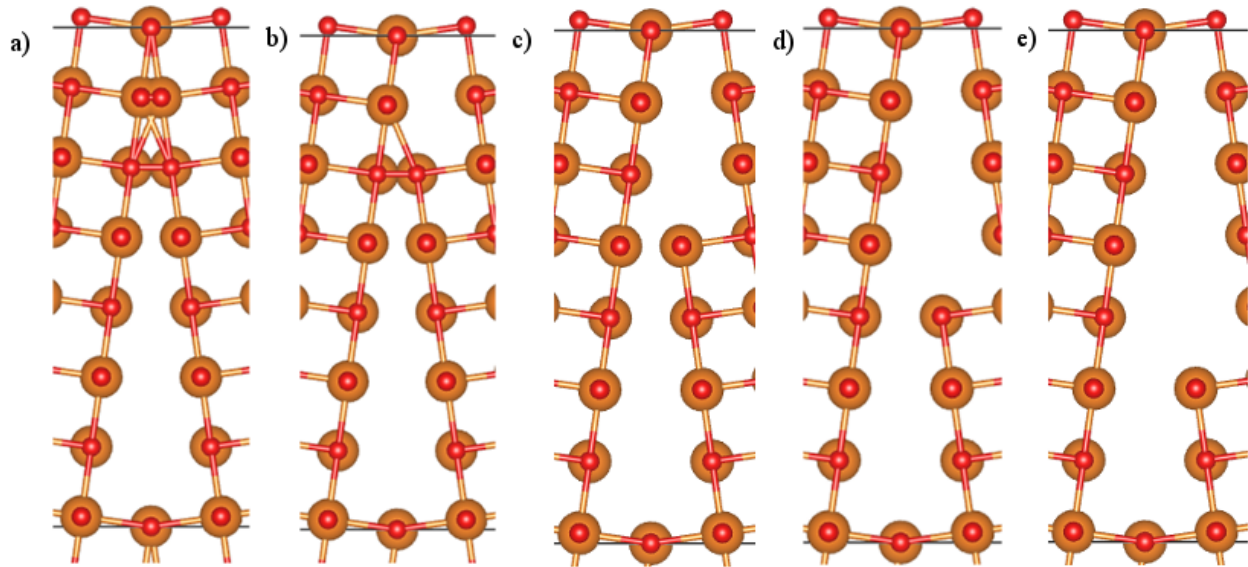

Figure 5.8: Generate grain boundaries with an increasing number of layer deletions to remove atoms that are too close together: a) 0b0t0b0t, b) 0b1t0b1t, c) 0b2t0b2t, d) 0b3t0b3t, e) 0b4t0b4t.

deletion. The `delete` string and the interlayer distance are passed to the `build_gb` method to construct the grain boundary and write it to a file. This method is particularly useful for comparing the results of different layer deletions if the number of layer deletions required is not immediately obvious.

Figure 5.9 demonstrates the construction of a mixed grain boundary. First, supercells of tilt and twist grain boundaries are created in preparation for their combination. Next, the lattice parameters of both supercell `Grain` objects and their fractional coordinates are updated. Once the lattice parameters and fractional coordinates are compatible, the two grains are combined to form a new `Grain` object containing the mixed grain boundary structure which is then written to a file.

97

```
axis = [0,0,1]
sigma = 5
initial_struct = Grain.from_file(poscar)

#make supercells of tilt and twist grain boundaries in preparation for combining
gb_tilt = GrainBoundary(axis, sigma, [1,2,0], initial_struct)
gb_twist = GrainBoundary(axis, sigma, [0,0,1], initial_struct)
grain_tilt = Grain.from_sites(gb_tilt.build_gb(to_primitive=False)[:]) #converts gb object into grain
grain_tilt.make_supercell([1,1,2])
grain_twist = Grain.from_sites(gb_twist.build_gb(to_primitive=False)[:])
grain_twist.make_supercell([1,2,1])

#change lattice lengths and update fcoords
abc_tilt = list(grain_tilt.lattice.abc)
abc_twist, angles = list(grain_twist.lattice.lengths_and_angles)
abc_tilt[0] += abc_twist[0]          #increase lattice to fit both grains
new_lat = Lattice.from_lengths_and_angles(abc_tilt, angles)
twist_fcoords = new_lat.get_fractional_coords(
    grain_twist.cart_coords + [grain_tilt.lattice.abc[0],0,0])  #update fcoords
tilt_fcoords = new_lat.get_fractional_coords(grain_tilt.cart_coords)     #update fcoords
grain_tilt = Grain(new_lat, grain_tilt.species, tilt_fcoords)   #update grain info
grain_twist = Grain(new_lat, grain_twist.species, twist_fcoords)#update grain info

#combine both grains into mixed grain
grain_mixed = Grain.from_sites(grain_tilt[:] + grain_twist[:])
grain_mixed = grain_mixed.get_sorted_structure()

#write grain to file
grain_mixed.to(filename="grain_mixed.vasp",fmt="poscar")
print poscar + " mixed grain boundary written to " + "grain_mixed.vasp"
```
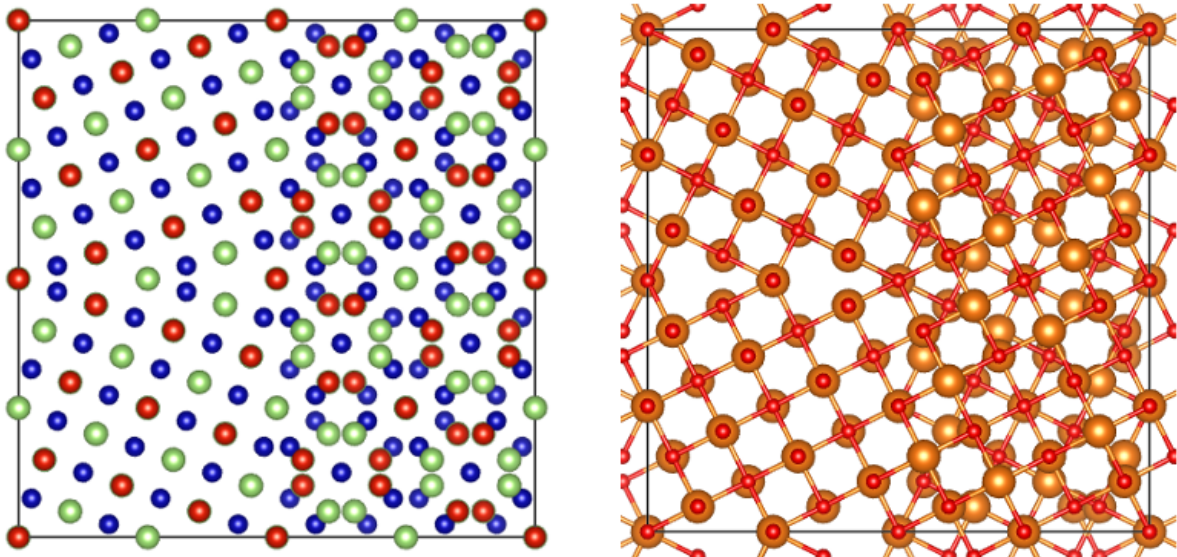

Figure 5.9: Building a mixed grain boundary by combining two grain boundary structures.

5.3 Example Applications

5.3.1 Asymmetric MgO grain boundary

McKenna and Shluger performed first principles calculations of defects near a grain boundary in MgO.[6] Their initial grain boundary structure is shown in Figure 5.10a. This structure can easily be replicated using aimsgb. As an initial starting point, a structure can be generated from the command line, via `aimsgb gb 001 5 3 -1 0 POSCAR_mgo`. From this initial structure shown in Figure 5.10b, it can be seen that the interface does not match that of Figure 5.10a. Upon inspection of the starting structure, it can be seen that 9 layers must be removed to create the correct interface termination. In addition to the layer deletion, further operations must be performed to obtain the asymmetric Mg/O interface. Namely, the Mg and O atoms must be switched in one of the grains to create the asymmetric interface. These operations can be performed via the aimsgb python module as shown in Figure 5.10 (top). The species are switched by reassigning the specie name for each atom. The indexes for the Mg and O atoms can be seen by printing the `grain_b` attribute of the `GrainBoundary` object. By performing these operations and adding an interface separation distance, a structure identical to that of McKenna and Shluger is generated as shown in Figure 5.10c.

5.3.2 Dopants at hybrid perovskite grain boundary

Long *et al.* performed time-domain atomistic simulations of grain boundaries in the hybrid perovskite, $CH_3NH_3PbI_3$ ($MAPbI_3$).[7] Their initial grain boundary structures after relaxation are shown in Figure 5.11. These structures can be replicated using aimsgb. A starting structure can be generated via `aimsgb 001 5 1 2 0 POSCAR_MAPbI3`. From this structure (Figure 5.12a), it can be seen that the interface does not match that of Figure 5.11b. Because the number of layer deletions required to replicate the interface is not immediately obvious, a series of structures with varying layer deletions must be compared. This can be accomplished with the aimsgb python script shown

```
#grain boundary info
axis = [0,0,1]
sigma = 5
plane = [3,-1,0]
initial_struct = Grain.from_file(poscar)
gb = GrainBoundary(axis, sigma, plane, initial_struct)

#switch Mg atoms to O in one grain
b = gb.grain_b
b[40:] = "Mg"
b[0:40] = "O"

#delete layers to reach correct termination, then add appropriate interface distance
gb.build_gb(delete_layer="0b9t0b9t", add_if_dist=1.44034).to(filename="POSCAR", fmt="poscar")
```
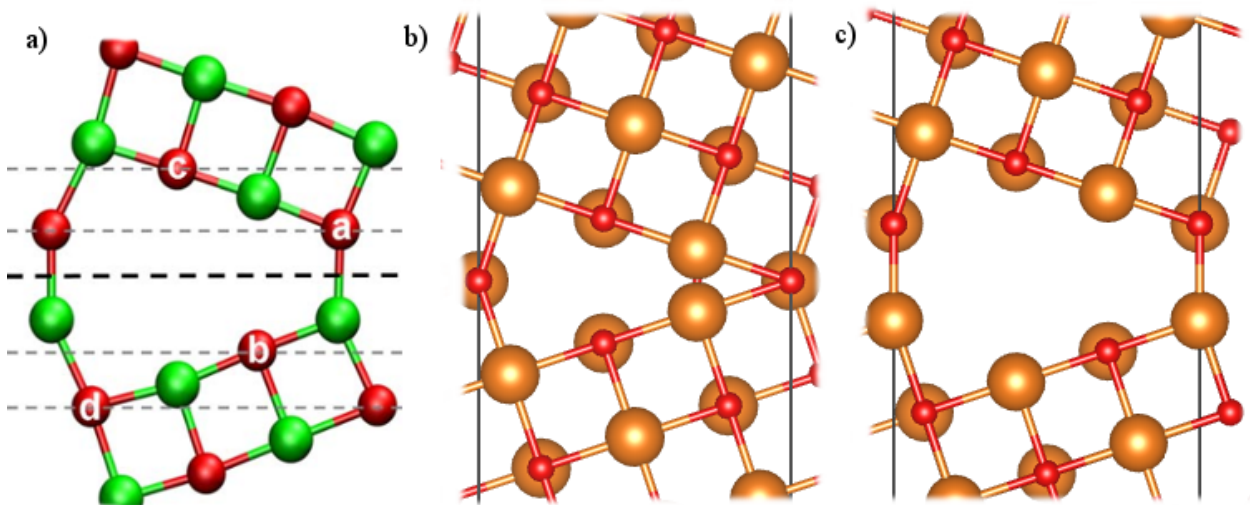

Figure 5.10: a) The (310)[001] tilt grain boundary by McKenna and Shluger, b) structure generated from `aimsgb gb 001 5 3 -1 0 POSCAR_mgo`, c) identical grain boundary structure generated from aimsgb script. Adapted and reproduced with permission from [6].
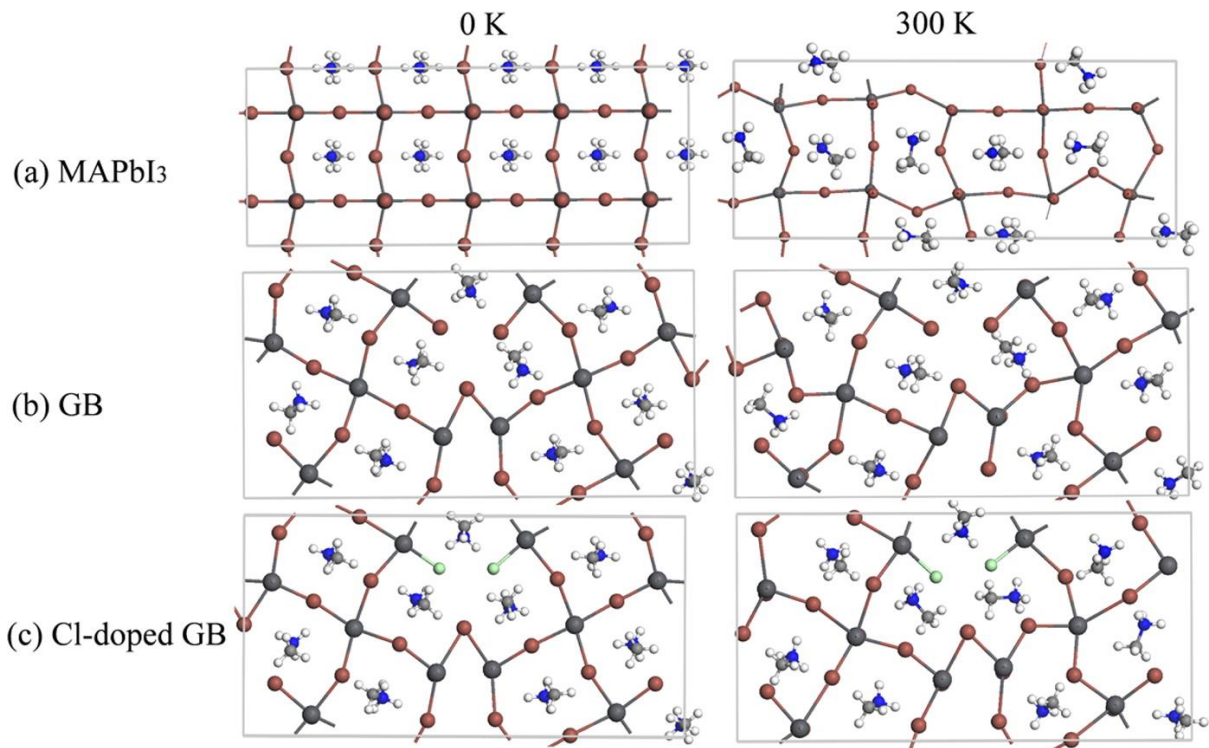
Figure 5.11: a) bulk MAPbI$_3$, b) Σ5 (012) grain boundary, c) Cl-doped grain boundary. Reproduced and adapted with permission from [7].

in Figure 5.12 (top). A comparison of these structures identifies 3 top and bottom layer deletions of both grains is necessary to obtain an interface similar to that of Long *et al.* as shown in Figure 5.12b. However, this structure has incorrect positions for the atoms in the MA molecule at the interface. To correct this molecule, the molecule at the interface is deleted and the atoms belonging to a molecule within the grain containing the same xy coordinates are copied to the interface. This operation yields the structure shown in Figure 5.10c, an analogous replica of the grain boundary structure by Long *et al.*. In addition, two I atoms at the interface can be replaced with Cl to recreate the Cl-doped structure shown in Figure 5.11c.

```
axis = [0,0,1]
sigma = 5
plane = [1,2,0]
initial_struct = Grain.from_file(poscar)

for i in range(0,7):
    delete = "{}b{}t{}b{}t".format(i, i, i, i)
    gb = GrainBoundary(axis, sigma, plane, initial_struct, uc_a=2, uc_b=2)
    gb.build_gb(delete_layer=delete).to(filename="POSCAR_"+delete, fmt="poscar")

    print poscar + " grain boundary written to " + "POSCAR_"+delete
```
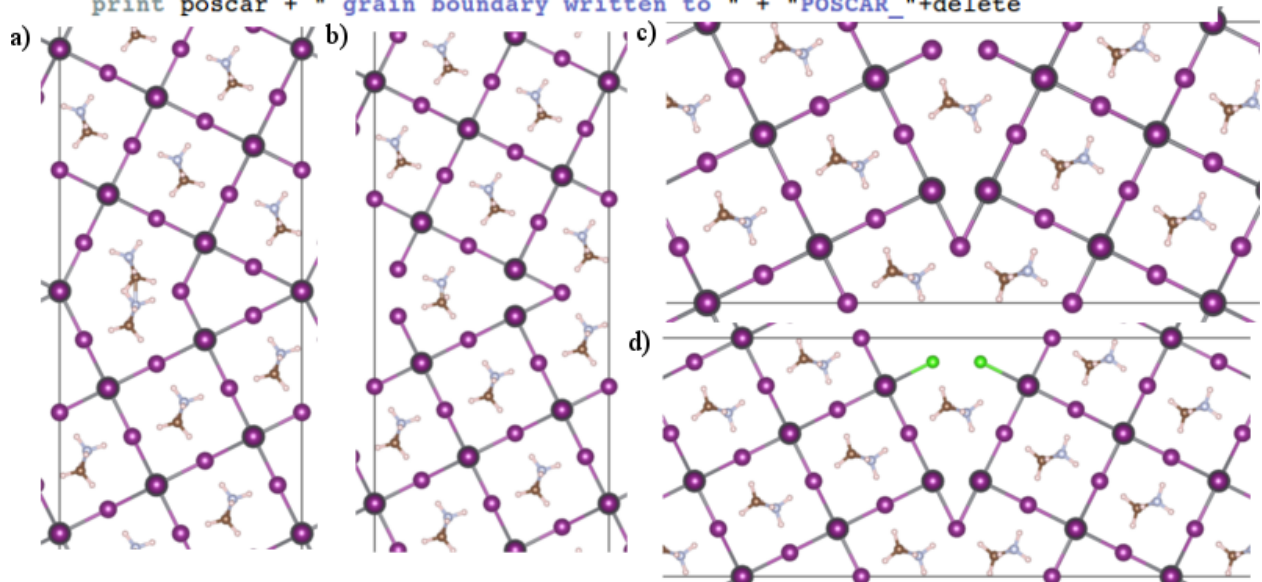

Figure 5.12: Hybrid perovskite grain boundaries generated using aimsgb: a) `aimsgb gb 001 5 1 2 0 POSCAR_MAPbI3` b) `-dl 3b3t3b3t` c) MA cation deleted at the interface and replaced with a MA cation translated from `grain_b` d) 2 I atoms replaced with Cl at the interface.

5.4 Conclusion

Aimsgb is an open-source python package that enables quick and facile construction of grain boundary structures for first principles calculations via the command-line or through the python module. Its basis in the pymatgen Structure module enables total control of atomic coordinates and lattice parameters, allowing the construction of virtually any grain boundary structure. The source code, additional examples, and a web application are publically available at aimsgb.org.

Chapter 5, in full, is currently being prepared for submission for publication of the material. Wong, Joseph; Cheng, Jianli; Yang, Kesong. The thesis author was the primary investigator and author of this material.

Bibliography

[1] Weiwei Liu, Jun Xing, Jiaxin Zhao, Xinglin Wen, Kai Wang, Peixiang Lu, and Qihua Xiong. Giant two–photon absorption and its saturation in 2d organic–inorganic perovskite. *Adv. Opt. Mater.*, 5:1601045, 2017.

[2] Lingling Mao, Weijun Ke, Laurent Pedesseau, Yilei Wu, Claudine Katan, Jacky Even, Michael R. Wasielewski, Constantinos C. Stoumpos, and Mercouri G. Kanatzidis. Hybrid dion–jacobson 2d lead iodide perovskites. *J. Am. Chem. Soc.*, 140:3775–3783, 2018.

[3] Olga Nazarenko, Martin R. Kotyrba, Sergii Yakunin, Marcel Aebli, Gabriele Rainó, Bogdan M. Benin, Michael Wörle, and Maksym V. Kovalenko. Guanidinium-formamidinium lead iodide: A layered perovskite-related compound with red luminescence at room temperature. *J. Am. Chem. Soc.*, 140:3850–3853, 2018.

[4] Duyen H. Cao, Constantinos C. Stoumpos, Omar K. Farha, Joseph T. Hupp, and Mercouri G. Kanatzidis. 2d homologous perovskites as light-absorbing materials for solar cell applications. *J. Am. Chem. Soc.*, 137:7843–7850, 2015.

[5] J.-C. Blancon, H. Tsai, W. Nie, C. C. Stoumpos, L. Pedesseau, C. Katan, M. Kepenekian, C. M. M. Soe, K. Appavoo, M. Y. Sfeir, S. Tretiak, P. M. Ajayan, M. G. Kanatzidis, J. Even, J. J. Crochet, and A. D. Mohite. Extremely efficient internal exciton dissociation through edge states in layered 2d perovskites. *Science*, 355:1288–1292, 2017.

[6] KP McKenna and AL Shluger. First-principles calculations of defects near a grain boundary in mgo. *Phys. Rev. B*, 79:224116, 2009.

[7] Run Long, Jin Liu, and Oleg V Prezhdo. Unravelling the effects of grain boundary and chemical doping on electron–hole recombination in $CH_3NH_3PbI_3$ perovskite by time-domain atomistic simulation. *J. Am. Chem. Soc.*, 138:3884–3890, 2016.

[8] I. Galanakis, P. H. Dederichs, and N. Papanikolaou. Slater-pauling behavior and origin of the half-metallicity of the full-heusler alloys. *Phys. Rev. B*, 66:174429, 2002.

[9] G. W. Hull, J. H. Wernick, T. H. Geballe, J. V. Waszczak, and J. E. Bernardini. Superconductivity in the ternary intermetallics $YbPd_2Ge_2$, $LaPd_2Ge_2$, and $LaPt_2Ge_2$. *Phys. Rev. B*, 24:6715–6718, 1981.

[10] H. A. Kierstead, B. D. Dunlap, S. K. Malik, A. M. Umarji, and G. K. Shenoy. Coexistence of ordered magnetism and superconductivity in Pd_2YbSn. *Phys. Rev. B*, 32:135–138, 1985.

[11] Stanislav Chadov, Xiaoliang Qi, Jürgen Kübler, Gerhard H. Fecher, Claudia Felser, and Shou Cheng Zhang. Tunable multifunctional topological insulators in ternary heusler compounds. *Nat. Mater.*, 9:541–545, 2010.

[12] Hsin Lin, L. Andrew Wray, Yuqi Xia, Suyang Xu, Shuang Jia, Robert J. Cava, Arun Bansil, and M. Zahid Hasan. Half-heusler ternary compounds as new multifunctional experimental platforms for topological quantum phenomena. *Nat. Mater.*, 9:546–549, 2010.

[13] Marcel Franz. Starting a new family. *Nat. Mater.*, 9:536–537, 2010.

[14] H. van Leuken and R. A. de Groot. Half-metallic antiferromagnets. *Phys. Rev. Lett.*, 74:1171–1173, 1995.

[15] Benjamin Balke, Gerhard H. Fecher, JÃijrgen Winterlik, and Claudia Felser. Mn3ga, a compensated ferrimagnet with high curie temperature and low magnetic moment for spin torque transfer applications. *Appl. Phys. Lett.*, 90:152504, 2007.

[16] Jürgen Winterlik, Benjamin Balke, Gerhard H. Fecher, Claudia Felser, Maria C. M. Alves, Fabiano Bernardi, and Jonder Morais. Structural, electronic, and magnetic properties of tetragonal $Mn_{3-x}Ga$: Experiments and first-principles calculations. *Phys. Rev. B*, 77:054406, 2008.

[17] H. Kurt, K. Rode, M. Venkatesan, P. Stamenov, and J. M. D. Coey. High spin polarization in epitaxial films of ferrimagnetic mn3ga. *Phys. Rev. B*, 83:020405, 2011.

[18] T. Block, C. Felser, G. Jakob, J. Ensling, B. MÃijhling, P. GÃijtlich, and R.J. Cava. Large negative magnetoresistance effects in $Co_2Cr_{0.6}Fe_{0.4}Al$. *J. Solid State Chem.*, 176:646–651, 2003.

[19] Benjamin Balke, Gerhard H. Fecher, Hem C. Kandpal, Claudia Felser, Keisuke Kobayashi, Eiji Ikenaga, Jung-Jin Kim, and Shigenori Ueda. Properties of the quaternary half-metal-type heusler alloy $Co_2Mn_{1-x}Fe_xSi$. *Phys. Rev. B*, 74:104405, 2006.

[20] S Fujii, S Sugimura, Ishida, and S Asano. Hyperfine fields and electronic structures of the heusler alloys Co_2MnX (X=Al, Ga, Si, Ge, Sn). *J. Phys.: Condens. Matter*, 2:8583, 1990.

[21] Ming Zhang, Zhuhong Liu, Haining Hu, Guodong Liu, Yuting Cui, Jinglan Chen, Guangheng Wu, Xixiang Zhang, and Gang Xiao. Is heusler compound co2cral a half-metallic ferromagnet: Electronic band structure, and transport properties. *J. Magn. Magn. Mater.*, 277:130–135, 2004.

[22] Atsufumi Hirohata and Koki Takanashi. Future perspectives for spintronic devices. *J. Phys. D: Appl. Phys.*, 47:193001, 2014.

[23] M Oogane, T Kubota, H Naganuma, and Y Ando. Magnetic damping constant in co-based full heusler alloy epitaxial films. *J. Phys. D: Appl. Phys.*, 48:164012, 2015.

[24] C. Felser, V. Alijani, J. Winterlik, S. Chadov, and A. K. Nayak. Tetragonal heusler compounds for spintronics. *IEEE Trans. Magn.*, 49:682–685, 2013.

[25] Teuta Gasi, Ajaya K. Nayak, Jürgen Winterlik, Vadim Ksenofontov, Peter Adler, Michael Nicklas, and Claudia Felser. Exchange-spring like magnetic behavior of the tetragonal heusler compound Mn_2FeGa as a candidate for spin-transfer torque. *Appl. Phys. Lett.*, 102:202402, 2013.

[26] Yoshio Miura, Masafumi Shirai, and Kazutaka Nagao. Ab initio study on stability of half-metallic co-based full-heusler alloys. *J. Appl. Phys.*, 99:08J112, 2006.

[27] Zhenchao Wen, Hiroaki Sukegawa, Seiji Mitani, and Koichiro Inomata. Perpendicular magnetization of co2feal full-heusler alloy films induced by mgo interface. *Appl. Phys. Lett.*, 98:242507, 2011.

[28] Takao Marukame and Masafumi Yamamoto. Tunnel magnetoresistance in fully epitaxial magnetic tunnel junctions with a full-heusler alloy thin film of $Co_2Cr_{0.6}Fe_{0.4}Al$ and a mgo tunnel barrier. *J. Appl. Phys.*, 101:083906, 2007.

[29] Jiangling Pan, Jun Ni, and Bingchu Yang. Surface structures of $Co_2FeAl_{0.5}Si_{0.5}(001)$ heusler alloys: A first-principles study. *Physica B*, 405:1580–1585, 2010.

[30] I. Galanakis. Effect of surfaces and interfaces on the electronic, magnetic and gap-related properties of the half-metal Co_2MnSn. *J. Comput. Theor. Nanos.*, 7:474–478, 2010.

[31] I Galanakis. Surface properties of the half-and full-heusler alloys. *J. Phys.: Condens. Matter*, 14:6329, 2002.

[32] S. Javad Hashemifar, Peter Kratzer, and Matthias Scheffler. Preserving the half-metallicity at the heusler alloy co2MnSi(001) surface: A density functional theory study. *Phys. Rev. Lett.*, 94:096402, 2005.

[33] M Oogane, Y Sakuraba, J Nakata, H Kubota, Y Ando, A Sakuma, and T Miyazaki. Large tunnel magnetoresistance in magnetic tunnel junctions using Co_2MnX (x = al, si) heusler alloys. *J. Phys. D: Appl. Phys.*, 39:834, 2006.

[34] Sh. Khosravizadeh, S. Javad Hashemifar, and Hadi Akbarzadeh. First-principles study of the co2FeSi(001) surface and co2FeSi/GaAs(001) interface. *Phys. Rev. B*, 79:235203, 2009.

[35] Hongpei Han, G. Y. Gao, and K. L. Yao. First-principles study on the half-metallicity of full-heusler alloy Co_2VGa (111) surface. *J. Appl. Phys.*, 111:093730, 2012.

[36] Jincheng Li and Yingjiu Jin. Half-metallicity of the inverse heusler alloy $Mn_2CoAl(001)$ surface: A first-principles study. *Appl. Sur. Sci.*, 283:876–880, 2013.

[37] G. Kresse and J. Furthmuller. Efficient iterative schemes for *ab-initio* total-energy calculations using a plane-wave basis set. *Phys. Rev. B*, 54:11169–11186, 1996.

[38] G. Kresse and D. Joubert. From ultrasoft pseudopotentials to the projector augmented-wave method. *Phys. Rev. B*, 59:1758–1775, 1999.

[39] P. E. Blöchl. Projector augmented-wave method. *Phys. Rev. B*, 50:17953–17979, 1994.

[40] J. P. Perdew, K. Burke, and M. Ernzerhof. Generalized gradient approximation made simple. *Phys. Rev. Lett.*, 77:3865–3868, 1996.

[41] S. Curtarolo, W. Setyawan, G. L. W. Hart, M. Jahnatek, R. V. Chepulskii, R. H. Taylor, S. Wang, J. Xue, K. Yang, O. Levy, M. Mehl, H. T. Stokes, D. O. Demchenko, , and D. Morgan. AFLOW: an automatic framework for high-throughput materials discovery. *Comput. Mater. Sci.*, 58:218–226, 2012.

[42] T. Kanomata, Y. Chieda, K. Endo, H. Okada, M. Nagasako, K. Kobayashi, R. Kainuma, R. Y. Umetsu, H. Takahashi, Y. Furutani, H. Nishihara, K. Abe, Y. Miura, and M. Shirai. Magnetic properties of the half-metallic heusler alloys Co_2VAl and Co_2VGa under pressure. *Phys. Rev. B*, 82:144415, 2010.

[43] Sabine Wurmehl, Gerhard H. Fecher, Hem C. Kandpal, Vadim Ksenofontov, Claudia Felser, Hong-Ji Lin, and Jonder Morais. Geometric, electronic, and magnetic structure of Co_2FeSi: Curie temperature and magnetic moment measurements and calculations. *Phys. Rev. B*, 72:184434, 2005.

[44] Shyue Ping Ong, William Davidson Richards, Anubhav Jain, Geoffroy Hautier, Michael Kocher, Shreyas Cholia, Dan Gunter, Vincent L. Chevrier, Kristin A. Persson, and Gerbrand Ceder. Python materials genomics (pymatgen): A robust, open-source python library for materials analysis. *Comput. Mater. Sci.*, 68:314–319, 2013.

[45] Richard Tran, Zihan Xu, Balachandran Radhakrishnan, Donald Winston, Wenhao Sun, Kristin A. Persson, and Shyue Ping Ong. Surface energies of elemental crystals. *Scientific Data*, 3:160080, 2016.

[46] Wenhao Sun and Gerbrand Ceder. Efficient creation and convergence of surface slabs. *Surf. Sci.*, 617:53–59, 2013.

[47] Stefano Sanvito, Corey Oses, Junkai Xue, Anurag Tiwari, Mario Zic, Thomas Archer, Pelin Tozman, Munuswamy Venkatesan, Michael Coey, and Stefano Curtarolo. Accelerated discovery of new magnets in the heusler alloy family. *Sci. Adv.*, 3:e1602241, 2017.

[48] K. Refson, R. A. Wogelius, D. G. Fraser, M. C. Payne, M. H. Lee, and V. Milman. Water chemisorption and reconstruction of the mgo surface. *Phys. Rev. B*, 52:10823–10826, 1995.

[49] T.A. Roth. The surface and grain boundary energies of iron, cobalt and nickel. *Mater. Sci. Eng.*, 18:183–192, 1975.

[50] Stefano Curtarolo, Gus L. W. Hart, Marco Buongiorno Nardelli, Natalio Mingo, Stefano Sanvito, and Ohad Levy. The high-throughput highway to computational materials design. *Nat. Mater.*, 12:191–201, 2013.

[51] Jeff Greeley, Thomas F. Jaramillo, Jacob Bonde, Ib Chorkendorff, and Jens K. Norskov. Computational high-throughput screening of electrocatalytic materials for hydrogen evolution. *Nat. Mater.*, 5:909–913, 2006.

[52] Jürgen Hafner. Ab-initio simulations of materials using vasp: Density-functional theory and beyond. *J. Comput. Chem.*, 29:2044–2078, 2008.

[53] S. Curtarolo, W. Setyawan, S. Wang, J. Xue, K. Yang, R. H. Taylor, L. J. Nelson, G. L. W. Hart, S. Sanvito, M. Buongiorno Nardelli, N. Mingo, and O. Levy. AFLOWLIB.ORG: A distributed materials properties repository from high-throughput *ab Initio* calculations. *Comput. Mater. Sci.*, 58:227–235, 2012.

[54] Anubhav Jain, Shyue Ping Ong, Geoffroy Hautier, Wei Chen, William Davidson Richards, Stephen Dacek, Shreyas Cholia, Dan Gunter, David Skinner, Gerbrand Ceder, and Kristin A. Persson. Commentary: The materials project: A materials genome approach to accelerating materials innovation. *APL Mater.*, 1:011002, 2013.

[55] Ghanshyam Pilania, Chenchen Wang, Xun Jiang, Sanguthevar Rajasekaran, and Ramamurthy Ramprasad. Accelerating materials property predictions using machine learning. *Sci. Rep.*, 3:2810, 2013.

[56] Paul Raccuglia, Katherine C. Elbert, Philip D. F. Adler, Casey Falk, Malia B. Wenny, Aurelio Mollo, Matthias Zeller, Sorelle A. Friedler, Joshua Schrier, and Alexander J. Norquist. Machine-learning-assisted materials discovery using failed experiments. *Nature*, 533:73–76, 2016.

[57] B. Meredig, A. Agrawal, S. Kirklin, J. E. Saal, J. W. Doak, A. Thompson, K. Zhang, A. Choudhary, and C. Wolverton. Combinatorial screening for new materials in unconstrained composition space with machine learning. *Phys. Rev. B*, 89:094104, 2014.

[58] Shuaihua Lu, Qionghua Zhou, Yixin Ouyang, Yilv Guo, Qiang Li, and Jinlan Wang. Accelerated discovery of stable lead-free hybrid organic-inorganic perovskites via machine learning. *Nat. Commun.*, 9:3405, 2018.

[59] Woon Seok Yang, Byung-Wook Park, Eui Hyuk Jung, Nam Joong Jeon, Young Chan Kim, Dong Uk Lee, Seong Sik Shin, Jangwon Seo, Eun Kyu Kim, Jun Hong Noh, and Sang Il Seok. Iodide management in formamidinium-lead-halide–based perovskite layers for efficient solar cells. *Science*, 356:1376–1379, 2017.

[60] Jingying Liu, Yunzhou Xue, Ziyu Wang, Zai-Quan Xu, Changxi Zheng, Bent Weber, Jingchao Song, Yusheng Wang, Yuerui Lu, Yupeng Zhang, and Qiaoliang Bao. Two-dimensional $CH_3NH_3PbI_3$ perovskite: Synthesis and optoelectronic application. *ACS Nano*, 10:3536–3542, 2016.

[61] Tom Baikie, Yanan Fang, Jeannette M. Kadro, Martin Schreyer, Fengxia Wei, Subodh G. Mhaisalkar, Michael Graetzel, and Tim J. White. Synthesis and crystal chemistry of the hybrid perovskite $(CH_3NH_3)PbI_3$ for solid-state sensitised solar cell applications. *J. Mater. Chem. A*, 1:5628–5641, 2013.

[62] David B. Mitzi. Synthesis, crystal structure, and optical and thermal properties of $(C_4H_9NH_3)_2MI_4$ (m = ge, sn, pb). *Chem. Mater.*, 8:791–800, 1996.

[63] Jun Xing, Xin Feng Liu, Qing Zhang, Son Tung Ha, Yan Wen Yuan, Chao Shen, Tze Chien Sum, and Qihua Xiong. Vapor phase synthesis of organometal halide perovskite nanowires for tunable room-temperature nanolasers. *Nano Lett.*, 15:4571–4577, 2015.

[64] Nakita K. Noel, Samuel D. Stranks, Antonio Abate, Christian Wehrenfennig, Simone Guarnera, Amir-Abbas Haghighirad, Aditya Sadhanala, Giles E. Eperon, Sandeep K. Pathak, Michael B. Johnston, Annamaria Petrozza, Laura M. Herz, and Henry J. Snaith. Lead-free organic–inorganic tin halide perovskites for photovoltaic applications. *Energy Environ. Sci.*, 7:3061–3068, 2014.

[65] Guangda Niu, Wenzhe Li, Fanqi Meng, Liduo Wang, Haopeng Dong, and Yong Qiu. Study on the stability of $ch_3nh_3pbi_3$ films and the effect of post-modification by aluminum oxide in all-solid-state hybrid solar cells. *J. Mater. Chem. A*, 2:705–710, 2014.

[66] Andrei Buin, Patrick Pietsch, Jixian Xu, Oleksandr Voznyy, Alexander H Ip, Riccardo Comin, and Edward H Sargent. Materials processing routes to trap-free halide perovskites. *Nano Lett.*, 14:6281–6286, 2014.

[67] G. P. Nagabhushana, Radha Shivaramaiah, and Alexandra Navrotsky. Direct calorimetric verification of thermodynamic instability of lead halide hybrid perovskites. *Proc. Natl. Acad. Sci.*, 113:7717–7721, 2016.

[68] Sudip Chakraborty, Wei Xie, Nripan Mathews, Matthew Sherburne, Rajeev Ahuja, Mark Asta, and Subodh G. Mhaisalkar. Rational design: A high-throughput computational screening and experimental validation methodology for lead-free and emergent hybrid perovskites. *ACS Energy Lett.*, 2:837–845, 2017.

[69] Sabine Körbel, Miguel A. L. Marques, and Silvana Botti. Stability and electronic properties of new inorganic perovskites from high-throughput ab initio calculations. *J. Mater. Chem. C*, 4:3157–3167, 2016.

[70] G. Pilania, J.E. Gubernatis, and T. Lookman. Multi-fidelity machine learning models for accurate bandgap predictions of solids. *Comput. Mater. Sci.*, 129:156–163, 2017.

[71] Mikhail Askerka, Ziliang Li, Mathieu Lempen, Yanan Liu, Andrew Johnston, Makhsud I. Saidaminov, Zoltan Zajacz, and Edward H. Sargent. Learning-in-templates enables accelerated discovery and synthesis of new stable double perovskites. *J. Am. Chem. Soc.*, 141:3682–3690, 2019.

[72] Zhenzhu Li, Qichen Xu, Qingde Sun, Zhufeng Hou, and Wan-Jian Yin. Thermodynamic stability landscape of halide double perovskites via high-throughput computing and machine learning. *Adv. Fun. Mater.*, 29:1807280, 2019.

[73] Logan Ward, Alexander Dunn, Alireza Faghaninia, Nils E.R. Zimmermann, Saurabh Bajaj, Qi Wang, Joseph Montoya, Jiming Chen, Kyle Bystrom, Maxwell Dylla, Kyle Chard, Mark Asta, Kristin A. Persson, G. Jeffrey Snyder, Ian Foster, and Anubhav Jain. Matminer: An open source toolkit for materials data mining. *Comput. Mater. Sci.*, 152:60–69, 2018.

[74] F. Pedregosa, G. Varoquaux, A. Gramfort, V. Michel, B. Thirion, O. Grisel, M. Blondel, P. Prettenhofer, R. Weiss, V. Dubourg, J. Vanderplas, A. Passos, D. Cournapeau, M. Brucher, M. Perrot, and E. Duchesnay. Scikit-learn: Machine learning in Python. *J. Mach. Learn. Res.*, 12:2825–2830, 2011.

[75] Tianqi Chen and Carlos Guestrin. Xgboost: A scalable tree boosting system. In *Proceedings of the 22Nd ACM SIGKDD International Conference on Knowledge Discovery and Data Mining*, KDD '16, pages 785–794, New York, NY, USA, 2016. ACM.

[76] Zeyu Deng, Fengxia Wei, Shijing Sun, Gregor Kieslich, Anthony K. Cheetham, and Paul D. Bristowe. Exploring the properties of lead-free hybrid double perovskites using a combined computational-experimental approach. *J. Mater. Chem. A*, 4:12025–12029, 2016.

[77] Akihiro Kojima, Kenjiro Teshima, Yasuo Shirai, and Tsutomu Miyasaka. Organometal halide perovskites as visible-light sensitizers for photovoltaic cells. *J. Am. Chem. Soc.*, 131:6050–6051, 2009.

[78] Gary Hodes. Perovskite-based solar cells. *Science*, 342:317–318, 2013.

[79] Mingzhen Liu, Michael B. Johnston, and Henry J. Snaith. Efficient planar heterojunction perovskite solar cells by vapour deposition. *Nature*, 501:395–398, 2013.

[80] Julian Burschka, Norman Pellet, Soo-Jin Moon, Robin Humphry-Baker, Peng Gao, Mohammad K. Nazeeruddin, and Michael Grätzel. Sequential deposition as a route to high-performance perovskite-sensitized solar cells. *Nature*, 499:316–319, 2013.

[81] Michael Gratzel. The light and shade of perovskite solar cells. *Nat. Mater.*, 13:838–842, 2014.

[82] Jin Hyuck Heo, Sang Hyuk Im, Jun Hong Noh, Tarak N. Mandal, Choong-Sun Lim, Jeong Ah Chang, Yong Hui Lee, Hi-jung Kim, Arpita Sarkar, K. NazeeruddinMd, Michael Gratzel, and Sang Il Seok. Efficient inorganic-organic hybrid heterojunction solar cells containing perovskite compound and polymeric hole conductors. *Nat. Photon.*, 7:486–491, 2013.

[83] Jeong-Hyeok Im, In-Hyuk Jang, Norman Pellet, Michael Grätzel, and Nam-Gyu Park. Growth of $CH_3NH_3PbI_3$ cuboids with controlled size for high-efficiency perovskite solar cells. *Nat. Nanotechnol.*, 9:927–932, 2014.

[84] Nam Joong Jeon, Jun Hong Noh, Young Chan Kim, Woon Seok Yang, Seungchan Ryu, and Sang Il Seok. Solvent engineering for high-performance inorganic–organic hybrid perovskite solar cells. *Nat. Mater.*, 13:897–903, 2014.

[85] Nam Joong Jeon, Jun Hong Noh, Woon Seok Yang, Young Chan Kim, Seungchan Ryu, Jangwon Seo, and Sang Il Seok. Compositional engineering of perovskite materials for high-performance solar cells. *Nature*, 517:476–480, 2015.

[86] Feng Hao, Constantinos C. Stoumpos, Duyen Hanh Cao, Robert P. H. Chang, and Mercouri G. Kanatzidis. Lead-free solid-state organic–inorganic halide perovskite solar cells. *Nat. Photon.*, 8:489–494, 2014.

[87] Huanping Zhou, Qi Chen, Gang Li, Song Luo, Tze-bing Song, Hsin-Sheng Duan, Ziruo Hong, Jingbi You, Yongsheng Liu, and Yang Yang. Interface engineering of highly efficient perovskite solar cells. *Science*, 345:542–546, 2014.

[88] Samuel D Stranks, Giles E Eperon, Giulia Grancini, Christopher Menelaou, Marcelo JP Alcocer, Tomas Leijtens, Laura M Herz, Annamaria Petrozza, and Henry J Snaith. Electron-hole diffusion lengths exceeding 1 micrometer in an organometal trihalide perovskite absorber. *Science*, 342:341–344, 2013.

[89] Guichuan Xing, Nripan Mathews, Shuangyong Sun, Swee Sien Lim, Yeng Ming Lam, Michael Grätzel, Subodh Mhaisalkar, and Tze Chien Sum. Long-range balanced electron- and hole-transport lengths in organic–inorganic $CH_3NH_3PbI_3$. *Science*, 342:344–347, 2013.

[90] David B. Mitzi. Templating and structural engineering in organic-inorganic perovskites. *J. Chem. Soc., Dalton Trans.*, 1:1–12, 2001.

[91] Constantinos C Stoumpos, Christos D Malliakas, and Mercouri G Kanatzidis. Semiconducting tin and lead iodide perovskites with organic cations: Phase transitions, high mobilities, and near-infrared photoluminescent properties. *Inorganic chemistry*, 52:9019–9038, 2013.

[92] Michael D. McGehee. Continuing to soar. *Nat. Mater.*, 13:845–846, 2014.

[93] Haiming Zhu, Kiyoshi Miyata, Yongping Fu, Jue Wang, Prakriti P Joshi, Daniel Niesner, Kristopher W Williams, Song Jin, and X-Y Zhu. Screening in crystalline liquids protects energetic carriers in hybrid perovskites. *Science*, 353:1409–1413, 2016.

[94] Haiming Zhu, Yongping Fu, Fei Meng, Xiaoxi Wu, Zizhou Gong, Qi Ding, Martin V. Gustafsson, M. Tuan Trinh, Song Jin, and X.-Y. Zhu. Lead halide perovskite nanowire lasers with low lasing thresholds and high quality factors. *Nat. Mater.*, 14:636–642, 2015.

[95] Qingfeng Dong, Yanjun Fang, Yuchuan Shao, Padhraic Mulligan, Jie Qiu, Lei Cao, and Jinsong Huang. Electron-hole diffusion lengths > 175 μm in solution-grown $CH_3NH_3PbI_3$ single crystals. *Science*, 347:967–970, 2015.

[96] Wanyi Nie, Hsinhan Tsai, Reza Asadpour, Jean-Christophe Blancon, Amanda J. Neukirch, Gautam Gupta, Jared J. Crochet, Manish Chhowalla, Sergei Tretiak, Muhammad A. Alam, Hsing-Lin Wang, and Aditya D. Mohite. High-efficiency solution-processed perovskite solar cells with millimeter-scale grains. *Science*, 347:522–525, 2015.

[97] Kiyoshi Miyata, Daniele Meggiolaro, M. Tuan Trinh, Prakriti P. Joshi, Edoardo Mosconi, Skyler C. Jones, Filippo De Angelis, and X.-Y. Zhu. Large polarons in lead halide perovskites. *Sci. Adv.*, 3:e1701217, 2017.

[98] Thomas M. Brenner, David A. Egger, Leeor Kronik, Gary Hodes, and David Cahen. Hybrid organic–inorganic perovskites: Low-cost semiconductors with intriguing charge-transport properties. *Nat. Rev. Mater.*, 1:15007, 2016.

[99] Wei Zhang, Giles E. Eperon, and Henry J. Snaith. Metal halide perovskites for energy applications. *Nat. Energy.*, 1:16048, 2016.

[100] Kiyoshi Miyata, Timothy L. Atallah, and X.-Y. Zhu. Lead halide perovskites: Crystal-liquid duality, phonon glass electron crystals, and large polaron formation. *Sci. Adv.*, 3:e1701469, 2017.

[101] Jingbi You, Lei Meng, Tze-Bin Song, Tzung-Fang Guo, Yang (Michael) Yang, Wei-Hsuan Chang, Ziruo Hong, Huajun Chen, Huanping Zhou, Qi Chen, Yongsheng Liu, Nicholas De Marco, and Yang Yang. Improved air stability of perovskite solar cells via solution-processed metal oxide transport layers. *Nat. Nanotechnol.*, 11:75–81, 2015.

[102] Woon Seok Yang, Jun Hong Noh, Nam Joong Jeon, Young Chan Kim, Seungchan Ryu, Jangwon Seo, and Sang Il Seok. High-performance photovoltaic perovskite layers fabricated through intramolecular exchange. *Science*, 348:1234–1237, 2015.

[103] Dane W. deQuilettes, Sarah M. Vorpahl, Samuel D. Stranks, Hirokazu Nagaoka, Giles E. Eperon, Mark E. Ziffer, Henry J. Snaith, and David S. Ginger. Impact of microstructure on local carrier lifetime in perovskite solar cells. *Science*, EMPTY:aaa5333, 2015.

[104] David P. McMeekin, Golnaz Sadoughi, Waqaas Rehman, Giles E. Eperon, Michael Saliba, Maximilian T. Hörantner, Amir Haghighirad, Nobuya Sakai, Lars Korte, Bernd Rech, Michael B. Johnston, Laura M. Herz, and Henry J. Snaith. A mixed-cation lead mixed-halide perovskite absorber for tandem solar cells. *Science*, 351:151–155, 2016.

[105] Anyi Mei, Xiong Li, Linfeng Liu, Zhiliang Ku, Tongfa Liu, Yaoguang Rong, Mi Xu, Min Hu, Jiangzhao Chen, Ying Yang, Michael Grätzel, and Hongwei Han. A hole-conductor–free, fully printable mesoscopic perovskite solar cell with high stability. *Science*, 345:295–298, 2014.

[106] Wei Chen, Yongzhen Wu, Youfeng Yue, Jian Liu, Wenjun Zhang, Xudong Yang, Han Chen, Enbing Bi, Islam Ashraful, Michael Grätzel, and Liyuan Han. Efficient and stable large-area perovskite solar cells with inorganic charge extraction layers. *Science*, 350:aad1015, 2015.

[107] Qianqian Lin, Ardalan Armin, Ravi Chandra Raju Nagiri, Paul L. Burn, and Paul Meredith. Electro-optics of perovskite solar cells. *Nat. Photon.*, 9:106–112, 2014.

[108] Olga Malinkiewicz, Aswani Yella, Yong Hui Lee, Guillermo Mínguez Espallargas, Michael Graetzel, Mohammad K. Nazeeruddin, and Henk J. Bolink. Perovskite solar cells employing organic charge-transport layers. 8:128–132, 2013.

[109] Martin A. Green, Anita Ho-Baillie, and Henry J. Snaith. The emergence of perovskite solar cells. 8:506–514, 2014.

[110] Dong Shi, Valerio Adinolfi, Riccardo Comin, Mingjian Yuan, Erkki Alarousu, Andrei Buin, Yin Chen, Sjoerd Hoogland, Alexander Rothenberger, Khabiboulakh Katsiev, Yaroslav Losovyj, Xin Zhang, Peter A. Dowben, Omar F. Mohammed, Edward H. Sargent, and Osman M. Bakr. Low trap-state density and long carrier diffusion in organolead trihalide perovskite single crystals. *Science*, 347:519–522, 2015.

[111] National Renewable Energy Laboratory. Research cell record efficiency chart, 2017. [Online; accessed June 10, 2017].

[112] Guangda Niu, Xudong Guo, and Liduo Wang. Review of recent progress in chemical stability of perovskite solar cells. *J. Mater. Chem. A*, 3:8970–8980, 2015.

[113] Yu Han, Steffen Meyer, Yasmina Dkhissi, Karl Weber, Jennifer M. Pringle, Udo Bach, Leone Spiccia, and Yi-Bing Cheng. Degradation observations of encapsulated planar ch$_3$nh$_3$pbi$_3$ perovskite solar cells at high temperatures and humidity. *J. Mater. Chem. A*, 3:8139–8147, 2015.

[114] Duyen H. Cao, Constantinos C. Stoumpos, Takamichi Yokoyama, Jenna L. Logsdon, Tze-Bin Song, Omar K. Farha, Michael R. Wasielewski, Joseph T. Hupp, and Mercouri G. Kanatzidis. Thin films and solar cells based on semiconducting two-dimensional ruddlesden–popper (CH$_3$(CH$_2$)$_3$NH$_3$)$_2$(CH$_3$NH$_3$)$_{n-1}$Sn$_n$I$_{3n+1}$ perovskites. *ACS Energy Lett.*, 2:982–990, 2017.

[115] Hsinhan Tsai, Wanyi Nie, Jean-Christophe Blancon, Constantinos C. Stoumpos, Reza Asadpour, Boris Harutyunyan, Amanda J. Neukirch, Rafael Verduzco, Jared J. Crochet, Sergei Tretiak, Laurent Pedesseau, Jacky Even, Muhammad A. Alam, Gautam Gupta, Jun Lou, Pulickel M. Ajayan, Michael J. Bedzyk, Mercouri G. Kanatzidis, and Aditya D. Mohite. High-efficiency two-dimensional ruddlesden-popper perovskite solar cells. *Nature*, 536:312–316, 2016.

[116] Alex M. Ganose, Christopher N. Savory, and David O. Scanlon. (CH$_3$NH$_3$)$_2$Pb(SCN)$_2$I$_2$: A more stable structural motif for hybrid halide photovoltaics? *J. Phys. Chem. Lett.*, 6:4594–4598, 2015.

[117] Jinwoo Byun, Himchan Cho, Christoph Wolf, Mi Jang, Aditya Sadhanala, Richard H Friend, Hoichang Yang, and Tae-Woo Lee. Efficient visible quasi-2d perovskite light-emitting diodes. *Adv. Mater.*, 28:7515–7520, 2016.

[118] Bat-El Cohen, Małgorzata Wierzbowska, and Lioz Etgar. High efficiency and high open circuit voltage in quasi 2d perovskite based solar cells. *Adv. Fun. Mater.*, 27:1604733, 2016.

[119] Mingjian Yuan, Li Na Quan, Riccardo Comin, Grant Walters, Randy Sabatini, Oleksandr Voznyy, Yongbiao Hoogland, Sjoerdand Zhao, Eric M. Beauregard, Pongsakorn Kanjanaboos, Zhenghong Lu, Dong Ha Kim, and Edward H. Sargent. Perovskite energy funnels for efficient light-emitting diodes. *Nat. Nanotechnol.*, 11:872–877, 2016.

[120] Ian C. Smith, Eric T. Hoke, Diego Solis-Ibarra, Michael D. McGehee, and Hemamala I. Karunadasa. A layered hybrid perovskite solar-cell absorber with enhanced moisture stability. *Angew. Chem.*, 126:11414–11417, 2014.

[121] Sanjun Zhang, Gaëtan Lanty, Jean-Sébastien Lauret, Emmanuelle Deleporte, Pierre Audebert, and Laurent Galmiche. Synthesis and optical properties of novel organic–inorganic hybrid nanolayer structure semiconductors. *Acta Mater.*, 57:3301–3309, 2009.

[122] Son-Tung Ha, Chao Shen, Jun Zhang, and Qihua Xiong. Laser cooling of organic–inorganic lead halide perovskites. *Nat. Photon.*, 10:115–121, 2015.

[123] Constantinos C. Stoumpos, Duyen H. Cao, Daniel J. Clark, Joshua Young, James M. Rondinelli, Joon I. Jang, Joseph T. Hupp, and Mercouri G. Kanatzidis. Ruddlesden-popper hybrid lead iodide perovskite 2d homologous semiconductors. *Chem. Mater.*, 28:2852–2867, 2016.

[124] Jeong-Hyeok Im, Hui-Seon Kim, and Nam-Gyu Park. Morphology-photovoltaic property correlation in perovskite solar cells: One-step versus two-step deposition of $CH_3NH_3PbI_3$. *APL Mater.*, 2:081510, 2014.

[125] Junnian Chen, Yaguang Wang, Lin Gan, Yunbin He, Huiqiao Li, and Tianyou Zhai. Generalized self-doping engineering towards ultrathin and large-sized two-dimensional homologous perovskites. *Angew. Chem.*, 129:15089–15093, 2017.

[126] Yun Lin, Yang Bai, Yanjun Fang, Zhaolai Chen, Shuang Yang, Xiaopeng Zheng, Shi Tang, Ye Liu, Jingjing Zhao, and Jinsong Huang. Enhanced thermal stability in perovskite solar cells by assembling 2d/3d stacking structures. *J. Phys. Chem. Lett.*, 9:654–658, 2018.

[127] Lingling Mao, Hsinhan Tsai, Wanyi Nie, Lin Ma, Jino Im, Constantinos C. Stoumpos, Christos D. Malliakas, Feng Hao, Michael R. Wasielewski, Aditya D. Mohite, and Mercouri G. Kanatzidis. Role of organic counterion in lead- and tin-based two-dimensional semiconducting iodide perovskites and application in planar solar cells. *Chem. Mater.*, 28:7781–7792, 2016.

[128] Edward P. Booker, Tudor H. Thomas, Claudio Quarti, Michael R. Stanton, Cameron D. Dashwood, Alexander J. Gillett, Johannes M. Richter, Andrew J. Pearson, Nathaniel J. L. K. Davis, Henning Sirringhaus, Michael B. Price, Neil C. Greenham, David Beljonne, Siân E. Dutton, and Felix Deschler. Formation of long-lived color centers for broadband visible light emission in low-dimensional layered perovskites. *J. Am. Chem. Soc.*, 139:18632–18639, 2017.

[129] G Lanty, A Bréhier, R Parashkov, J S Lauret, and E Deleporte. Strong exciton–photon coupling at room temperature in microcavities containing two-dimensional layered perovskite compounds. *New J. Phys.*, 10:065007, 2008.

[130] Zewen Xiao, Weiwei Meng, Bayrammurad Saparov, Hsin-Sheng Duan, Changlei Wang, Chunbao Feng, Wei-Qiang Liao, Weijun Ke, Dewei Zhao, Jianbo Wang, David B. Mitzi, and

Yanfa Yan. Photovoltaic properties of two-dimensional $(CH_3NH_3)_2Pb(SCN)_2I_2$ perovskite: A combined experimental and density-functional theory study. *J. Phys. Chem. Lett.*, 7:1213–1218, 2016.

[131] Yan Sun, Li Zhang, Nana Wang, Shuting Zhang, Yu Cao, Yanfeng Miao, Mengmeng Xu, Hao Zhang, Hai Li, Chang Yi, Jianpu Wang, and Wei Huang. The formation of perovskite multiple quantum well structures for high performance light-emitting diodes. *npj Flexible Electronics*, 2:12, 2018.

[132] A. Yangui, S. Pillet, A. Mlayah, A. Lusson, G. Bouchez, S. Triki, Y. Abid, and K. Boukhed-daden. Structural phase transition causing anomalous photoluminescence behavior in per-ovskite $(C_6H_{11}NH_3)_2[PbI_4]$. *J. Chem. Phys.*, 143:224201, 2015.

[133] Khaoula Lanty, Gaëtan ad Jemli, Yi Wei, Joël Leymarie, Jacky Even, Jean-Sébastien Lauret, and Emmanuelle Deleporte. Room-temperature optical tunability and inhomogeneous broad-ening in 2d-layered organic–inorganic perovskite pseudobinary alloys. *J. Phys. Chem. Lett.*, 5:3958–3963, 2014.

[134] Xiaoxi Wu, M. Tuan Trinh, Daniel Niesner, Haiming Zhu, Zachariah Norman, Jonathan S. Owen, Omer Yaffe, Bryan J. Kudisch, and X.-Y. Zhu. Trap states in lead iodide perovskites. *J. Am. Chem. Soc.*, 137:2089–2096, 2015.

[135] K. Abdel-Baki, F. Boitier, H. Diab, G. Lanty, K. Jemli, F. Lédée, D. Garrot, E. Deleporte, and J. S. Lauret. Exciton dynamics and non-linearities in two-dimensional hybrid organic perovskites. *J. Appl. Phys.*, 119:064301, 2016.

[136] Daniele Cortecchia, Kar Cheng Lew, Jin-Kyu So, Annalisa Bruno, and Cesare Soci. Cathodo-luminescence of self-organized heterogeneous phases in multidimensional perovskite thin films. *Chem. Mater.*, 29:10088–10094, 2017.

[137] R. Hamaguchi, M. Yoshizawa-Fujita, T. Miyasaka, H. Kunugita, K. Ema, Y. Takeoka, and M. Rikukawa. Formamidine and cesium-based quasi-two-dimensional perovskites as photovoltaic absorbers. *Chem. Commun.*, 53:4366–4369, 2017.

[138] Daniele Cortecchia, Herlina Arianita Dewi, Jun Yin, Annalisa Bruno, Shi Chen, Tom Baikie, Pablo P. Boix, Michael Grätzel, Subodh Mhaisalkar, Cesare Soci, and Nripan Mathews. Lead-free $MA_2CuCl_xBr_{4−X}$ hybrid perovskites. *Inorg. Chem.*, 55:1044–1052, 2016.

[139] Giulia Grancini, Cristina Carmona, Iwan Zimmermann, E Mosconi, X Lee, D Martineau, S Narbey, Frédéric Oswald, Filippo Angelis, Michael Graetzel, and Mohammad Nazeeruddin. One-year stable perovskite solar cells by 2d/3d interface engineering. *Nat. Commun.*, 8:1–8, 2017.

[140] Teck Ming Koh, Vignesh Shanmugam, Johannes Schlipf, Lukas Oesinghaus, Peter Müller-Buschbaum, N. Ramakrishnan, Varghese Swamy, Nripan Mathews, Pablo P. Boix, and Subodh G. Mhaisalkar. Nanostructuring mixed-dimensional perovskites: A route toward tunable, efficient photovoltaics. *Adv. Mater.*, 28:3653–3661, 2016.

[141] Naveen R. Venkatesan, John G. Labram, and Michael L. Chabinyc. Charge-carrier dynamics and crystalline texture of layered ruddlesden–popper hybrid lead iodide perovskite thin films. *ACS Energy Lett.*, 3:380–386, 2018.

[142] Chinnambedu Murugesan Raghavan, Tzu-Pei Chen, Shao-Sian Li, Wei-Liang Chen, Chao-Yuan Lo, Yu-Ming Liao, Golam Haider, Cheng-Chieh Lin, Chia-Chun Chen, Raman Sankar, Yu-Ming Chang, Fang-Cheng Chou, and Chun-Wei Chen. Low-threshold lasing from 2d homologous organic–inorganic hybrid ruddlesden–popper perovskite single crystals. *Nano Lett.*, 18:3221–3228, 2018.

[143] Aymen Yangui, Sebastien Pillet, El-Eulmi Bendeif, Alain Lusson, Smail Triki, Younes Abid, and Kamel Boukheddaden. Broadband emission in a new two-dimensional cd-based hybrid perovskite. *ACS Photonics*, 5:1599–1611, 2018.

[144] Ning Zhou, Yiheng Shen, Liang Li, Shunquan Tan, Na Liu, Guanhaojie Zheng, Qi Chen, and Huanping Zhou. Exploration of crystallization kinetics in quasi two-dimensional perovskite and high performance solar cells. *J. Am. Chem. Soc.*, 140:459–465, 2018.

[145] Anastasia Vassilakopoulou, Dionysios Papadatos, Ioannis Zakouras, and Ioannis Koutselas. Mixtures of quasi-two and three dimensional hybrid organic-inorganic semiconducting perovskites for single layer led. *J. Alloys Compound.*, 692:589–598, 2017.

[146] Letian Dou, Andrew B. Wong, Yi Yu, Minliang Lai, Nikolay Kornienko, Samuel W. Eaton, Anthony Fu, Connor G. Bischak, Jie Ma, Tina Ding, Naomi S. Ginsberg, Lin-Wang Wang, A. Paul Alivisatos, and Peidong Yang. Atomically thin two-dimensional organic–inorganic hybrid perovskites. *Science*, 349:1518–1521, 2015.

[147] Omer Yaffe, Alexey Chernikov, Zachariah M. Norman, Yu Zhong, Ajanthkrishna Velauthapillai, Arend van der Zande, Jonathan S. Owen, and Tony F. Heinz. Excitons in ultrathin organic–inorganic perovskite crystals. *Phys. Rev. B*, 92:045414, 2015.

[148] Wendy Niu, Anna Eiden, G. Vijaya Prakash, and Jeremy J. Baumberg. Exfoliation of self-assembled 2d organic–inorganic perovskite semiconductors. *Appl. Phys. Lett.*, 104:171111, 2014.

[149] Zhi Guo, Xiaoxi Wu, Tong Zhu, Xiaoyang Zhu, and Libai Huang. Electron–phonon scattering in atomically thin 2d perovskites. *ACS Nano*, 10:9992–9998, 2016.

[150] Junnian Chen, Lin Gan, Fuwei Zhuge, Huiqiao Li, Jizhong Song, Haibo Zeng, and Tianyou Zhai. A ternary solvent method for large-sized two-dimensional perovskites. *Angew. Chem. Int. Ed.*, 56:2390–2394, 2017.

[151] Robert Younts, Hsin-Sheng Duan, Bhoj Gautam, Bayrammurad Saparov, Jie Liu, Cedric Mongin, Felix N. Castellano, David B. Mitzi, and Kenan Gundogdu. Efficient generation of long-lived triplet excitons in 2d hybrid perovskite. *Adv. Mater.*, 29:1604278, 2016.

[152] Guo Jia, Ze-Jiao Shi, Ying-Dong Xia, Qi Wei, Yong-Hua Chen, Gui-Chuan Xing, and Wei Huang. Super air stable quasi-2d organic-inorganic hybrid perovskites for visible light-emitting diodes. *Opt. Express*, 26:A66–A74, 2018.

[153] Kecai Xiong, Wei Liu, Simon J. Teat, Litao An, Hao Wang, Thomas J. Emge, and Jing Li. New hybrid lead iodides: From one-dimensional chain to two-dimensional layered perovskite structure. *J. Solid State Chem.*, 230:143–148, 2015.

[154] Ishita Neogi, Annalisa Bruno, Damodaran Bahulayan, Teck Wee Goh, Biplab Ghosh, Rakesh Ganguly, Daniele Cortecchia, Tze Chien Sum, Cesare Soci, Nripan Mathews, and Subodh Gautam Mhaisalkar. Broadband-emitting 2d hybrid organic–inorganic perovskite based on cyclohexane-bis(methylamonium) cation. *ChemSusChem*, 10:3765–3772, 2017.

[155] Dejian Yu, Chunyang Yin, Fei Cao, Ying Zhu, Jianping Ji, Bo Cai, Xuhai Liu, Xiaoyong Wang, and Haibo Zeng. Enhancing optoelectronic properties of low-dimensional halide perovskite via ultrasonic-assisted template refinement. *ACS Appl. Mater. Interfaces*, 9:39602–39609, 2017.

[156] Liyuan Wu, Pengfei Lu, Yuheng Li, Yan Sun, Joseph Wong, and Kesong Yang. First-principles characterization of two-dimensional $(CH_3(CH_2)_3NH_3)_2(CH_3NH_3)_{n-1}Ge_nI_{3n+1}$ perovskite. *J. Mater. Chem. A*, 6:24389–24396, 2018.

[157] Ashok K. Vishwakarma, Prasanna S. Ghalsasi, Arulsamy Navamoney, Yanhua Lan, and A.K. Powell. Structural phase transition and magnetic properties of layered organicâĂŞinorganic hybrid compounds: P-haloanilinium tetrachlorocuparate(ii). *Polyhedron*, 30:1565–1570, 2011.

[158] Wei-Qiang Liao, Yi Zhang, Chun-Li Hu, Jiang-Gao Mao, Heng-Yun Ye, Peng-Fei Li, Songping D. Huang, and Ren-Gen Xiong. A lead-halide perovskite molecular ferroelectric semiconductor. *Nat. Commun.*, 6:7338, 2015.

[159] K. Pradeesh, K. Nageswara Rao, and G. Vijaya Prakash. Synthesis, structural, thermal and optical studies of inorganic-organic hybrid semiconductors, R-PbI$_4$. *J. Appl. Phys.*, 113:083523, 2013.

[160] Alberto García-Fernández, Juan Manuel Bermúdez-García, Socorro Castro-García, Antonio Luis Llamas-Saiz, Ramón Artiaga, Jorge José López-Beceiro, Manuel Sánchez-Andújar, and María Antonia Señarís-Rodríguez. $[(CH_3)_2NH_2]_7Pb_4X_{15}$ (x = cl$^-$ and br$^-$), 2d-perovskite related hybrids with dielectric transitions and broadband photoluminiscent emission. *Inorg. Chem.*, 57:3215–3222, 2018.

[161] Lingling Mao, Yilei Wu, Constantinos C. Stoumpos, Michael R. Wasielewski, and Mercouri G. Kanatzidis. White-light emission and structural distortion in new corrugated two-dimensional lead bromide perovskites. *J. Am. Chem. Soc.*, 139:5210–5215, 2017.

[162] Emma R. Dohner, Adam Jaffe, Liam R. Bradshaw, and Hemamala I. Karunadasa. Intrinsic white-light emission from layered hybrid perovskites. *J. Am. Chem. Soc.*, 136:13154–13157, 2014.

[163] Alberto Fraccarollo, Leonardo Marchese, and Maurizio Cossi. Ab initio design of low band gap 2d tin organohalide perovskites. *J. Phys. Chem. C*, 122:3677–3689, 2018.

[164] Emma R. Dohner, Eric T. Hoke, and Hemamala I. Karunadasa. Self-assembly of broadband white-light emitters. *J. Am. Chem. Soc.*, 136:1718–1721, 2014.

[165] Jin-Peng Li, Long-Hua Li, Li-Ming Wu, and Ling Chen. Synthesis, properties, and theoretical studies of new stepwise layered iodoplumbate: $[Ni(opd)_2(acn)_2]_n[Pb_4I_{10}]_n$. *Inorg. Chem.*, 48:1260–1262, 2009.

[166] Dewei Ma and Yidan He. Syntheses of needle-shaped layered perovskite $(C_6H_5CH_2NH_3)_2PbI_4$ bundles via a two-step processing technique. *J. Alloys Compound.*, 696:1213–1219, 2017.

[167] Constantinos C. Stoumpos, Chan Myae Myae Soe, Hsinhan Tsai, Wanyi Nie, Jean-Christophe Blancon, Duyen H. Cao, Fangze Liu, Boubacar Traoré, Claudine Katan, Jacky Even, Aditya D. Mohite, and Mercouri G. Kanatzidis. High members of the 2d ruddlesden-popper halide perovskites: Synthesis, optical properties, and solar cells of $(CH_3(CH_2)_3NH_3)_2(CH_3NH_3)_4Pb_5I_{16}$. *Chem*, 2:427–440, 2017.

[168] Jing Han, Sadafumi Nishihara, Katsuya Inoue, and Mohamedally Kurmoo. On the nature of the structural and magnetic phase transitions in the layered perovskite-like $(CH_3NH_3)_2[Fe^{II}Cl_4]$. *Inorg. Chem.*, 53:2068–2075, 2014.

[169] Michael Daub and Harald Hillebrecht. Synthesis, single-crystal structure and characterization of $(CH_3NH_3)_2Pb(SCN)_2I_2$. *Angew. Chem. Int. Ed.*, 54:11016–11017, 2015.

[170] Alexey O. Polyakov, Anne H. Arkenbout, Jacob Baas, Graeme R. Blake, Auke Meetsma, Antonio Caretta, Paul H. M. van Loosdrecht, and Thomas T. M. Palstra. Coexisting ferromagnetic and ferroelectric order in a $CuCl_4$-based organic–inorganic hybrid. *Chem. Mater.*, 24:133–139, 2012.

[171] David G. Billing and Andreas Lemmerer. Synthesis, characterization and phase transitions of the inorganic–organic layered perovskite-type hybrids $[(C_nH_{2n+1}NH_3)_2PbI_4]$ (n = 12, 14, 16 and 18). *New J. Chem.*, 32:1736–1746, 2008.

[172] Gang Tang, Chao Yang, Alessandro Stroppa, Daining Fang, and Jiawang Hong. Revealing the role of thiocyanate anion in layered hybrid halide perovskite $(CH_3NH_3)_2Pb(SCN)_2I_2$. *J. Chem. Phys.*, 146:224702, 2017.

[173] Te Hu, Matthew D. Smith, Emma R. Dohner, Meng-Ju Sher, Xiaoxi Wu, M. Tuan Trinh, Alan Fisher, Jeff Corbett, X.-Y. Zhu, Hemamala I. Karunadasa, and Aaron M. Lindenberg. Mechanism for broadband white-light emission from two-dimensional (110) hybrid perovskites. *J. Phys. Chem. Lett.*, 7:2258–2263, 2016.

[174] X. Hong, T. Ishihara, and A. V. Nurmikko. Dielectric confinement effect on excitons in PbI_4-based layered semiconductors. *Phys. Rev. B*, 45:6961–6964, 1992.

[175] Wei Peng, Jun Yin, Kang-Ting Ho, Olivier Ouellette, Michele De Bastiani, Banavoth Murali, Omar El Tall, Chao Shen, Xiaohe Miao, Jun Pan, Erkki Alarousu, Jr-Hau He, Boon S. Ooi, Omar F. Mohammed, Edward Sargent, and Osman M. Bakr. Ultralow self-doping in two-dimensional hybrid perovskite single crystals. *Nano Lett.*, 17:4759–4767, 2017.

[176] Pengfei Cheng, Tao Wu, Junxue Liu, Wei-Qiao Deng, and Keli Han. Lead-free, two-dimensional mixed germanium and tin perovskites. *J. Phys. Chem. Lett.*, 9:2518–2522, 2018.

[177] Luis Lanzetta, Jose Manuel Marin-Beloqui, Irene Sanchez-Molina, Dong Ding, and Saif A. Haque. Two-dimensional organic tin halide perovskites with tunable visible emission and their use in light-emitting devices. *ACS Energy Lett.*, 2:1662–1668, 2017.

[178] Daniele Cortecchia, Stefanie Neutzner, Ajay Ram Srimath Kandada, Edoardo Mosconi, Daniele Meggiolaro, Filippo De Angelis, Cesare Soci, and Annamaria Petrozza. Broadband emission in two-dimensional hybrid perovskites: The role of structural deformation. *J. Am. Chem. Soc.*, 139:39–42, 2017.

[179] Camille Bernal and Kesong Yang. First-principles hybrid functional study of the organic-inorganic perovskites $CHNH_3SnBr_3$ and $CH_3NH_3SnI_3$. *J. Phys. Chem. C*, 118:24383–24388, 2014.

[180] Alberto Fraccarollo, Lorenzo Canti, Leonardo Marchese, and Maurizio Cossi. First principles study of 2d layered organohalide tin perovskites. *J. Chem. Phys.*, 146:234703, 2017.

[181] J. I Pankove. *Optical Processes in Semiconductors*. Dover publications (New York), 1975.

[182] Tianyi Wang, Benjamin Daiber, Jarvist M. Frost, Sander A. Mann, Erik C. Garnett, Aron Walsh, and Bruno Ehrler. Indirect to direct bandgap transition in methylammonium lead halide perovskite. *Energy Environ. Sci.*, 10:509–515, 2017.

[183] J Tauc, Radu Grigorovici, and Anina Vancu. Optical properties and electronic structure of amorphous germanium. *physica status solidi (b)*, 15:627–637, 1966.

[184] Bunsho Ohtani. Revisiting the fundamental physical chemistry in heterogeneous photo-catalysis: Its thermodynamics and kinetics. *Phys. Chem. Chem. Phys.*, 16:1788–1797, 2014.

[185] David Giovanni, Wee Kiang Chong, Herlina Arianita Dewi, Krishnamoorthy Thirumal, Ishita Neogi, Ramamoorthy Ramesh, Subodh Mhaisalkar, Nripan Mathews, and Tze Chien Sum. Tunable room-temperature spin-selective optical stark effect in solution-processed layered halide perovskites. *Sci. Adv.*, 2:e1600477, 2016.

[186] Edbert Jarvis Sie. *Valley-Selective Optical Stark Effect in Monolayer WS_2*. Springer International Publishing, Cham, 2018.

119

[187] Zhenjun Tan, Yue Wu, Hao Hong, Jianbo Yin, Jincan Zhang, Li Lin, Mingzhan Wang, Xiao Sun, Luzhao Sun, Yucheng Huang, Kaihui Liu, Zhongfan Liu, and Hailin Peng. Two-dimensional $(C_4H_9NH_3)_2PbBr_4$ perovskite crystals for high-performance photodetector. *J. Am. Chem. Soc.*, 138:16612–16615, 2016.

[188] E. Fred Schubert, Jaehee Cho, and Jong Kyu Kim. *Light-Emitting Diodes*. American Cancer Society, 2015.

[189] Zhi-Kuang Tan, Reza Saberi Moghaddam, May Ling Lai, Pablo Docampo, Ruben Higler, Felix Deschler, Michael Price, Aditya Sadhanala, Luis M. Pazos, Dan Credgington, Fabian Hanusch, Thomas Bein, Henry J. Snaith, and Richard H. Friend. Bright light-emitting diodes based on organometal halide perovskite. *Nat. Nanotechnol.*, 9:687–692, 2014.

[190] Young-Hoon Kim, Cho Himchan, Jin Hyuck Heo, Tae-Sik Kim, ung Myoung NoSo, Chang-Lyoul Lee, Hyuk Im Sang, and Tae-Woo Lee. Multicolored organic/inorganic hybrid perovskite light-emitting diodes. *Adv. Mater.*, 27:1248–1254, 2014.

[191] A. Yangui, D. Garrot, J. S. Lauret, A. Lusson, G. Bouchez, E. Deleporte, S. Pillet, E. E. Bendeif, M. Castro, S. Triki, Y. Abid, and K. Boukheddaden. Optical investigation of broadband white-light emission in self-assembled organic–inorganic perovskite $(C_6H_{11}NH_3)_2PbBr_4$. *J. Phys. Chem. C*, 119:23638–23647, 2015.

[192] Anastasia Vassilakopoulou, Dionysios Papadatos, and Ioannis Koutselas. Polystyrene based perovskite light emitting diode. *Applied Materials Today*, 12:15–20, 2018.

[193] Rico Meerheim, Sebastian Scholz, Selina Olthof, Gregor Schwartz, Sebastian Reineke, Karsten Walzer, and Karl Leo. Influence of charge balance and exciton distribution on efficiency and lifetime of phosphorescent organic light-emitting devices. *J. Appl. Phys.*, 104:014510, 2008.

[194] Chihaya Adachi, Marc A. Baldo, Mark E. Thompson, and Stephen R. Forrest. Nearly 100% internal phosphorescence efficiency in an organic light-emitting device. *J. Appl. Phys.*, 90:5048–5051, 2001.

[195] Hany Aziz and Zoran D. Popovic. Degradation phenomena in small-molecule organic light-emitting devices. *Chem. Mater.*, 16:4522–4532, 2004.

[196] Jason S. Ross, Philip Klement, Aaron M. Jones, Nirmal J. Ghimire, Jiaqiang Yan, D. G. Mandrus, Takashi Taniguchi, Kenji Watanabe, Kenji Kitamura, Wang Yao, David H. Cobden, and Xiaodong Xu. Electrically tunable excitonic light-emitting diodes based on monolayer WSe_2 p-n junctions. *Nat. Nanotechnol.*, 9:268–272, 2014.

[197] Jason Ross, Sanfeng Wu, Hongyi Yu, Nirmal Ghimire, Aaron Jones, Grant Aivazian, J.-Q Yan, David G Mandrus, Xiao di, Wang Yao, and Xiaodong Xu. Electrical control of neutral and charged excitons in a monolayer semiconductor. *Nat. Commun.*, 4:1474, 2013.

[198] Sanfeng Wu, Sonia Buckley, Aaron Jones, Jason Ross, Nirmal Ghimire, J.-Q Yan, David G. Mandrus, Wang Yao, Fariba Hatami, Jelena Vuckovic, Arka Majumdar, and Xiaodong Xu. Control of two-dimensional excitonic light emission via photonic crystal. *2D Mater.*, 1:011001, 2013.

[199] Daniel Sapori, Mikael Kepenekian, Laurent Pedesseau, Claudine Katan, and Jacky Even. Quantum confinement and dielectric profiles of colloidal nanoplatelets of halide inorganic and hybrid organic–inorganic perovskites. *Nanoscale*, 8:6369–6378, 2016.

[200] Yiru Sun, Noel C. Giebink, Hiroshi Kanno, Biwu Ma, Mark E. Thompson, and Stephen R. Forrest. Management of singlet and triplet excitons for efficient white organic light-emitting devices. *Nature*, 440:908–912, 2006.

[201] B. W. D'Andrade and S. R. Forrest. White organic light-emitting devices for solid-state lighting. *Adv. Mater.*, 16:1585–1595, 2004.

[202] Yasuhiro Shiraishi, Hiroyuki Hara, Takayuki Hirai, and Isao Komasawa. A deep desulfurization process for light oil by photosensitized oxidation using a triplet photosensitizer and hydrogen peroxide in an oil/water two-phase liquid–liquid extraction system. *Ind. Eng. Chem. Res.*, 38:1589–1595, 1999.

[203] Yifan Liu and Jianzhang Zhao. Visible light-harvesting perylenebisimide-fullerene (C_{60}) dyads with bidirectional "ping-pong" energy transfer as triplet photosensitizers for photooxidation of 1,5-dihydroxynaphthalene. *Chem. Commun.*, 48:3751–3753, 2012.

[204] Qian Liu, Baoru Yin, Tianshe Yang, Yongchao Yang, Zhen Shen, Ping Yao, and Fuyou Li. A general strategy for biocompatible, high-effective upconversion nanocapsules based on triplet-triplet annihilation. *J. Am. Chem. Soc.*, 135:5029–5037, 2013.

[205] A De Vos. Detailed balance limit of the efficiency of tandem solar cells. *J. Phys. D: Appl. Phys.*, 13:839, 1980.

[206] Zach M. Beiley and Michael D. McGehee. Modeling low cost hybrid tandem photovoltaics with the potential for efficiencies exceeding 20%. *Energy Environ. Sci.*, 5:9173–9179, 2012.

[207] Tomas Leijtens, Samuel D. Stranks, Giles E. Eperon, Rebecka Lindblad, Erik M. J. Johansson, Ian J. McPherson, Håkan Rensmo, James M. Ball, Michael M. Lee, and Henry J. Snaith. Electronic properties of meso-superstructured and planar organometal halide perovskite films: Charge trapping, photodoping, and carrier mobility. *ACS Nano*, 8:7147–7155, 2014.

[208] Lili Wang, Christopher McCleese, Anton Kovalsky, Yixin Zhao, and Clemens Burda. Femtosecond time-resolved transient absorption spectroscopy of $CH_3NH_3PbI_3$ perovskite films: Evidence for passivation effect of PbI_2. *J. Am. Chem. Soc.*, 136:12205–12208, 2014.

[209] R. D. Willett. Structures of the antiferrodistortive layer perovskites bis(phenethylammonium) tetrahalocuprate(ii), halo = Cl^-, Br^-. *Acta Cryst. C*, 46:565–568, 1990.

[210] William E. Estes, D. Bruce Losee, and William E. Hatfield. The magnetic properties of several quasi twoâĂŘdimensional heisenberg layer compounds: A new class of ferromagnetic insulators involving halocuprates. *J. Chem. Phys.*, 72:630–638, 1980.

[211] Anne H. Arkenbout, Takafumi Uemura, Jun Takeya, and Thomas T. M. Palstra. Charge-transfer induced surface conductivity for a copper based inorganic-organic hybrid. *Appl. Phys. Lett.*, 95:173104, 2009.

[212] Lior Iagher and Lioz Etgar. Effect of cs on the stability and photovoltaic performance of 2d/3d perovskite-based solar cells. *ACS Energy Lett.*, 3:366–372, 2018.

[213] T. Umebayashi, K. Asai, T. Kondo, and A. Nakao. Electronic structures of lead iodide based low-dimensional crystals. *Phys. Rev. B*, 67:155405, 2003.

[214] Bayrammurad Saparov, Feng Hong, Jon-Paul Sun, Hsin-Sheng Duan, Weiwei Meng, Samuel Cameron, Ian G. Hill, Yanfa Yan, and David B. Mitzi. Thin-film preparation and characterization of $Cs_3Sb_2I_9$: A lead-free layered perovskite semiconductor. *Chem. Mater.*, 27:5622–5632, 2015.

[215] Alberto Fraccarollo, Valentina Cantatore, Gabriele Boschetto, Leonardo Marchese, and Maurizio Cossi. Ab initio modeling of 2d layered organohalide lead perovskites. *J. Chem. Phys.*, 144:164701, 2016.

[216] H.L. Störmer, R. Dingle, A.C. Gossard, W. Wiegmann, and M.D. Sturge. Two-dimensional electron gas at a semiconductor-semiconductor interface. *Solid State Commun.*, 29:705–709, 1979.

[217] Daniele Cortecchia, Herlina Arianita Dewi, Jun Yin, Annalisa Bruno, Shi Chen, Tom Baikie, Pablo P Boix, Michael Grätzel, Subodh Mhaisalkar, Cesare Soci, and Mathews Nripan. Lead-free $MA_2CuCl_xBr_{4-X}$ hybrid perovskites. *Inorg. Chem.*, 55:1044–1052, 2016.

[218] P.M. Koenraad and Michael Flatté. Single dopants in semiconductors. *Nat. Mater.*, 10:91–100, 2011.

[219] James M. Ball and Annamaria Petrozza. Defects in perovskite-halides and their effects in solar cells. *Nature Energy*, 1:16149, 2016.

[220] Yuanyue Liu, Hai Xiao, and William A. Goddard. Two-dimensional halide perovskites: Tuning electronic activities of defects. *Nano Lett.*, 16:3335–3340, 2016.

[221] Wan-Jian Yin, Tingting Shi, and Yanfa Yan. Unique properties of halide perovskites as possible origins of the superior solar cell performance. *Adv. Mater.*, 26:4653–4658, 2014.

[222] Wan-Jian Yin, Tingting Shi, and Yanfa Yan. Unusual defect physics in ch3nh3pbi3 perovskite solar cell absorber. *Appl. Phys. Lett.*, 104:063903, 2014.

[223] Li Na Quan, Mingjian Yuan, Riccardo Comin, Oleksandr Voznyy, Eric M. Beauregard, Sjoerd Hoogland, Andrei Buin, Ahmad R. Kirmani, Kui Zhao, Aram Amassian, Dong Ha Kim, and Edward H. Sargent. Ligand-stabilized reduced-dimensionality perovskites. *J. Am. Chem. Soc.*, 138:2649–2655, 2016.

[224] Hui-Seon Kim, Chang-Ryul Lee, Jeong-Hyeok Im, Ki-Beom Lee, Thomas Moehl, Arianna Marchioro, Soo-Jin Moon, Robin Humphry-Baker, Jun-Ho Yum, Jacques E. Moser, Michael Grätzel, and Nam-Gyu Park. Lead iodide perovskite sensitized all-solid-state submicron thin film mesoscopic solar cell with efficiency exceeding 9%. *Sci. Rep.*, 2:591, 2012.

[225] Michael M. Lee, Joël Teuscher, Tsutomu Miyasaka, Takurou N. Murakami, and Henry J. Snaith. Efficient hybrid solar cells based on meso-superstructured organometal halide perovskites. *Science*, 338:643–647, 2012.

[226] Mulmudi Hemant Kumar, Natalia Yantara, Sabba Dharani, Michael Graetzel, Subodh Mhaisalkar, Pablo P. Boix, and Nripan Mathews. Flexible, low-temperature, solution processed zno-based perovskite solid state solar cells. *Chem. Commun.*, 49:11089–11091, 2013.

[227] Pablo Docampo, James M. Ball, Mariam Darwich, Giles E. Eperon, and Henry J. Snaith. Efficient organometal trihalide perovskite planar-heterojunction solar cells on flexible polymer substrates. *Nat. Commun.*, 4:276, 2013.

[228] Jingbi You, Ziruo Hong, Yang Michael Yang, Qi Chen, Min Cai, Tze-Bin Song, Chun-Chao Chen, Shirong Lu, Yongsheng Liu, Huanping Zhou, and Yang Yang. Low-temperature solution-processed perovskite solar cells with high efficiency and flexibility. *ACS Nano*, 8:1674–1680, 2014.

[229] Yuming Wang, Sai Bai, Lu Cheng, Nana Wang, Jianpu Wang, Feng Gao, and Wei Huang. High-efficiency flexible solar cells based on organometal halide perovskites. *Adv. Mater.*, 28:4532–4540, 2016.

[230] Anastasia Vassilakopoulou, Dionysios Papadatos, and Ioannis Koutselas. Flexible, cathodo-luminescent and free standing mesoporous silica films with entrapped quasi-2d perovskites. *Appl. Sur. Sci.*, 400:434–439, 2017.

[231] Jacky Even, Laurent Pedesseau, M A. Dupertuis, J Jancu, and Claudine Katan. Electronic model for self-assembled hybrid organic/perovskite semiconductors: Reverse band edge electronic states ordering and spin-orbit coupling. *Phys. Rev. B*, 86:205301, 2012.

[232] Jacky Even, Laurent Pedesseau, Claudine Katan, Mikaël Kepenekian, Jean-Sébastien Lauret, Daniel Sapori, and Emmanuelle Deleporte. Solid-state physics perspective on hybrid perovskite semiconductors. *J. Phys. Chem. C*, 119:10161–10177, 2015.

[233] Laurent Pedesseau, Daniel Sapori, Boubacar Traore, Roberto Robles, Hong-Hua Fang, Maria Antonietta Loi, Hsinhan Tsai, Wanyi Nie, Jean-Christophe Blancon, Amanda Neukirch, Sergei Tretiak, Aditya D. Mohite, Claudine Katan, Jacky Even, and Mikaël Kepenekian.

Advances and promises of layered halide hybrid perovskite semiconductors. *ACS Nano*, 10:9776–9786, 2016.

[234] Boubacar Traore, Laurent Pedesseau, Linda Assam, Xiaoyang Che, Jean-Christophe Blancon, Hsinhan Tsai, Wanyi Nie, Constantinos C. Stoumpos, Mercouri G. Kanatzidis, Sergei Tretiak, Aditya D. Mohite, Jacky Even, MikaÃńl Kepenekian, and Claudine Katan. Composite nature of layered hybrid perovskites: Assessment on quantum and dielectric confinements and band alignment. *ACS Nano*, 12:3321–3332, 2018.

[235] K. W. Schlichting, N. P. Padture, and P. G. Klemens. Thermal conductivity of dense and porous yttria-stabilized zirconia. *J. Mater. Sci.*, 36:3003–3010, 2001.

[236] Alexandra Navrotsky. Thermochemical insights into refractory ceramic materials based on oxides with large tetravalent cations. *J. Mater. Chem.*, 15:1883–1890, 2005.

[237] X.Q. Cao, R. Vassen, and D. Stoever. Ceramic materials for thermal barrier coatings. *J. Am. Ceram. Soc.*, 24:1–10, 2004.

[238] Robert L. Jones and Derek Mess. Improved tetragonal phase stability at 1400°C with scandia, yttria-stabilized zirconia. *Surf. Coat. Technol.*, 86-87:94–101, 1996.

[239] R. W. Trice, Y. Jennifer Su, J. R. Mawdsley, K. T. Faber, A. R. De Arellano-López, Hsin Wang, and W. D. Porter. Effect of heat treatment on phase stability, microstructure, and thermal conductivity of plasma-sprayed ysz. *J. Mater. Sci.*, 37:2359–2365, 2002.

[240] M. J. Stiger, N. M. Yanar, F. S. Pettit, and G. H. Meier. Thermal barrier coatings for the 21st century. *Z. Metall*, 90:1069–1078, 1999.

[241] Smialek J. I. The chemistry of saudi arabian sand: A deposition problem on helicopter turbine airfoils. Number 105234. NASA Technical Memorandum, 1991.

[242] Jong-Heun Lee, Toshiyuki Mori, Ji-Guang Li, Takayasu Ikegami, John Drennan, and Doh-Yeon Kim. Scavenging of siliceous grain-boundary phase of 8-mol%-ytterbia-stabilized zirconia without additive. *J. Am. Ceram. Soc.*, 84:2734–2736, 2001.

[243] Giacomo Giorgi, Anatoli Korkin, and Koichi Yamashita. Zirconium and hafnium oxide interface with silicon: Computational study of stress and strain effects. *Comput. Mater. Sci.*, 43:930–937, 2008.

[244] R. L. Jones. Some aspects of the hot corrosion of thermal barrier coatings. *J. Therm. Spray Technology*, 6:77–84, 1997.

[245] F.H. Stott, D.J. de Wet, and R. Taylor. Degradation of thermal-barrier coatings at very high temperatures. *MRS Bulletin*, 19:46–49, 1994.

[246] Stephan Krämer, James Yang, Carlos G. Levi, and Curtis A. Johnson. Thermochemical interaction of thermal barrier coatings with molten cao–mgo–Al_2O_3–SiO_2 (cmas) deposits. *J. Am. Ceram. Soc.*, 89:3167–3175, 2006.

[247] Jing Wu, Hong bo Guo, Yu zhi Gao, and Sheng kai Gong. Microstructure and thermo-physical properties of yttria stabilized zirconia coatings with cmas deposits. *J. Eur. Ceram. Soc.*, 31:1881–1888, 2011.

[248] C. Mercer, S. Faulhaber, A.G. Evans, and R. Darolia. A delamination mechanism for thermal barrier coatings subject to calcium–magnesium–alumino–silicate (cmas) infiltration. *Acta Mater.*, 53:1029–1039, 2005.

[249] Xi Chen. Calcium–magnesium–alumina–silicate (cmas) delamination mechanisms in eb-pvd thermal barrier coatings. *Surf. Coat. Technol.*, 200:3418–3427, 2006.

[250] R. Wellman, G. Whitman, and J.R. Nicholls. Cmas corrosion of eb pvd tbcs: Identifying the minimum level to initiate damage. *Int. J. of Refract. Met. Hard Mater.*, 28:124–132, 2010.

[251] R. M. Latanision and H. Opperhauser. The intergranular embrittlement of nickel by hydrogen: The effect of grain boundary segregation. *Metall. Trans.*, 5:483–492, 1974.

[252] H. Erhart and H. J. Grabke. Equilibrium segregation of phosphorus at grain boundaries of fe–p, fe–c–p, fe–cr–p, and fe–cr–c–p alloys. *Met. Sci.*, 15:401–408, 1981.

[253] Masatake Yamaguchi, Motoyuki Shiga, and Hideo Kaburaki. Grain boundary decohesion by impurity segregation in a nickel-sulfur system. *Science*, 307:393–397, 2005.

[254] M Matsuda, J Nowotny, Z Zhang, and C.C Sorrell. Lattice and grain boundary diffusion of ca in polycrystalline yttria-stabilized ZrO_2 determined by employing sims technique. *Solid State Ion.*, 111:301–306, 1998.

[255] K. Kowalski, A. Bernasik, and A. Sadowski. Diffusion of calcium in yttria stabilized zirconia ceramics. *J. Eur. Ceram. Soc.*, 20:2095–2100, 2000.

[256] Xin Guo, Chao-Qun Tang, and Run-Zhang Yuan. Grain boundary ionic conduction in zirconia-based solid electrolyte with alumina addition. *J. Eur. Ceram. Soc.*, 15:25–32, 1995.

[257] Makoto Aoki, Yet-Ming Chiang, Igor Kosacki, L. Jong-Ren Lee, Harry Tuller, and Yaping Liu. Solute segregation and grain-boundary impedance in high-purity stabilized zirconia. *J. Eur. Ceram. Soc.*, 79:1169–1180, 1996.

[258] Y. Oishi and H. Ichimura. Grain–boundary enhanced interdiffusion in polycrystalline cao–stabilized zirconia system. *J. Chem. Phys.*, 71:5134–5139, 1979.

[259] E.D. Hondros and M.P. Seah. Grain boundary activity measurements by auger electron spectroscopy. *Scr. Metall. Mater.*, 6:1007–1012, 1972.

[260] M. P. Seah, E. D. Hondros, and Anthony Kelly. Grain boundary segregation. *Proc. R. Soc. Lond. A Mater.*, 335:191–212, 1973.

[261] C. L. Briant. On the chemistry of grain boundary segregation and grain boundary fracture. *Metall. Trans. A*, 21:2339–2354, 1990.

[262] Hark B. Lee, Friedrich B. Prinz, and Wei Cai. Atomistic simulations of grain boundary segregation in nanocrystalline yttria-stabilized zirconia and gadolinia-doped ceria solid oxide electrolytes. *Acta Mater.*, 61:3872–3887, 2013.

[263] Jihwan An, Joong Sun Park, Ai Leen Koh, Hark B. Lee, Hee Joon Jung, Joop Schoonman, Robert Sinclair, Turgut M. Gür, and Fritz B. Prinz. Atomic scale verification of oxide-ion vacancy distribution near a single grain boundary in ysz. *Sci. Rep.*, 3:2680EP–, 2013.

[264] David R. Clarke and Simon R. Phillpot. Thermal barrier coating materials. *Mater. Today*, 8:22–29, 2005.

[265] A. Predith, G. Ceder, C. Wolverton, K. Persson, and T. Mueller. Ab initio prediction of ordered ground-state structures in ZrO_2-Y_2O_3. *Phys. Rev. B*, 77:144104, 2008.

[266] G. Kresse and J. Furthmüller. Efficiency of *ab-initio* total energy calculations for metals and semiconductors using a plane-wave basis set. *Comput. Mater. Sci.*, 6:15–50, 1996.

[267] Craig A.J Fisher and Hideaki Matsubara. Molecular dynamics investigations of grain boundary phenomena in cubic zirconia. *Comput. Mater. Sci.*, 14:177–184, 1999.

[268] I. A. El-Shanshoury, V. A. Rudenko, and I. A. Ibrahim. Polymorphic behavior of thin evaporated films of zirconium and hafnium oxides. *J. Am. Ceram. Soc.*, 53:264–268, 1970.

[269] Julian D. Gale and Andrew L. Rohl. The general utility lattice program (gulp). *Mol. Simul.*, 29:291–341, 2003.

[270] Matthew O. Zacate, Licia Minervini, Daniel J. Bradfield, Robin W. Grimes, and Kurt E. Sickafus. Defect cluster formation in M_2O_3-doped cubic ZrO_2. *Solid State Ion.*, 128:243–254, 2000.

[271] Yanhao Dong, Liang Qi, Ju Li, and I-Wei Chen. A computational study of yttria-stabilized zirconia: I. using crystal chemistry to search for the ground state on a glassy energy landscape. *Acta Mater.*, 127:73–84, 2017.

[272] Kesong Yang, Corey Oses, and Stefano Curtarolo. Modeling off-stoichiometry materials with a high-throughput ab-initio approach. *Chem. Mater.*, 28:6484–6492, 2016.

[273] Jianli Cheng, Jian Luo, and Kesong Yang. Aimsgb: An algorithm and open-source python library to generate periodic grain boundary structures. *Comput. Mater. Sci.*, 155:92–103, 2018.